Heinz Maier-Leibnitz Zentrum
und Physik - Department

Surface segregation studied by time-resolved positron annihilation induced Auger electron spectroscopy

Dissertation
von

Samantha Maria Zimnik

Technische Universität München

Technische Universität München

Heinz Maier-Leibnitz Zentrum und

Physik-Department - Lehrstuhl E21 für Neutronenstreuung

Surface segregation studied by time-resolved positron annihilation induced Auger electron spectroscopy

Samantha Maria Zimnik

Vollständiger Abdruck der von der Fakultät für Physik der Technischen Universität München zur Erlangung des akademischen Grades eines

Doktors der Naturwissenschaften (Dr. rer. nat.)

genehmigten Dissertation.

Vorsitzender: apl. Prof. Dr. Norbert Kaiser

Prüfer der Dissertation:

1. Priv.-Doz. Dr. Christoph P. Hugenschmidt
2. Univ.-Prof. Dr. Johannes Barth

Die Dissertation wurde am 12.04.2017 bei der Technischen Universität München eingereicht und durch die Fakultät für Physik am 22.05.2017 angenommen.

Abstract

It is a common observation that certain elements in a solid solution tend to accumulate at surfaces. For the investigation and development of this surface segregation process with regard to catalytic applications, analysis techniques with highest surface sensitivity are required.

Within this thesis, surface segregation of Fe/Pt, Ni/Pt and Ni/Pd was investigated using Positron annihilation induced Auger Electron Spectroscopy (PAES). The upgraded surface spectrometer at NEPOMUC (NEutron induced POsitron source MUniCh) enables a comprehensive characterization of the surface topography and the elemental composition with complementary techniques in a temperature range between 95 K and 1500 K. A new approach for the evaluation of PAES spectra of compounds was developed, using the spectra obtained for the pure elements as reference.

Comparative studies on sub-monolayer coverage of Ni on Pd using conventional AES induced by X-rays or electrons and X-ray induced Photoelectron Spectroscopy (XPS) demonstrated the exceptional surface sensitivity of PAES. In particular, a clear and element specific effect to the PAES signal was observed as a consequence of H exposure of a Ni/Pd surface, which was not detectable with XPS. Additionally, an unprecedented measurement time for PAES of only 230 s was achieved. Time-dependent PAES was performed on a Ni cover layer on Pd. The PAES results show a migration of Ni atoms into the Pd substrate according to the decreasing of the Ni signal by 12 % within 13 hours at room temperature. The chemical specificity of XPS was applied to rule out varying influence on the elements from surface contamination due to the residual gas.

Temperature-dependent PAES enabled the in situ observation of the surface segregation of Ni adatoms on single crystalline Pd surfaces. The activation energy for surface segregation was found to depend strongly on the surface orientation and was determined to 38.4(3) meV for Pd(111), 46.0(10) meV for Pd(100), and 51.6(9) meV for Pd(110). Moreover, surface segregation of thin layers of Ni and Pd was studied on a MgO(001) substrate. A clear tendency for surface segregation was observed and even after subsequent heating, the topmost Pd layer was shown to be stable. Evidence for surface segregation already during growth was found for an alloy of Ni and Pd on MgO. In contrast to Ni/Pd, the system Ni/Pt was determined to show no surface segregation.

PAES was successfully applied to observe surface segregation in situ and determine the activation energy. The exceptional surface sensitivity and the element specific sensitivity to H adsorbtion provide unique information for the investigation of catalysts.

Zusammenfassung

Häufig wird die Anlagerung bestimmter Elemente an der Oberfläche beobachtet, die zunächst in einem Mischkristall homogen verteilt waren. Um diesen Oberflächensegregationsprozess zu untersuchen und für katalytische Anwendungen nutzbar zu machen, sind Analysetechniken mit höchstmöglicher Oberflächensensitivität nötig.

Der Oberflächensegregationsprozess in Fe/Pt, Ni/Pt und Ni/Pd wurde mit durch Positronenannihilation induzierter Augerelektronenspektroskopie (PAES) untersucht. Das erweiterte Oberflächenspektrometer an NEPOMUC (NEutron induced POsitron source MUniCh) ermöglicht eine umfassende Charakterisierung der Oberflächentopologie und Elementzusammensetzung mit komplementären Messmethoden in einem Temperaturbereich zwischen 95 K und 1500 K. Ein neuartiger Ansatz für die Auswertung von PAES Spektren von Elementkombinationen wurde entwickelt. Dabei werden die Spektren von Reinmaterialien als Referenzen nutzt.

Durch Gegenüberstellung der Ergebnisse von konventioneller AES, induziert durch Röntgenstrahlung oder Elektronen und Röntgenphotoelektronenspektroskopie (XPS) von Submonolayerbedeckungen von Ni auf Pd konnte die außergewöhnliche Oberflächensensitivität von PAES nachgewiesen werden. Deutliche elementspezifische Auswirkungen auf das PAES Signal wurden nach der Wasserstoffexposition einer Ni/Pd Oberfläche detektiert, die XPS verborgen bleiben. Eine bislang unerreichte Messzeit von nur 230 s für ein PAES Spektrum wurde realisiert. Zeitabhängige PAES wurde an Ni Deckschichten auf Pd durchgeführt. Die Abnahme des Ni Signals um 12 % innerhalb von 13 h zeigt die Verlagerung der Ni Atome in das Pd Substrat bei Raumtemperatur. Die chemische Spezifizität von XPS wurde dabei genutzt, um unterschiedliche Einflüsse des Restgases auf die Elemente auszuschließen.

Der Oberflächensegregationsprozess von Ni Adatomen auf einkristallinen Pd Substraten konnte mit temperaturabhängiger PAES in situ beobachtet werden. Es wurde gezeigt, dass die Aktivierungsenergie für den Segregationsprozess stark von der Oberflächenorientierung abhängt. Eine Aktivierungsenergie von 38.4(3) meV wurde für Pd(111) ermittelt, 46.0(10) meV für Pd(100) und 51.6(9) meV für Pd(110). Die Oberflächensegregation in dünnen Schichten aus Ni und Pd auf MgO(001) wurde ebenfalls untersucht. Auch hier wurde eine klare Tendenz für die Oberflächensegregation und die Stabilität der Pd Deckschicht auch nach dem Aufheizen der Probe beobachtet. Beim Aufwachsen einer NiPd Legierung auf MgO zeigt sich bereits während der Herstellung eine Tendenz zur Oberflächensegregation. Für das System Ni/Pt konnte nachgewiesen werden, dass im Gegensatz zu Ni/Pd darin kein Oberflächensegregationsprozess auftritt.

Mittels PAES konnten Oberflächensegregationsprozesse in situ nachgewiesen und erfolgreich die Aktivierungsenergien ermittelt werden. Die herausragende Oberflächensensitivität sowie die elementspezifische Sensitivität für Wasserstoffanlagerung liefern einzigartige Informationen bei der Erforschung von Katalysatoren.

Contents

Chapter 1

Introduction

Surface phenomena have fascinated people for centuries. The Lotus flower even found its way into mythology and culture as a symbol of purity, long before the investigation of the physical reasons of its water repellent leafs could begin. The hydrophobic mechanism was explained in the early 1970s after the introduction of the scanning electron microscope. The evolution of ultra high vacuum technology in the 1960s allowed the stabilization of surfaces for several hours and thereby their analysis with electron spectroscopy techniques for the first time. The development of scanning probe microscopes with a resolution down to the atomic scale in the 1980s as well as the huge increase in computational power enabled highly complex surface experiments. Surface physics and surface chemistry emerged as new fields of research. Nowadays the applications of surface science technology such as heterogeneous catalysis, semiconductor device fabrication and fuel cells form the basis for a large number of modern daily-life products.

The surface of a solid is involved in many processes of particular interest such as oxidation, surface segregation, or catalysis. Since these processes significantly affect several macroscopic properties of thin films or nanoparticles, detailed knowledge of the surface structure and elemental composition is of great importance. For example, functional materials and surfaces based on Pd are applied for heterogeneous catalysis and for hydrogen purification. For industrial applications, several aspects play an important role such as the chemical composition of the Pd surface, which influences the catalytic properties substantially, and the mechanical stability e.g. of thin membranes, which is affected by foreign atoms or segregation processes.

Catalysts consisting of a combination of catalytically active elements are developed in order to increase the efficiency and reduce the costs. Another approach to bring further improvements in this respect is the fabrication of core-shell catalyst structures containing an inexpensive, non-noble core surrounded by a noble-metal shell. The effect of surface segregation can be applied for the development of core-shell nanocatalysts. However, the complex interplay of the elements at the surface, which is also influenced by the fabrication process, needs to be understood to achieve a long term stability.

The progress in data storage techniques are closely related to advances in surface physics. The monolithic manufacturing of integrated circuits with structural sizes in the nanometer scale is only possible due to the understanding of material properties and manufacturing processes, such as thin film technology. For data storage, heat assisted magnetic recording is developed to enhance the capacity from nowadays $1\,\mathrm{Tb/inch^2}$ leading to a length scale of 25 nm per bit even further. This is strongly related with research on materials with a high magneto-crystalline anisotropy, as for example found for FePt and the size-dependent stability of such nanoclusters against oxidation and surface segregation.

For the comprehension of complex surface phenomena such as surface segregation, an analysis technique with highest surface sensitivity is necessary. Positron annihilation induced Auger electron spectroscopy (PAES) is known for its excellent top layer sensitivity and was applied in this work to study surface segregation processes systematically on Fe/Pt, Ni/Pt and Ni/Pd. The measurements were carried out time- and temperature-dependent, making the migration of adatoms observable for the first time. The PAES studies were accompanied by X-ray photoelectron spectroscopy, which allowed indispensable information due to its chemical specificity. The combination of these highly specialized techniques gave new insights to surface segregation processes presented in this work.

Chapter 2

Positrons for surface analysis

2.1 The positron as probing particle

The positron is the antiparticle of the electron. It was postulated by Paul A. M. Dirac in 1928 as a solution of the Dirac equation allowing a positive charge for electrons [1]. Four years later, Carl David Anderson detected a previously unknown particle in cloud chamber experiments on cosmic rays. From the magnetic deflection, direction and the length of the particle's ion trace he was able to prove that it was the positron [2]. The physical properties of the positron are summarized in Table 2.1.

Nowadays positrons are used in various methods in order to investigate solids in a non-destructive way and to determine the mechanical, optical and electronic properties. Positrons as nano-probes are particularly sensitive to lattice defects in a bulk material such as vacancies or dislocations. The open volume defects represent an attractive potential for positrons, due to the missing positive charge of the nucleus. A thermalized positron, which has lost all its energy due to scattering processes with electrons and phonons, can be trapped in such a defect when diffusing over hundreds of lattice constants through the solid.

A number of measurement techniques have been established in order to perform spectroscopy on defects and measurements on the electron momentum distribution using positrons. The annihilation radiation, which is emitted as a result of the annihilation of an electron with a positron, is detected and analyzed with regard to the energy distribution and angular correlation of

the γ-quanta. The Doppler broadening spectroscopy provides a quantitative analysis of defects [5]. The detection of the γ-quanta in coincidence, as it is the case for coincident Doppler broadening spectroscopy, allows conclusions about the chemical composition of the surrounding atoms of the vacancies [6]. For the characterization of defect types, such as atomic vacancies or dislocations in the crystal lattice, the positron lifetime spectroscopy is applied [7]. In defect-free single crystals, positrons are able to provide information on the electron momentum distribution, which is used in measurements of the angular correlation of annihilation radiation [8].

Positrons, however, gain insight into the bulk structure of a material, but also allow the investigation of their surface with highest sensitivity. Total reflection high energy positron diffraction allows the investigation of atom positions in the topmost surface layer [9, 10]. Their exact position determine the electronic structure and magnetic properties of the crystal surface.

Low energy positrons have been applied to study adsorbates, cover layers with nominal thicknesses in the (sub-)monolayer range, as well as surface segregation processes. Positron annihilation induced Auger electron spectroscopy is an element selective and highly sensitive analysis technique to study the topmost atomic layer of a solid [11]. A detailed description of this method of analysis can be found in Section 3.1.3.

2.2 Positron trapping in surface states

Many channels are open to positrons when they encounter matter, which are summarized in Figure 2.1. Positrons, which are not reflected at the surface loose their energy inside the solid within picoseconds in a so-called thermalization process. Depending on the energy of the positrons, different interactions occur: positrons with an energy of a few keV, loose their energy by ionization of core and valence electrons. In an energy range below 100 eV, the excitation of electron-hole pairs is the dominant loss mechanism. At low energies below 5 eV down to thermal energy, phonon scattering is the main energy loss process [12]. The positron lifetime in the solid is in the range of several hundred picoseconds up to nanoseconds [7]. After the thermalization, the positron diffuses through the solid. The diffusion length is typically in the order of 100 nm.

The material dependent penetration depth of positrons is described by the Makhovian implantation profile and results in a mean implantation depth of approximately 100 nm for a 3 keV positron beam in Al [13]. When implanted into the bulk of the solid, annihilation can occur either in the crystal lattice or when the positron is trapped in a vacancy. When implanted with low energies of some eV surface interactions are dominant. The electron density extends beyond the surface towards the vacuum and leads to the creation of a surface dipole, known as dipol barrier for electrons. Detailed surface calculation found an image potential induced positron surface state wavefunction by numerical solution of a single particle Schrödinger equation. The potential was calculated using the corugated mirrir model [14, 15]. Hence, the surface is an attractive site for positrons [4]. The surface potential is the fundamental prerequisite for the surface sensitivity of positron studies. For illustration, a scheme of the surface potential is shown in Figure 2.2.

For electrons, the chemical potential in the bulk corresponds to the Fermi energy. In case of positrons, usually only one positron is present in the solid within its lifetime. Therefore, the positron ground state can be described as a delocalized Bloch wave in the periodic lattice potential. The image potential of the positron forms the surface potential well resulting in positron surface states. In contrast to electrons, the dipol barrier Δ is negative for positrons, that enables negative and positive values of the positron work function Φ_+, depending on the chemical potential for positrons μ_+ of the solid:

$$\Phi_+ = -\Delta - \mu_+ \tag{2.1}$$

Metals with a negative work function are e.g. W, Pt or Ni, show to spontaneous emission of positrons to the vacuum with a discrete energy. This process, including the previous thermalization is called positron moderation.

Apart from positron moderation two other processes of positrons in the surface state are distinguished: Positronium (Ps) formation and the emission of Auger electrons. Ps, a bound state of an electron and a positron, can be formed, when a positron arriving at the surface picks up an electron. The binding energy of Ps is 6.8 eV. Ps is initially bound to the surface and can be emitted by thermal activation. The formation of Ps can be studied when recording energy spectra of the positron annihilation radiation with a high purity Ge detector.

Ps can be formed in two states, depending on the orientation of the spins of positron and electron. Para-Ps, the singlet state has a total spin S=0 and ortho-PS, the triplet state with a total spin of S=1. From the respective spin multiplicities follows a formation probability of 3:1 in favor of the triplet state. Due to the conservation of angular momentum, ortho-Ps annihilates in three γ-quanta, which have a continuous energy distribution up to 511 keV. When comparing the count ratio in the valley between the Compton edge and the onset of the photopeak with the intensity of the photopeak, the Ps formation can be studied.

When the positron is trapped in the surface state, annihilation with an electron from a surface atom occurs. The relaxation of the ionized atom can lead to characteristic X-ray emission or an Auger process can be induced. The latter allows the study of the elemental composition of the surface atoms with exceptional surface sensitivity and will be discussed in more detail in Chapter 3. The trapping of positrons in the surface state is illustrated in Figure 2.3 at the example of Cu(100) showing the localization of the positron wave function at the crystal surface. This feature of positron interaction with the sample surface is fundamental for the outstanding sensitivity of surface analysis using positrons.

rest mass	$m_0 = 9.10938215(45) \cdot 10^{-31}\,\mathrm{kg}$
rest energy	$E_0 = 510.998910(13)$ keV
charge	$q = +1.6021917(70) \cdot 10^{-19}\,\mathrm{C}$
spin	$\frac{1}{2}$
magnetic moment	$\mu = 1.001159658(4) \cdot \mu_B$
vacuum lifetime	$\tau > 2 \cdot 10^{21}\,\mathrm{a}$

Table 2.1: Physical properties of the positron. [3, 4]

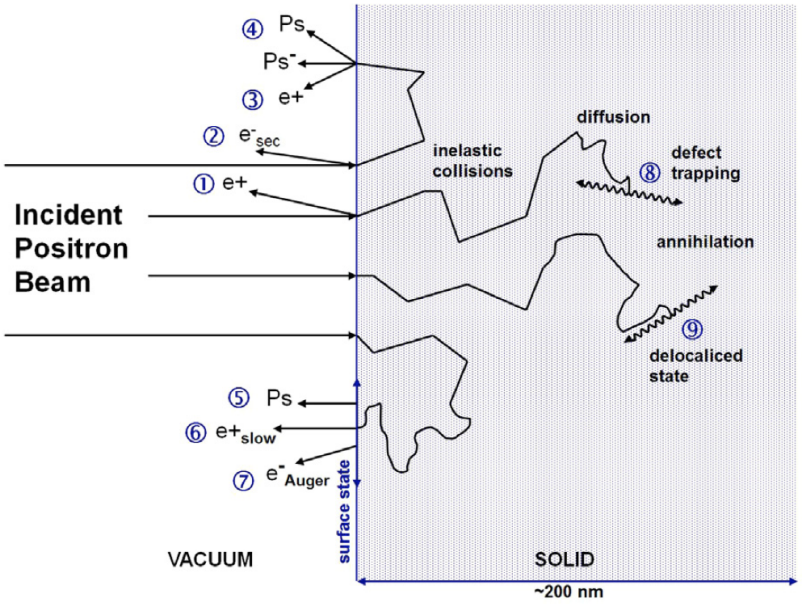

Figure 2.1: Interaction of positrons with matter: When a positron impinges the surface, reflection and deflection can occur (1) and secondary electrons are emitted (2). Non-thermalized positrons can leave the surface as fast positrons (3) or as a bound state with one (Ps) or two electrons (Ps^-) (4). When a thermalized positron diffuses back to the surface, the desorption of Ps (5) is possible and, depending on the work function of the solid, the emission of moderated positrons (6). For the present work, the annihilation in a surface state leading to the emission of Auger electrons (7) is most important. When positrons are implanted into the bulk, annihilation in a defect (8) or from a delocalized state in the crystal lattice are possible. Taken from [16].

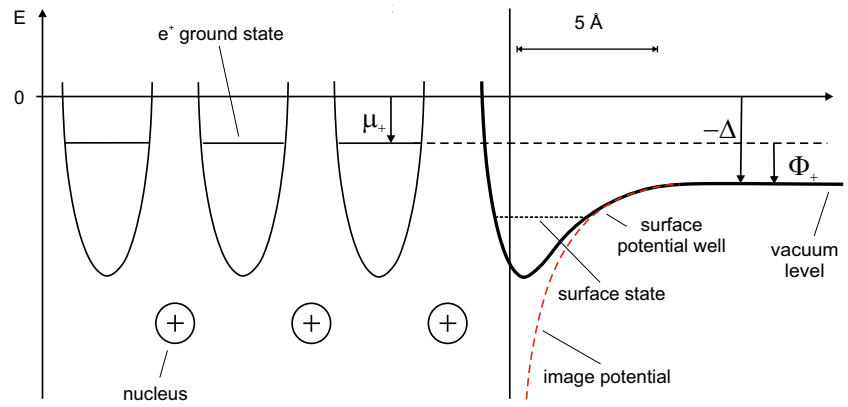

Figure 2.2: Scheme of the bulk and surface potential for positrons. In contrast to electrons, the dipol barrier Δ is negative for positrons which can lead to negative and positive values for the positron work function Φ_+, depending on the chemical potential for positrons μ_+ in the solid. The surface state results from the image potential of the positron. The potential is shown with respect to the 'crystal zero'.

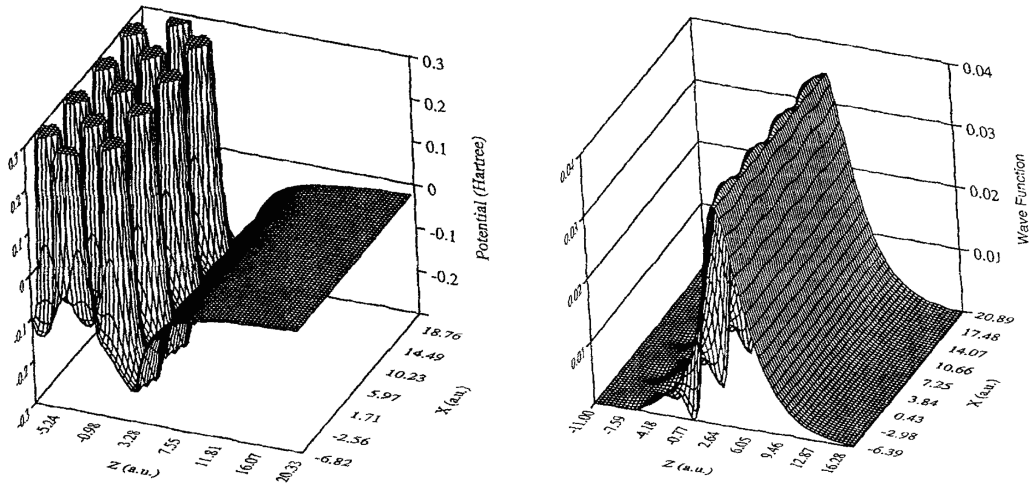

(a) (b)

Figure 2.3: a) Calculated potential and (b) probability density for positrons at the surface of Cu(100), showing the localization of the positrons at the outermost atomic layer [17]. The trapping in this surface state is the basis for the exceptional surface sensitivity of positrons in surface analysis.

Chapter 3

Surface analysis techniques

3.1 Auger electron spectroscopy

Auger electron spectroscopy is a measurement technique to analyze the elemental composition of the surface. By using positron annihilation from a surface state an exceptional selectivity for analyzing the outermost atoms is achieved. Thus, this technique can contribute to the study of catalytic materials or the analysis of surface segregation processes. Surface segregation is an atomic rearrangement of different elements on the surface of a solid as a consequence of the minimization of the Gibbs free energy. For example, Cu atoms deposited on a Pd substrate migrate even at room temperature from the surface below the first atomic layer of Pd atoms. The experimental proof of this process, which was predicted in theoretical calculations [18], was achieved for the first time with the time-dependent Auger electron spectroscopy induced by positron annihilation [19].

3.1.1 Principle of the Auger effect

The emission of electrons with discrete energy was discovered independently by Lise Meitner and Pierre Auger in the 1920s [20, 21]. The underlying Auger effect is a radiation-free transition of an ionized atom. Initially, a hole is created in an inner electron shell of the atom. Then an electron from a higher energy level fills this hole and the energy of this transition is transfered to a third electron, which leaves the atom with a discrete energy. Due to its characteristic

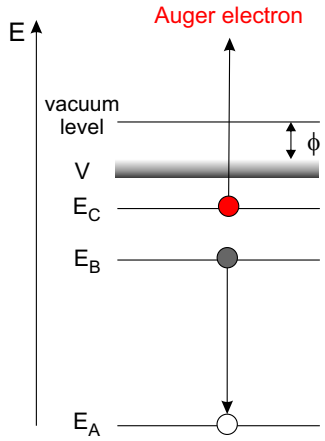

Figure 3.1: Scheme of the Auger process. A hole is created in the electron shell at the energy level E_A, which is filled with an electron from a higher level E_B. The energy released in this transition is transfered to a third electron from level E_C, the Auger electron which can leave the atom. The energy of the Auger electron characterizes the element and the involved electron states.

energy, this so-called Auger electron carries an element specific information. A scheme of this process is shown in Figure 3.1.

The nomenclature of Auger transitions describes the involved electron states in the same way as it is used for X-ray spectroscopy, e.g. $LM_{2,3}V$. The first letter names the level, in which the primary hole is formed, the second stands for the state from which the electron fills the hole. The last letter identifies the shell from which the Auger electron is emitted. Capital letters denote the main quantum number of the electron (K, L, M correspond to n = 1, 2, 3 etc.). V stands for the valence band. The subscript digits denote the total angular momentum of the orbits consisting of the angular momentum and the electron spin. Table 3.1 summarizes the terminology and the spectroscopic notation. If the energy gap of adjacent shell is small, the Auger transition may not be clearly defined and the indices of both possible electron states are indicated. If the first two shells involved have the same main quantum number the transition is called a Coster-Kronig transition. In the special case that all three electrons have the same main quantum number one denotes it as a super-Coster-Kronig transition [22].

The energy of an Auger electron from the transition ABC can be estimated using Equation 3.1 [23]. In this simplified model, influences due to the corre-

Quantum numbers				
n	l	j	Auger or X-ray name	spectroscopic level
1	0	1/2	K	$1s_{1/2}$
2	0	1/2	L_1	$2s_{1/2}$
2	1	1/2	L_2	$2p_{1/2}$
2	1	3/2	L_3	$2p_{3/2}$
3	0	1/2	M_1	$3s_{1/2}$
3	1	1/2	M_2	$3p_{1/2}$
3	1	3/2	M_3	$3p_{3/2}$
3	2	3/2	M_4	$3d_{3/2}$
3	2	5/2	M_5	$3d_{5/2}$
			...	

Table 3.1: Nomenclature of Auger and photo electron spectroscopy.

lation between the holes formed in the shells B and C, as well as relaxation energies are neglected.

$$E_{ABC} \approx E_A(Z) - \frac{1}{2}\left[E_B(Z) + E_B(Z+1)\right] - \frac{1}{2}\left[E_C(Z) + E_C(Z+1)\right] - \Phi^- \quad (3.1)$$

In Equation 3.1, E_i denotes the electron binding energy of the corresponding electron shell i=A, B, C of the atom with the nuclear charge number Z and $Z+1$, respectively. The binding energy has to be corrected accordingly because of the ionization of the atom through the initially arising hole in the level A. Φ^- denotes the electron work function, the energy of the Auger electron is reduced by this value when leaving the sample.

The probability of an Auger transition is determined by the probability of the ionization of the core level A and its de-excitation process. The competing processes are the emission of Auger electrons or photons. Characteristic X-rays can be emitted instead of Auger electrons, when an electron from an outer shell fills the vacancy in the core level. This process is called fluorescence. The quantum mechanical selection rules only allow this transition, it the difference angular quantum number $\Delta l \neq 0$. Therefore, the emission probability varies with the atomic number Z and the type of atomic level involved (K, L, M, etc.). Especially for light elements, the probability for the emission of Auger electrons is much higher than the fluorescence yield. The Auger yield and and

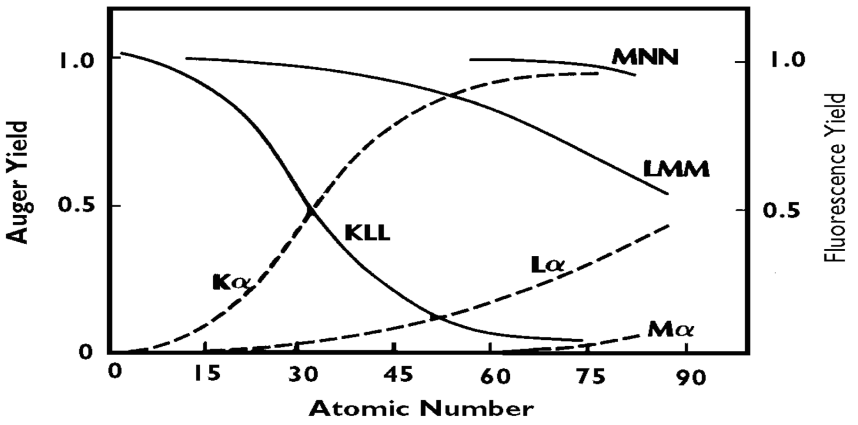

Figure 3.2: Probability for Auger electron (solid line) and X-ray emission (dashed line) as a function of the atomic number for K, L and M shell. [24, 25]

the energy of the Auger electron as a function of the atomic number are shown in Figure 3.2 and Figure 3.3, respectively.

The initial ionization of the atom can be achieved in various ways. Conventionally, electrons or X-rays are used, but also positron annihilating with a core electron can induce the Auger process. Accordingly, an additional letter (X, E, P) is added to the abbreviation AES, to distinguish between the different techniques, which are discussed in the following section.

3.1.2 Conventional AES

Auger Electron Spectroscopy (AES) is a widely used surface analysis technique for the investigation of the elemental composition of the surface-near layers. The Auger process is usually induced by ionization of the sample atoms with electrons or X-rays (EAES or XAES). For EAES the ionization cross section is correlated with the kinetic energy of the primary electron and the binding energy of the shell, which should be ionized. The relationship is shown in Figure 3.4a. A maximum of the ionization cross section is observed when the energy of the primary electrons is about three times the binding energy. Therefore, usually electron energies in the keV range are necessary. The absolute value for the cross section is typically in the range of 10^{-3} to 10^{-4}, i.e. the probability of an ionization followed by an Auger de-excitation is 1 in 10^4. For XAES, the ionization cross sections are determined by the X-ray photoionization cross sections, which are listed in e.g. [27]. Usually, the K_α lines of Al or Mg are

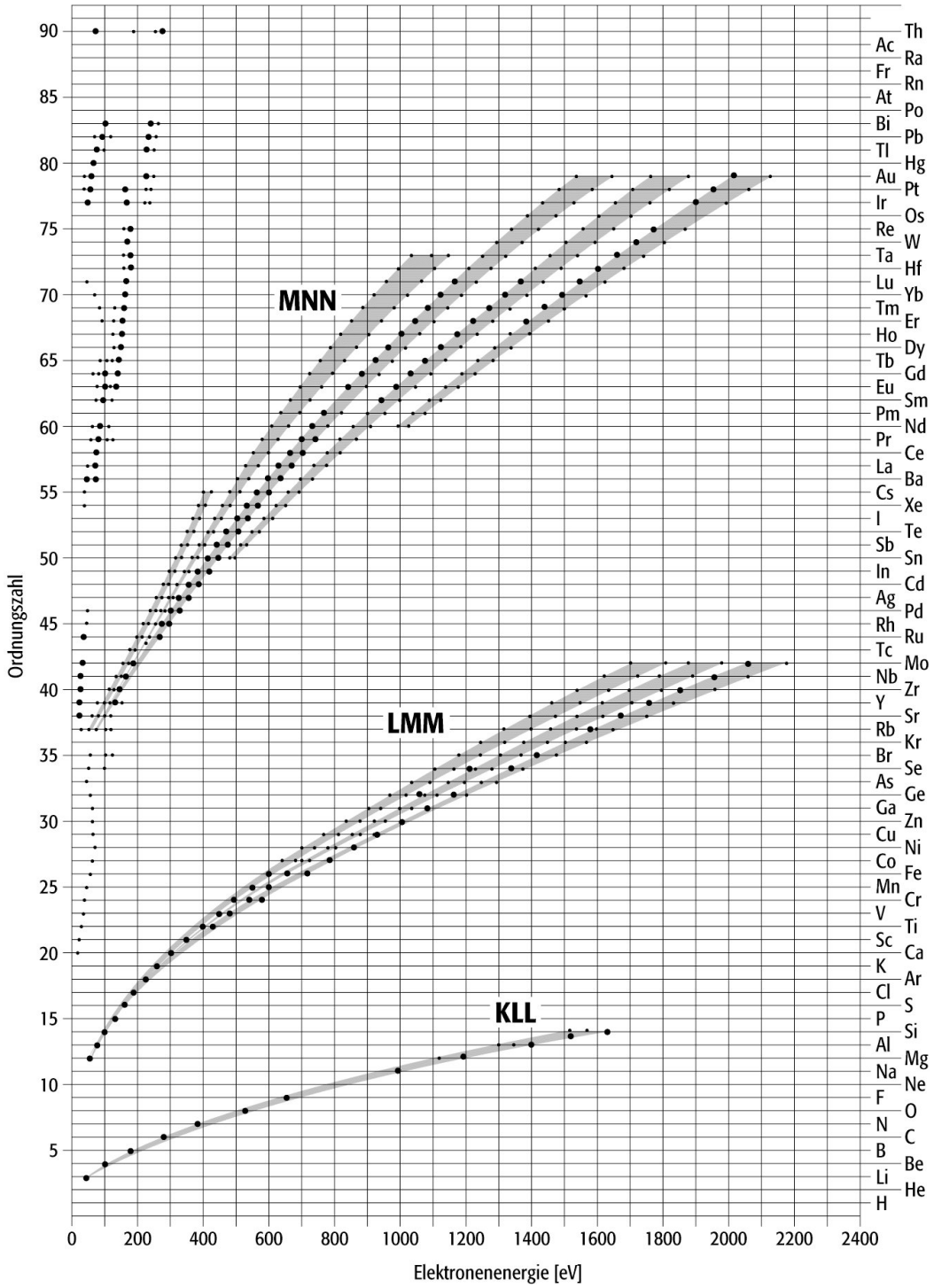

Figure 3.3: Auger electron energy in eV as a function of the element atomic number. The size of the points represents the intensity of the corresponding transition. [26]

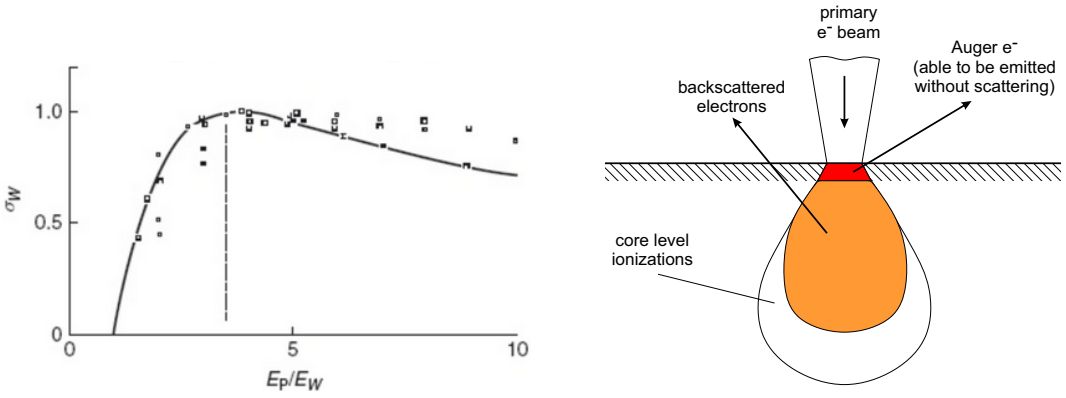

(a) (b)

Figure 3.4: a) Relative ionization cross section $\sigma_w$for the atomic level W as a function of the ratio of the primary electron energy E_p and the electron binding energy in the shell E_W. A maximum can be found around a ratio of $E_p/E_w \approx 3$ [28]. b) Schematic illustration of the sample volume excitation. Auger electrons are produced in a large volume, but only a small fraction contributes to the Auger peak (indicated in red), whereas electrons from the orange marked volume superimpose the Auger transitions as a background.

used with an energy of 1486 eV and 1256 eV, respectively. The high energy photons and electrons lead to an excitation of atoms in a large sample volume (see Figure 3.4b). The spectra are superimposed by a high electron background, which consists of secondary electrons and scattered primary electrons.

However, the information depth is limited by the inelastic mean free path (IMFP) of the Auger electrons and corresponds to typically a few atomic layers [29]. The IMFP is an empirical relationship between the average distance between inelastic collisions and the electron energy. It should be noted that an electron may undergo elastic collisions between inelastic events and hence the trajectory between the events may not be a straight line. The attenuation length λ, which is a general term and can be applied for any radiation passing through matter, describes the transmission probability of the material to the radiation. The attenuation coefficient μ describes the fraction of the radiation removed as it passes through a thickness Δx of the material in the limit Δx$\rightarrow$ 0:

$$\mu = \lim_{\Delta x \to 0} \frac{1 - \frac{I}{I_0}}{\Delta x} \tag{3.2}$$

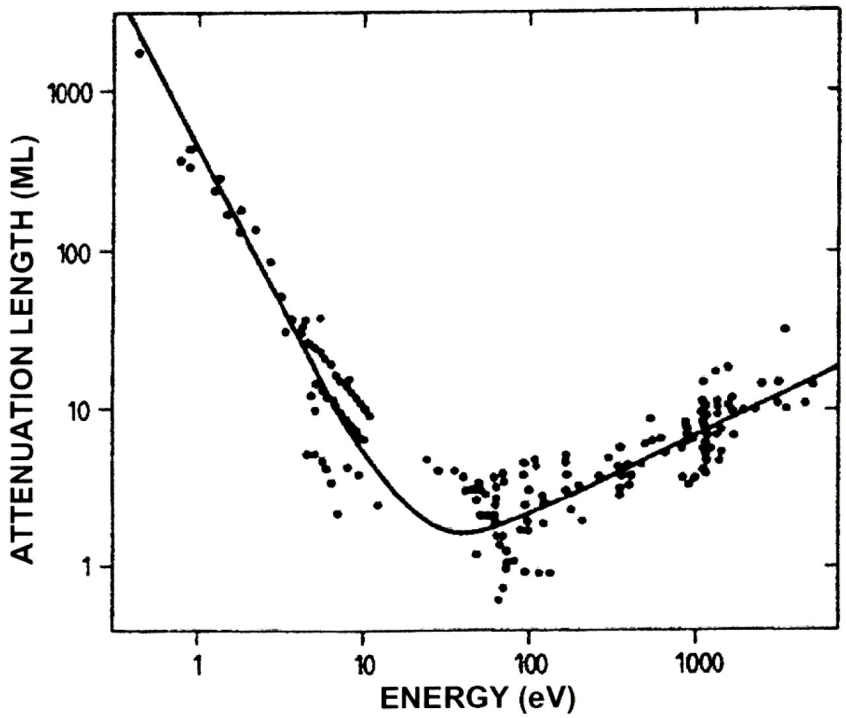

Figure 3.5: Attenuation length of electrons in a solid as a function of the kinetic energy [30]. The data points represent different elements and transitions therein.

The attenuation length λ is the reciprocal term of the attenuation coefficient:

$$\lambda = \frac{1}{\mu} \tag{3.3}$$

The experimentally determined energy-dependent course of λ is shown in Figure 3.5 and can be described by the empirical equation:

$$\lambda \propto \frac{1}{E^2} + 0.054 \cdot \sqrt{E} \tag{3.4}$$

Hence, in conventional Auger electron spectroscopy, the highest surface sensitivity can be reached by studying low energy Auger transitions at about 40 eV. Due to the enormous number of scattered electrons from the ionization mechanism, this low energy range has the highest background level.

3.1.3 Positron annihilation induced AES

Positron annihilation induced Auger electron spectroscopy makes use of a fundamentally new method for the excitation of Auger electron emission. Slow positrons are used to create the core ionization of an atom by positron-electron annihilation. PAES has been shown to have significant advantages over conventional AES, which are discussed in this section. The technique has been first demonstrated in 1987 by Weiss et *al.* [31]. Subsequent studies have shown that PAES is able to eliminate the very large collisionally induced secondary electron background, which in conventional techniques is present under the low energy Auger peaks. Slow positrons with an energy of only 20 eV are used induce the Auger process and hence enable nearly background-free spectra in the range of the Auger transitions, which usually start at about 30 eV in case of core level transitions [32]. Secondary electrons cannot be created through collisional processes with energies in excess of the kinematic edge energy E_k given by

$$E_{sec} \leq E_k = E_p - \Phi_- + \Phi_+ \tag{3.5}$$

where E_{sec} is the kinetic energy of with which the secondary electrons leave the surface of the sample, E_p is the energy of the primary positron beam and Φ_- and Φ_+ represent the electron and positron work function, respectively. The background-free spectra of Auger transitions can be used to study features of the Auger peak more detailed. The spectral intensity on the low energy side of the peak contains information on intrinsic final state effects such as shake up and shake off. Hence, the elimination of the secondary electron background is particularly useful to determine the lineshape of low energy Auger transitions. In addition, PAES is regarded as a truly non-destructive method since the annihilation site is independent of the implantation site, due to the diffusion length of the thermalized positron. When obtaining PAES spectra, the energy dose to the surface is five orders of magnitude lower compared to EAES [7].

However, the most important advantage of PAES using low energy positrons is the outstanding surface sensitivity. As discussed more detailed in Section 2.2, positrons become localized in the image potential well just outside of the surface before they annihilate. The vast majority of the positrons is trapped in the surface potential when diffusing through the sample [33]. Consequently,

the surface trapped positrons annihilate almost exclusively with atoms at the surface and thus nearly all of the Auger electrons originate from the topmost atomic layer of a sample intrinsically [11,31]. The top layer sensitivity of PAES was first confirmed in a series of vapor-deposited Pd films on a Cu(100) surface, comparing the results of PAES, EAES and low energy electron diffraction (LEED) [34, 35]. As a consequence of the element specific positron affinity, different elements at the surface can be detected with enhanced sensitivity [36]. The surface selectivity of PAES was demonstrated by a series of measurements on Cu single crystals with varying coverage of S overlayers [37]. This possibility can be used for the study of surface chemistry and the identification of adsorption sites demonstrated e.g. in the system O/Au/Si(100) [11, 38], which is crucial for catalytic reactivity and selectivity.

For the initiation of the Auger process, the ionization of a core level is a fundamental prerequisite. The annihilation probability of positrons with electrons from the core level is up to approximately 11 % [11]. A table of the calculated core annihilation probabilities can be found in Table A.3. The Auger electron yield was shown to be about two orders of magnitude higher in PAES than in EAES [29, 39].

PAES was successfully employed in a variety of experiments e.g. Se passivation of Si(001) [40], for highly-sensitive detection of impurities on carbon nanotubes [41], adsorption and desorption of O from an oxidized Cu(100) surface [42], studies on the adsorption of H and O on Si(100) [43] to measure the sticking coefficient, high resolution measurements of Auger transitions [44, 45], and growth of Cu and Fe islands on Pd [44]. In particular, using time-dependent PAES, the surface segregation in the system Cu/Pd was observed with a characteristic time constant of 83 minutes [19].

The main drawback of PAES were the very long measurement times on the order of 15-20 days (see e.g. [46]) due to the low intensity of the positron beams generated from radio nuclide sources, where self absorption limits the strength of the source. This was overcome by using the high-intensity positron beam at the NEutron induced POsitron source MUniCh (NEPOMUC) located at the research reactor Heinz-Maier Leibnitz at the Technische Universität München [47]. NEPOMUC provides an intensity of about 10^9 monoenergetic positrons per second with an energy of 1 keV [48, 49] and reduces the measurement time

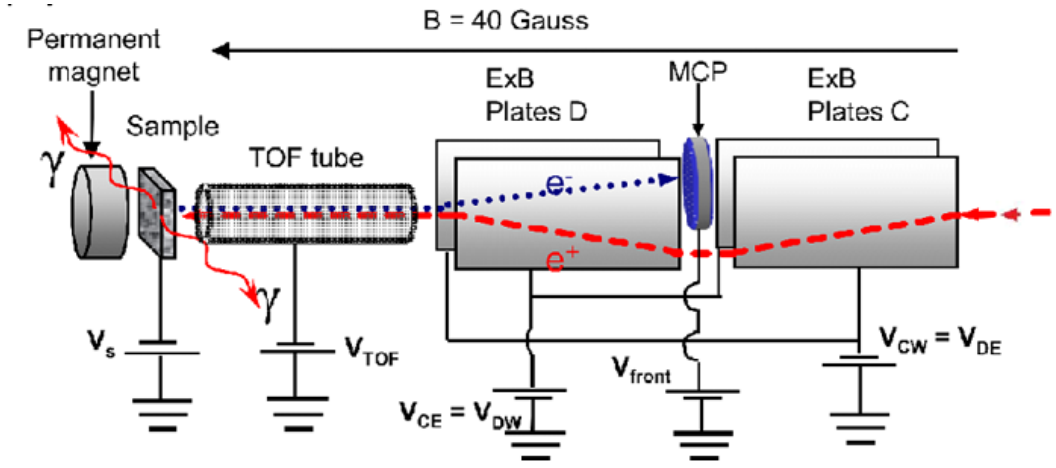

Figure 3.6: Schematic diagram of a time-of-flight energy analyzer system of a PAES setup. [51]

for a single PAES spectrum to a few minutes [50]. The setup will be described in Chapter 4. For the recording of PAES spectra, the energy of the Auger electrons is evaluated using an hemispheric energy analyzer that employs an electric field to allow the passage of only those electrons that have a given specific energy. This setup can also be used for complementary characterization with conventional AES and XPS.

Another approach to record PAES spectra is a time-of-flight (TOF) setup, see e.g. [51], where the time difference between the positron annihilation and its detection on a Micro-Channel Plate (MCP) detector is measured. The element specific kinetic energy of the Auger electrons leads to different flight times. A schematic sketch of the setup is shown in Figure 3.6. The incident positron beam coming from the right is guided by an axial magnetic field.The E×B plates C and D in Figure 3.6 serve to deflect the positron beam around the MCP. This acts as an energy filter for the positron beam as well as directs the electrons emitted from the sample towards the MCP. The permanent magnet parallelizes the electrons emitted from the sample and allows the collection of electrons at nearly 2π solid angle. A 0.6 m long TOF tube is used to provide a field free flight path. The total flight path of the electrons from the sample to the plate is approximately 1 m.

When an electron is detected at the MCP, the detector provides a timing signal. A BaF_2 scintillator is used to detect the 511 keV annihilation radiation of the positron with an electron from the sample, which also provides a time

signal. The time between the annihilation of the core electron and the emission of the Auger electron is on the order of 10^{-14} s, whereas the time taken by Auger electrons to travel from the sample to the MCP is about 10^{-6} s [51]. The time of flight is determined from the time difference between the timing signal from the MCP and the BaF_2 detector.

From the flight time Δt, the kinetic energy of the electrons E_{kin} can be calculated as follows

$$E_{kin} = \frac{1}{2} m_e v^2 = \frac{1}{2} m_e \cdot \frac{L}{\Delta t} \tag{3.6}$$

where m_e denotes the electron mass and L is the flight path. The main advantages of a time-of-flight setup are the large solid angle of collected electrons and the acquisition of all electron energies at the same time, which is not possible with a hemispheric energy analyzer. However, the TOF setup cannot be used for the acquisition of complementary XPS spectra.

3.1.4 Surface sensitivity of PAES, EAES and XAES compared on Ni/Pd

In order to enable the comparison of the surface sensitivity using different analysis techniques, samples with 0.1 ML and 1 ML Ni on Pd were prepared. The spectra recorded with PAES, EAES and XAES for the Ni/Pd system are shown in Figure 3.7.

The PAES spectrum of the sample with 0.1 ML Ni on Pd shows significantly three Auger transitions of the elements (Figure 3.7 a). Due to the varying core annihilation probabilities for the Pd levels – Pd 4s: 1.51 % and Pd 4p: 6.07 % [11] – , the Pd N_1VV transition is less distinct than the Pd $N_{2,3}VV$ peak. Ni and Pd have the same Z_{eff} leading to the same probability for Auger relaxation [24]. Due to the low positron energy the secondary electron background induced by the positron beam ends at 20 eV. Generally, the line shape of the peaks is smeared out to lower energies due to scattered Auger electrons. The background at higher energies arises also from scattered high-energy Auger electrons.

Despite of shorter measurement times, EAES and XAES show much higher statistics than PAES, due to the high electron and photon flux, respectively.

However, due to the high secondary electron background in this most surface sensitive energy range, the transitions are much less pronounced. Pd is visible in both spectra, especially the Pd $N_{2,3}VV$ transition, due to the higher number of electrons in the Pd 4p shell. The Ni $M_{2,3}VV$ transition of the 0.1 ML Ni is also visible in XAES but not in the EAES spectrum.

The PAES spectrum of the sample with 1 ML Ni on Pd shows almost only Ni whereas the Pd substrate is hardly visible, pointing out the intrinsic high surface sensitivity of PAES. EAES and XAES show a significant Ni peak. The Pd substrate, especially in the EAES spectrum, is clearly detectable, as expected due to the IMFP of electrons.

3.2 X-ray photoelectron spectroscopy

Among all contemporary surface characterization methods X-ray Photoelectron Spectroscopy (XPS) is the most widely used. It provides a high information content and can be applied easily to a wide variety of samples. For this reason it is often called Electron Spectroscopy for Chemical Analysis (ESCA). The good theoretical description of the fundamental mechanisms of XPS allows a detailed interpretation of the spectra, as well as quantitative statements. The overall process is known as photoelectric effect, which was first interpreted by Albert Einstein in 1905 [53]. A schematic explanation of XPS compared with Auger electron spectroscopy induced by electrons, X-rays and positrons is shown in Figure 3.8. A comparison of the typical spectra of all three acquisition techniques using the example of Ni can be found in Figure 3.9.

In a basic XPS experiment, the sample is illuminated with soft X-rays, capable to penetrate several micrometers into the bulk of the sample. When a photon is absorbed by an atom, a bound electron is released. This process is called photoionization. As described for conventional AES in Section 3.1.2, due to the attenuation length of electrons in the solid, only electrons near the surface can leave the sample, which is the so-called photoemission. The kinetic energy E_K of the photoelectrons is given by:

$$E_K = h\nu - E_B - \Phi_- \tag{3.7}$$

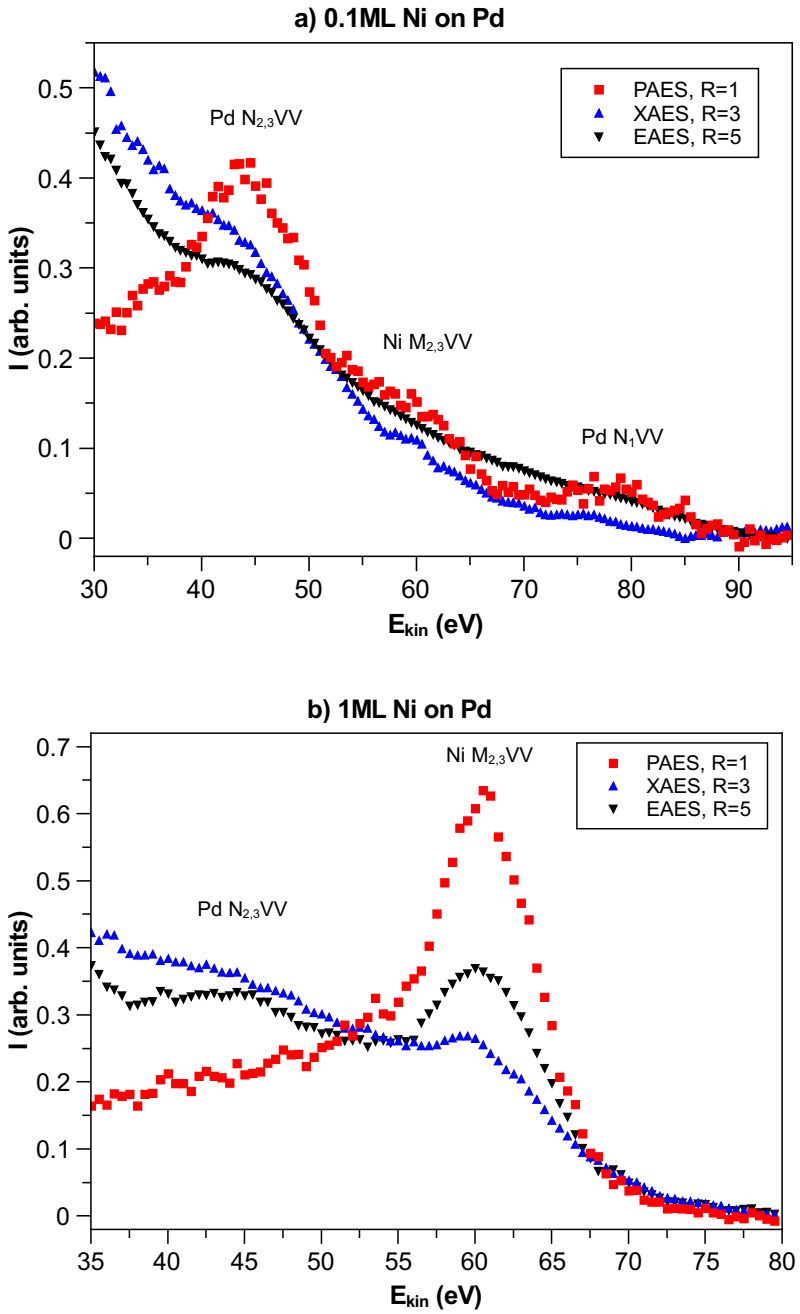

Figure 3.7: Comparison of PAES with conventional AES on (a) 0.1 ML Ni on Pd and (b) 1 ML Ni on Pd. In the PAES spectra 0.1 ML Ni on Pd is clearly visible, whereas at 1 ML Ni on Pd almost no Pd substrate is detected. Note the high electron background at EAES and XAES. All spectra are normalized to the same number of events in the spectrum. Recording mode: FRR, retarding ratios R are given in the legend. Published in [52]

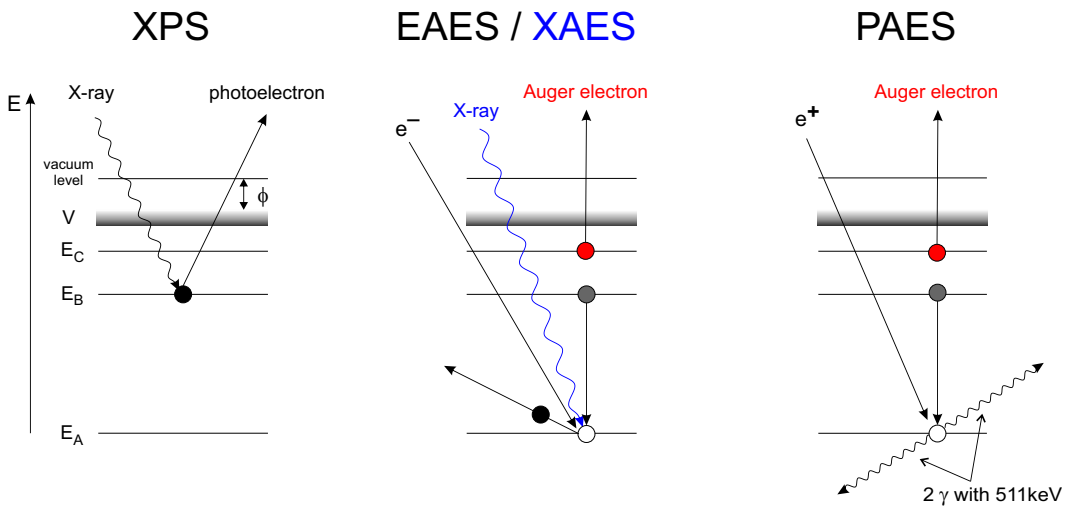

Figure 3.8: Scheme of XPS, conventional AES induced by electrons or X-rays and PAES.

where $h\nu$ is the energy of the photon, Φ_- denotes the electron work function and E_B the binding energy of the electron. In commercial X-ray sources typically the K_α line of Mg, Al or Cu with an energy of 1256 eV, 1486 eV and 8028 eV, respectively, are used. The photoemission process is extremely rapid (10^{-16}s) [28], leading to very sharp peaks in the spectra. The emission of a photoelectron leaves the atom in an ionized state. Therefore, Auger transitions can be observed in every XPS spectrum, too.

3.2.1 Elemental surface composition

The reason for the widespread use of XPS is the simple quantification of the photopeaks in the spectra, whereby the proportion of different elements on the sample surface can be determined. Therefore, XPS can be used to monitor the surface contamination due to the residual gas in the chamber or the thermal induced desorption of adsorbates from surfaces. The latter is shown in Figure 3.10. The effect of thermal surface cleaning is observed on a single crystalline Ni(100) foil with a thickness of 100 nm, which was previously exposed to air. The temperature is increased stepwise from room temperature to 600 °C and the fraction of Ni and the main contaminations, C and O, were determined from the recorded XPS spectra at each temperature step. The largest increase of the Ni signal was observed at temperatures between 200 °C and 300 °C, were

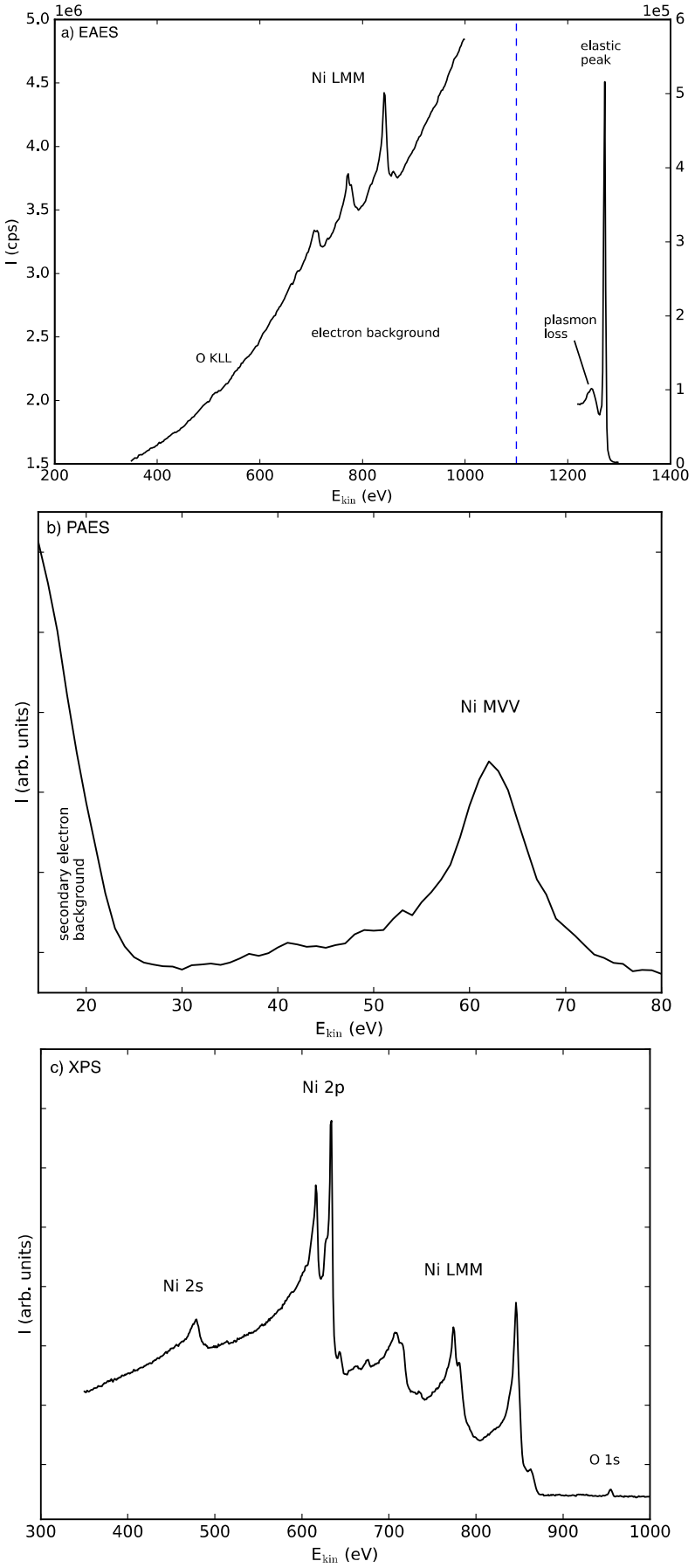

Figure 3.9: Typical spectrum of Ni recorded with (a) EAES, (b) PAES and (c) XPS.

a large amount of C and O were desorbed from the Ni surface. The details of the quantification method of XPS spectra is discussed in Chapter 5.

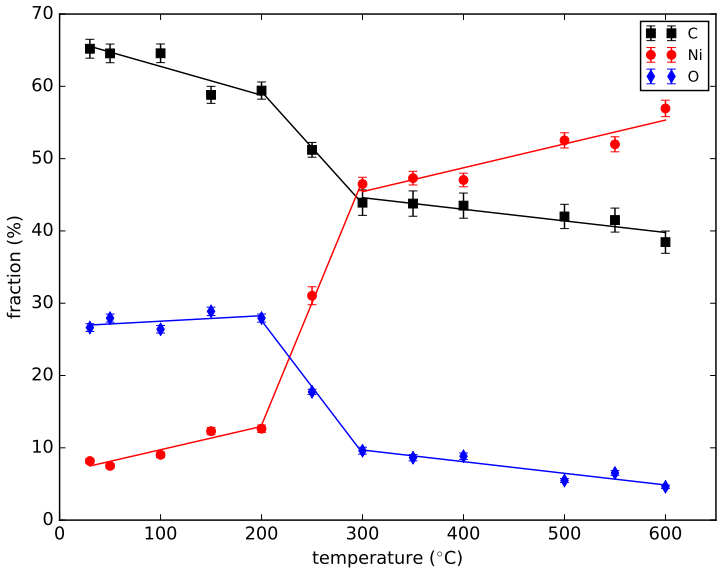

Figure 3.10: Temperature induced surface cleaning of a Ni(100) foil with a thickness of 100 nm after exposure to air observed with XPS. The main contaminations of the foil were determined to be C and O, which were mostly desorbed from the surface at 300 °C. The lines are to guide the eye.

However, H is not directly detectable with XPS, as it does not produce a core photoelectron peak [54]. The H 1s electron is a valence electron and as such participates in chemical bonds. Any signal only appears in the valence band like for example in case of Pd [55]. However, the photoionization cross-section is also very low [27].

3.2.2 Chemical specificity of XPS

Since the electrons can be ejected from a tightly bound core level as well as from weakly bound valence levels or molecular orbitals, the spectra contain a variety of information about the chemical state of a sample. The core levels have small chemical shifts depending on the chemical environment of the atom that is ionized. This allows the determination of the chemical structure. This chemical specificity is the special feature of XPS. Thus, XPS does not only characterize the chemical elements of the surface, but also their ionization

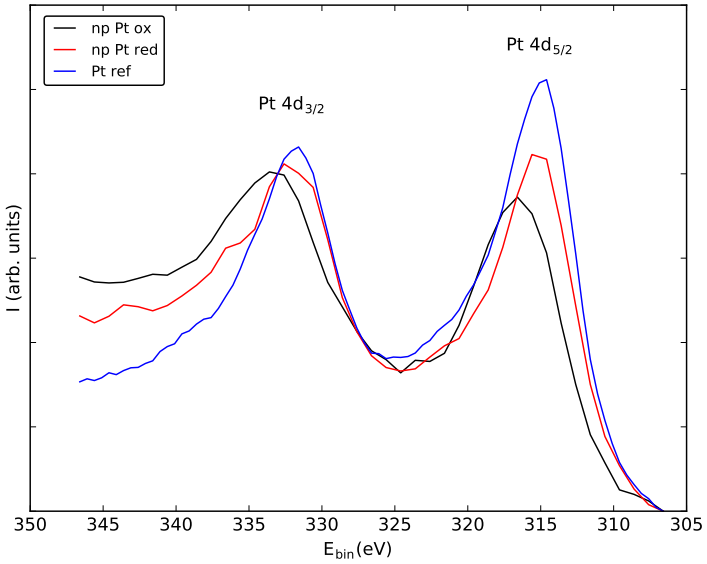

Figure 3.11: Demonstration of the chemical specificity of XPS using the example of three different chemical states of Pt. A metallic Pt foil used as reference is compared with nanoporous Pt clusters, which were oxidized or reduced.

states or small shifts in the binding energy due to chemical bonding with other elements. As an example, the peak shifts of the Pt 4d level are shown in Figure 3.11. Three states of Pt are compared. As a reference, a clean metallic Pt foil is shown in blue and compared with reduced (red) and oxidized (black) nanoporous Pt. An energy shift of about 3 eV can be observed for the different states.

In order to resolve the superimpositions of various binding energies or features of the band structure at the Fermi energy as good as possible, an optimum energy resolution is necessary. Apart from the detector resolution and the natural line width of the photopeak, determined by the lifetime of the respective state, the energy distribution of the incident X-ray is a crucial factor. The characteristic K_α energy is an unresolved doublet resulting from the transitions $2p_{3/2} \rightarrow 1s$ and $2p_{3/2} \rightarrow 1s$. Therefore, sometimes it is called $K_{\alpha 1,2}$. However, weaker satellite lines resulting from other transitions can occur. For example in case of Al, the $K_{\alpha 3}$ with an intensity of 7.8 % of the K_α intensity and a separation of 9.6 eV is present, leading to satellite peaks in the spectra. To get rid of these peaks and reduce the line width of the K_α a monochromatic X-ray source can be used. Monochromatic Al K_α X-rays are produced by focusing on

and diffraction by a thin disc of α-quartz with a <1010> orientation, reducing the line width from 0.85 eV to 0.3 eV.

3.2.3 Surface sensitivity of XPS

As in conventional Auger electron spectroscopy, the surface sensitivity of XPS is given by the energy-dependent attenuation length of the ejected photoelectrons, see Figure 3.5. 95 % of the information obtained by XPS comes from three attenuation lengths of the surface. This is called the sampling depth of XPS. However, the signal intensity obtained from a layer of atoms buried a distance z beneath the surface is less than the signal intensity at the surface. The correlation is given by the Beer-Lambert law

$$I_z = I_0 \cdot \exp\left(-\mu \cdot z\right) = I_0 \cdot \exp\left(-\mu \frac{d}{\sin\Theta}\right) = I_0 \cdot \exp\left(\frac{-d}{\lambda \cdot \sin\Theta}\right) \qquad (3.8)$$

where λ is the photoelectron attenuation length and Θ the photoemission angle with respect to the surface plane. If electrons are collected over a range of angles from near normal emission to near grazing emission then the analysis depth changes. A higher surface sensitivity is reached at higher grazing angles. This enhancement of surface sensitivity can be shown experimentally using a Pd substrate with a Ni cover layer with a thickness of 0.7 ML. Figure 3.12 shows the ratio of the intensities of Ni and Pd versus the detector angle. At higher grazing angles, the Ni signal becomes more pronounced than when recording perpendicular.

When analyzing the Ni 2p photopeak, a change in chemical composition can be found, see Figure 3.13. The arising of side peaks at more surface sensitive angles at binding energies of 857 eV and 874 eV indicates a chemical bond at the surface, which corresponds to $Ni(OH)_2$ [56].

However, when XPS is used for depth profiling, the determined atomic fractions have to be evaluated carefully from the photopeak intensities, as sampling depths depend on the kinetic energy of the photoelectrons. Table 3.2 summarizes the sampling depth for selected elements as a function of the kinetic energy and the detector angle. The sampling depth increases with increasing kinetic energy, leading to a better visibility in the spectra.

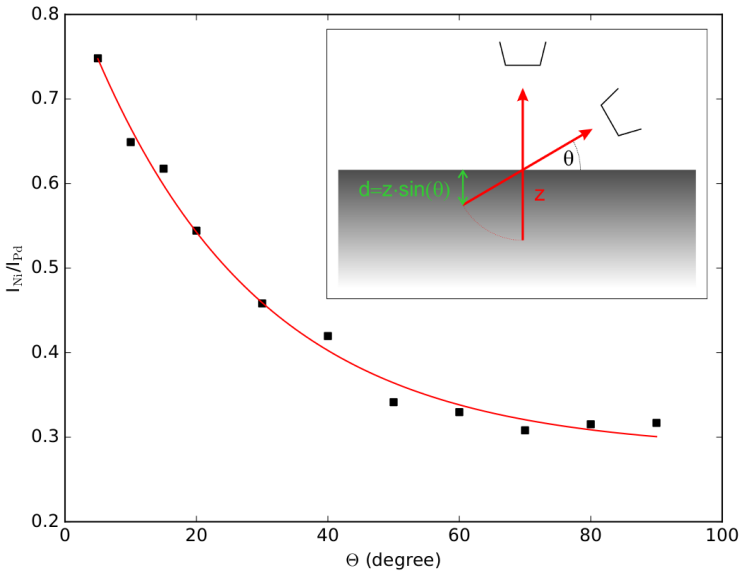

Figure 3.12: A higher surface sensitivity of XPS can be achieved by collecting photo electrons at more grazing emission angles Θ. This can be demonstrated experimentally by plotting the ratio of Ni to Pd versus the angle to the detector of a Pd substrate covered with 0.7 ML of Ni.

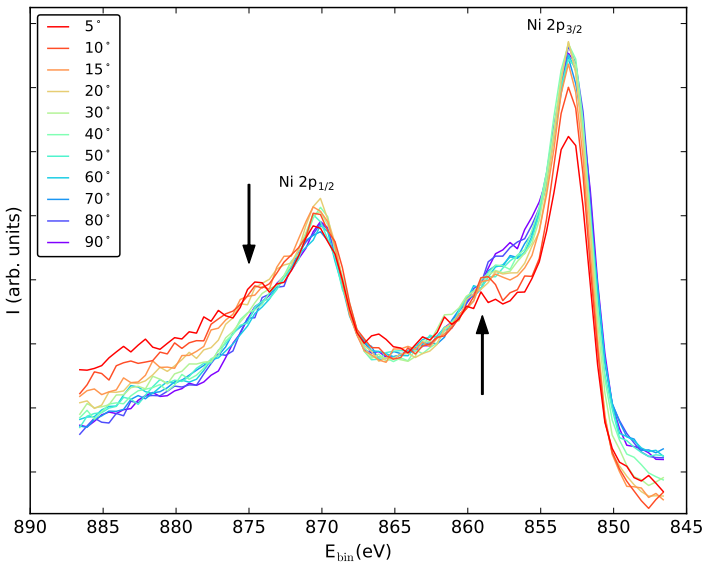

Figure 3.13: Normalized spectra of the Ni 2p photo peak measured at detector angles between 90 ° and 5 °, which is most surface sensitive. The presence of side peaks (see arrows) at low angles indicates a chemical bond at the surface. The energies correspond to $Ni(OH)_2$.

core level	kinetic energy (eV)		sampling depth (nm)					
	Mg Kα	Al Kα	Mg Kα			Al Kα		
			10°	45°	90°	10°	45°	90°
O 1s	723	956	1.0	4.1	5.8	1.3	5.2	7.3
C 1s	967	1200	1.3	5.2	7.3	1.5	6.2	8.7
Si 2p	1152	1385	1.5	5.9	8.4	1.7	6.9	9.7

Table 3.2: Sampling depths as a function of the core level kinetic energy and the detector angle for selected elements. The sampling depth is defined as $3{\cdot}\lambda(E)\sin(\Theta)$, where 95 % of the signal originate from. λ denotes the energy dependent attenuation length, see also Figure 3.5 and Θ is the detector angle. [57]

3.3 Further techniques for surface analysis

Apart from Auger electron spectroscopy, XPS and Scanning Tunneling Microscopy (STM), which will be introduced in Section 4.3, several other techniques are available for surface analysis and will be briefly presented in this section.

Closely related to XPS is the Ultraviolet Photoelectron Spectroscopy (UPS). The kinetic energy of photoelectrons emitted by molecules which have absorbed ultraviolet photons. Due to the lower photon energy compared to XPS, the studies are focused to organic molecules adsorbed to surfaces. Another application of UPS is the determination of the work function of a material.

3.3.1 Scanning techniques

In scanning probe techniques one tries to obtain an image of the surface structure directly. STM is based on the quantum tunneling effect, leading to a tunneling current when a sharp, biased tip is approximated a few Angstroms close to the sample surface. The electron density distribution at the surface is measured, which is related to the atom's positions. Therefore, STM is limited to conductive samples. The Atomic Force Microscope (AFM) is based on the effect of forces between atoms or molecules described by the Lennard-Jones potential. In AFM the cantilever has a sharp, force-sensing tip at its end, which interacts with the sample surface. As a result of variations in the interaction, the deflections of the cantilever can be measured containing the topographic information.

3.3.2 Scattering techniques

Secondary ion mass spectroscopy (SIMS) is an ion beam analysis technique for the characterization of the top few micrometers of a sample. The primary ions, most commonly O^-, Ar^+, Xe^+, etc. with energies up to 20 keV erode the sample surface, where secondary elemental or cluster ions of the sample material are ejected and analyzed in a detector with regard to their energy, mass and charge. The technique has an outstanding sensitivity in composition analysis. Detection limits of $10^{13} - 10^{18}$ atoms per cm^3 for impurities in semiconductors were reported [58, 59]. SIMS is an inherently destructive method, since it gives the elemental composition of a sample as depth profiles. Therefore, it generally does not provide structural information.

Rutherford Backscattering Spectrometry (RBS) is another ion beam analysis technique. Most commonly alpha particles with an energy of 1-4 MeV or protons of 100 keV to 2 MeV are used and the elastic Coulomb scattering between the projectile and the target nuclei is analyzed. The method is most suitable to characterize the structure and composition variation or impurity distribution of mainly inorganic compounds as a function of depth with a resolution of a few hundreds Angstrom.

Low Energy Ion Scattering (LEIS) enables studies of the structure and composition of a surface by detecting ions scattered off the surface. The ion energy is usually in the range of 100 eV to 10 keV. The lower the ion energy, the higher the surface sensitivity. LEIS is closely related to RBS, differing primarily in the energy range of the ion beam used to probe the surface. LEIS is unique in its sensitivity to both structure and composition of surfaces. Additionally, LEIS is one of a very few surface-sensitive techniques capable of directly observing hydrogen atoms [60].

3.3.3 Diffraction techniques

As an electron beam with an energy of 150 eV has a de Broglie wavelength of approximately 1Å, which is similar to the lattice spacing in a crystal, it is suitable for diffraction experiments.

Low Energy Electron Diffraction (LEED) is one widely used technique to study surface superstructures as well as effects of adsorbates to a surface and

particle	penetration depth (Å)
photon	10 000
electron	20
ion	10

Table 3.3: Comparison of the penetration depth of particles with a primary energy of 1 keV. [28]

their alignment on the surface structure of single crystalline materials. In LEED, the elastic backscattering of low energy electrons with an energy of typically 10-600 eV incidenting perpendicularly to the surface is analyzed, to determine the atom positions. LEED is not element-specific and thus cannot be used to determine surface elemental composition.

In Reflection High Energy Electron Diffraction (RHEED) an electron beam with an energy of 5-30 keV is directed at a glancing angle of usually $<5°$ at a single crystal. The diffraction pattern of the electrons is made visible by a phosphor screen to recalculate the atom's positions. RHEED is one of the few techniques that can monitor the epitaxial growth of thin layers in-situ, where extreme purity and precision is necessary.

RHEED has a counterpart by using positrons (RHEPD) with the same kinetic energy to observe the diffraction pattern generated by positron small angle scattering at a surface. Since positrons have the opposite charge of electrons, the particle ion-core interaction and the crystal potential differs and at a critical angle total reflection can occur. RHEPD below the critical angle is extremly sensitive to the topmost atomic surface layer. Total reflection is also used in X-ray diffraction (XRD), but the critical angle is usually less than $0.2°$. However, due to the higher penetration depth of photons this still amounts to a few nanometers. Table 3.3 compares the penetration depth into a sample of different particles with an energy of 1 keV.

3.3.4 Radiation damage

From the surface sensitivity point of view, referring to Table 3.3 one might prefer ions for surface studies, due to their low penetration depth. However, the bombardment of a sample surface with ions leads to damages in the surface structure, such as ejection of atoms, generation of dislocations, atom exchange

technique	primary flux ($cm^{-2} \cdot s^{-1}$)	primary energy (eV)	power (W/cm^2)
XPS	10^{14}	1400	$2 \cdot 10^{-2}$
LEED	10^{15}	50	$5 \cdot 10^{-3}$
SIMS	10^{10}	3000	$3 \cdot 10^{-6}$
PAES	10^{7}	20	$3 \cdot 10^{-11}$

Table 3.4: Typical flux, particle energy and resulting power dissipated in different surface analysis techniques [28].

or adsorption. As photons penetrate deeply into the sample, the energy is not deposited in the near surface. However, the power dissipated by the sample surface needs to be considered, especially in case of weakly bound adsorbates. Table 3.4 summarizes the typical flux, particle energy and dissipated power of selected surface analysis techniques using photons, electrons, ions and positrons. It turns out that the radiation damage due to the dissipated power is lower in case of ions than for X-rays. Therefore, all aspects of the interaction of the projectile and the sample material need to be considered when choosing the appropriate analysis technique.

For this reason surface analysis with PAES turns out to have several advantages. The surface sensitivity is an intrinsic feature of low energy positrons due to the trapping in surface states. On the other hand it is truly non destructive, since the energy of the positrons is low and the annihilation site is independent from the implantation site due to the diffusion of the thermalized positron.

Chapter 4

The Surface Spectrometer at NEPOMUC

In this chapter, the spectrometer used for the surface analysis will be introduced. The unique feature of the spectrometer is the combination of a variety of well established surface analysis techniques with Auger electron spectroscopy induced by positrons annihilation. To overcome the usually low count rate in PAES, the spectrometer is connected to the world's most intense positron source NEPOMUC, which will be presented in the first part.

4.1 The positron source NEPOMUC

Positrons can be generated in β^+ decay processes or by pair production from high energy γ radiation. In laboratories, the most prominent positron source is a radio nuclide of Na:

$$^{22}_{11}\mathrm{Na} \rightarrow ^{22}_{10}\mathrm{Ne} + \beta^+ + \nu_\mathrm{e} \tag{4.1}$$

It combines the advantages of a high positron yield of 90% and a half-life of 2.6 years. Self absorption limits the strength of the source to a few GBq [4]. The positrons released in the β^+ decay of ^{22}Na show a continuous energy distribution up to 544 keV. For surface studies, the implantation depth of positrons into the sample has to be as small as possible. In order to generate and focus a beam, which can be implanted to a dedicated depth into the sample, monoenergetic positrons are necessary. Therefore, moderation of the positrons is necessary,

which has a small yield in case of the broad energy distribution of ^{22}Na, since most of the positrons are implanted too deep into the moderator to reach the surface within their diffusion length after thermalization. Due to the low resulting intensity, measurement times for positron annihilation induced Auger electron spectroscopy studies with radio isotopes extend to several days [61].

To achieve higher positron intensities the principle of pair production is used. Gamma quanta with an energy of more than twice the electron mass can produce a pair of electron and positron in the electrostatic field of a nucleus, which takes the recoil momentum:

$$\gamma \rightarrow e^+ + e^- \tag{4.2}$$

High intense γ-sources are available at accelerators from Bremsstrahlung targets or at research reactors from nuclear processes. The cross section for pair production increases quadratically with the nuclear charge number Z, therefore high Z materials such as Pt, Ta or W are preferably used as converters.

At the research neutron source Heinz Maier-Leibnitz (FRM II) in Garching the positron source NEPOMUC is located. For positron production the high flux of thermal neutrons is combined with a nuclear reaction of Cd, which gave the source its name NEutron induced POsitron source MUniCh (NEPOMUC):

$$^{113}\mathrm{Cd} + \mathrm{n} \rightarrow ^{114}\mathrm{Cd} + \gamma \tag{4.3}$$

The isotope ^{113}Cd has a huge cross section for the capture of thermal neutrons of 20600 barn [62]. The γ radiation released in the nuclear reaction have an energy of up to 9.05 MeV and are converted to pairs of electrons and positrons in a structure of Pt foils. Pt has a negative work function for positrons of -1.95 eV [63], so the positrons are spilled out with a discrete energy into the vacuum, where they are formed to a beam by an electrostatic lens system and guided magnetically to the experiment. A cross sectional view of the NEPOMUC source is shown in Figure 4.1.

The NEPOMUC source provides the world highest intensity of more than 10^9 moderated positrons per second [49]. An important criteria for the beam quality of an ensemble of particles is the brightness, which is defined as the ratio of the beam intensity and the phase space volume. When focusing a

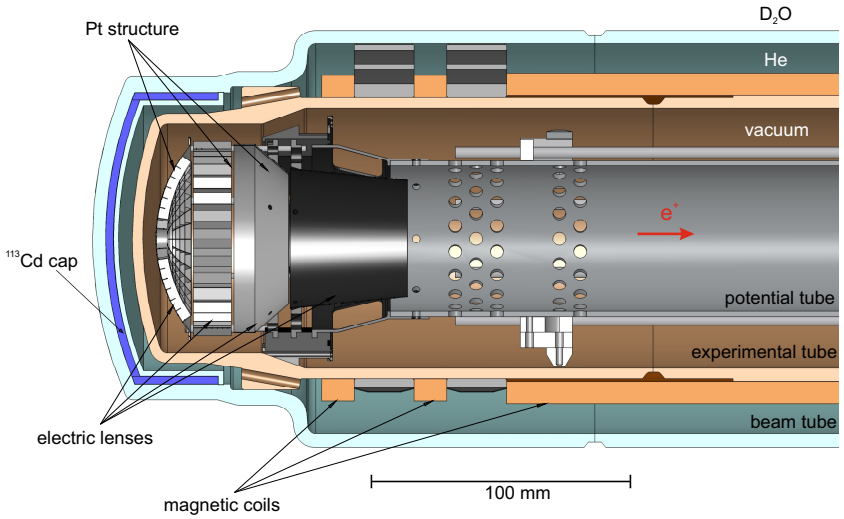

Figure 4.1: Cross sectional view to the NEPOMUC source, see [64]. Thermal neutrons from the reactor are used for the nuclear reaction ^{113}Cd(n,γ)^{114}Cd. The γ's are converted to electron-positron pairs in Pt and the positrons are focused to a beam by the electric lens system and guided magnetically to the experiments.

beam, one is limited by Liouville's theorem, which states that the phase space volume remains constant in the presence of conservative forces. Therefore, to enhance the brightness, the beam is focused to a W single crystal, which has a negative work function for positrons of Φ_+=-3.0 eV [7]. In this process the momentum of the positrons is reduced to the thermal energy, which leads to a lower phase space volume of the beam. By applying a positive potential to the W crystal, the desired kinetic beam energy can be adjusted and is typically set to 20 eV. The intensity of this so-called re-moderated beam is $3{\cdot}10^7$ e^+/s [49], with a beam diameter as the full width at half maximum of less than 2 mm. This beam is used for the measurements shown in the next chapters.

4.2 Overview of the Surface Spectrometer

The surface spectrometer at the positron beam facility NEPOMUC enables an extensive analysis of the sample surface, including its elemental composition as well as its topology combined with on-site sample preparation and storage. During the past years, the spectrometer was continuously upgraded to todays state, shown in Figure 4.2. The spectrometer consists of five interconnected

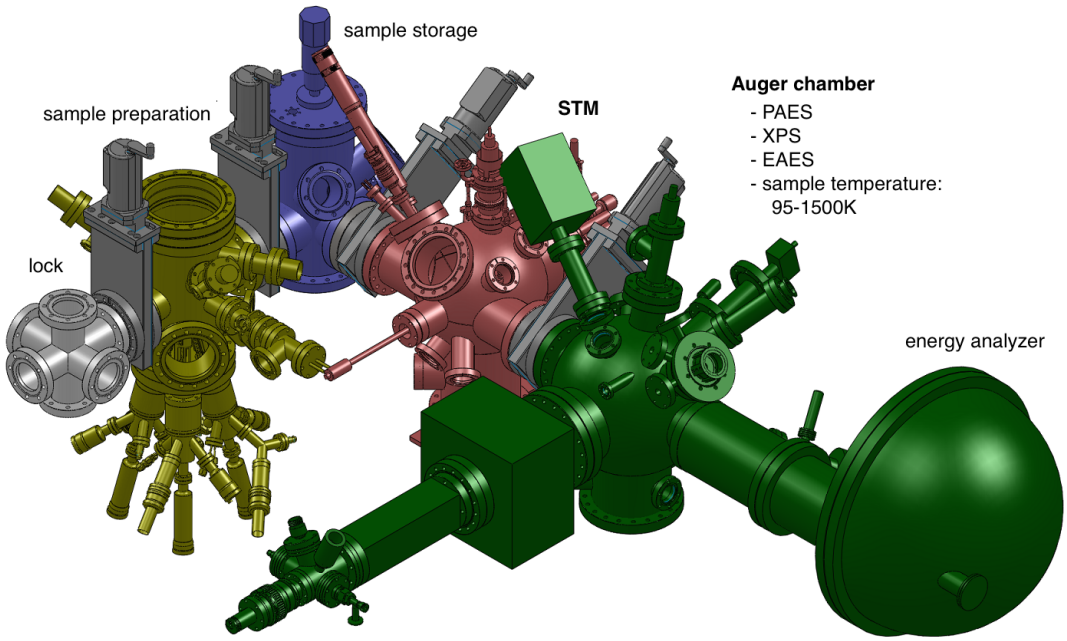

Figure 4.2: The setup of the surface spectrometer at NEPOMUC. See [65].

UHV chambers. The samples are transferred by magnetically linked linear feedthroughs. The most important chambers are those for the preparation of the samples, the STM chamber to study the topography and the Auger chamber for element analysis. The details are described in the following sections.

4.2.1 Sample preparation

Samples can be transfered into the vacuum using the load lock, without influencing the vacuum in the other chambers. This is followed by a further chamber, dedicated for sample preparation and cleaning. It contains a sputter gun with an energy range of 250 eV up to 5 keV, which is operated with Ar of 6.0 purity. To avoid damaging the single crystalline surface of the samples during cleaning with Ar-ions, an energy between 500 eV and 1 keV were used. Sputter yields depend strongly on the projectile energy and the target material. Typical sputter times are in the range of several minutes to an hour. A vanadium foil was used to adjust the beam focus in a way that the FWHM of the Ar ion beam is in the range of the sample size of typically 10 mm in diameter.

Moreover, the chamber houses three independent electron beam evaporators, which are used to prepare samples with a cover layer. In an electron beam

evaporator, a tungsten filament is heated up by an electrical current of about 8 A and the emitted electrons are accelerated towards the target material, which is set to a positive potential of 3 kV. This energy is sufficient for the evaporation of many metals, such as Ni, Ag, Fe. For those materials, a rod with a diameter of 3 mm to 5 mm was chosen. Evaporation from a crucible is preferred for e.g. Al, Cu and Au. To prepare Pt layers, the so called wetted-wire technique was applied. For this, a thin Pt foil is wrapped on a W rod, which is fed to the evaporator. When heating up, the Pt wets the W surface. Due to the lower sublimation temperature the evaporation of Pt begins earlier and the W rod remains. This setup enables thin film deposition with thicknesses from a fraction of an atomic layer up to several 100 nm. For most studies a coverage of only a few atomic layers is needed, hence a low evaporation rate of 0.1 - 0.2 Å/s is chosen, leading to a nominal thickness accuracy of typically 0.01 to 0.02 ML. The evaporation rate is monitored by a Piezo oscillator. The resonant frequency of an exposed quartz crystal is used to sense the mass of deposited films attached to its surface. For a previously defined element, there is a known relationship between the mass of evaporated material and the measured frequency f of the sensor crystal. When measuring the frequency change due to accumulated mass, the film thickness d_{film} can be calculated by the following equation [66]:

$$d_{\text{film}} = \frac{C \cdot \rho_{\text{quartz}}}{\pi \cdot \rho_{\text{film}} \cdot Z \cdot f} \cdot \arctan\left(Z \cdot \tan\left(\frac{\pi \cdot (f_i - f)}{f_i}\right)\right) \tag{4.4}$$

with the crystal specific frequency C, ρ_{x} the densities of quartz and the deposed film, the frequency f_i of sensor crystal prior to depositing any film material on it and Z-factor of the material, representing mechanical interactions between the quartz and the deposed film.

To avoid an influence of temperature on the oscillation frequency during evaporation, the Piezo oscillator is water cooled. The Piezo oscillator can be moved to the sample position. Therefore, the evaporation rate has to be stable over a longer time before coating the sample and is controlled after exposition.

The following chamber marked in blue in Figure 4.2 contains a sample storage place under UVH conditions for up to ten samples, which are stacked vertically one above the other.

4.2.2 STM chamber

For the characterization of the cover layers grown in the preparation chamber the distribution of the evaporated atoms on the substrate surface is one of the key parameters. Scanning tunneling microscopy is an established technique for analyzing the topology of surfaces, see the measurements on Si(111) presented in Section 4.3. The STM installed in the chamber marked in red of the surface spectrometer in Figure 4.2 is an Aarhus HT STM from Specs with a temperature range between 90-1300 K. Cooling is realized by liquid nitrogen and heating by electron bombardment. Another sample storage for five samples is installed in the chamber which has a further place to heat up samples by electron bombardment to more than 1500 K within seconds. The stage can be used for flashing samples. Flashing is an effective way to clean surfaces from adsorbates and favor surface reconstruction. In this process the sample is heated up to temperatures close to the melting point within seconds, while the sample holder stays close to room temperature, due to the low thermal contact between sample and sample holder.

4.2.3 Auger chamber

The main analysis chamber shown in green in Figure 4.2 connects the spectrometer to the NEPOMUC beamline. The positron beam passes a magnetic field termination at the chamber flange and is guided electrostatically through a lens system, which focuses the beam onto the sample. The lens system is shown in Figure 4.3. It consists of eight cylindrical lenses, of which the penultimate lens is four-segmented to deflect the beam to the sample center. The lens voltages are given in Table B.1. For PAES measurements, the energy of the positrons is set to a value as low as possible for beam guiding. This enhances the surface sensitivity of PAES, since it is more likely that the positrons will be trapped in the surface state of the sample. Furthermore, the secondary electron background in the spectra ends up at lower energies of 20 eV and enables the observation of low energy Auger transition. For PAES measurements, the re-moderated positron beam with an energy of approximately 20 eV was used. A positron intensity of $3{\cdot}10^7\,e^+/s$ was measured on the sample using a

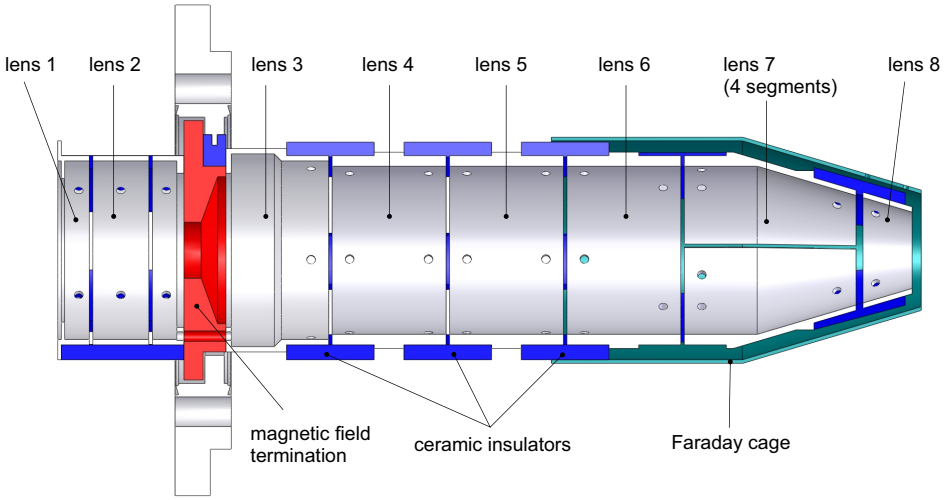

Figure 4.3: Electrostatic lens system to focus the positron beam to the sample. The positron beam coming from the left is extracted from the magnetic guiding field outside the chamber and guided electrostatically to the sample. The magnetic field termination is shown in red. Lens 7 is a four-segmented lens to deflect the beam. A Faraday cage prevents an influence of the lens potentials on electrons outside the lens system.

W-shielded NaI(Tl) scintillation detector, analyzing the 511 keV annihilation radiation of the positrons on the sample.

The shape of the positron beam is characterized by a micro channel plate (MCP) in combination with a phosphor screen used as beam monitor. It can be moved to the sample position and characterizes the beam on site. A mirror below the phosphor screen allows a CCD camera to image the phosphor screen. From this image the size of the positron beam on the sample can be estimated. Figure 4.4 shows the image from the CCD camera of the 20 eV positron beam and a line profile of the intensity distribution. The beam profile can be well described by a Gaussian shape with a diameter of 5.9 mm (FWHM).

For conventional Auger electron and X-ray induced photoelectron spectroscopy, an electron gun and a X-ray source are installed. The X-ray source is equipped with a twin anode made of Al with an energy of 1486.6 eV and Mg with 1256.6 eV. The energy of the electrons is analyzed with a hemispherical analyzer (Specs Phoibos 150) with a mean radius of 150 mm and a CCD readout. Since the energy analyzer is the key component to record PAES spectra, it is described in detail in Section 4.4.

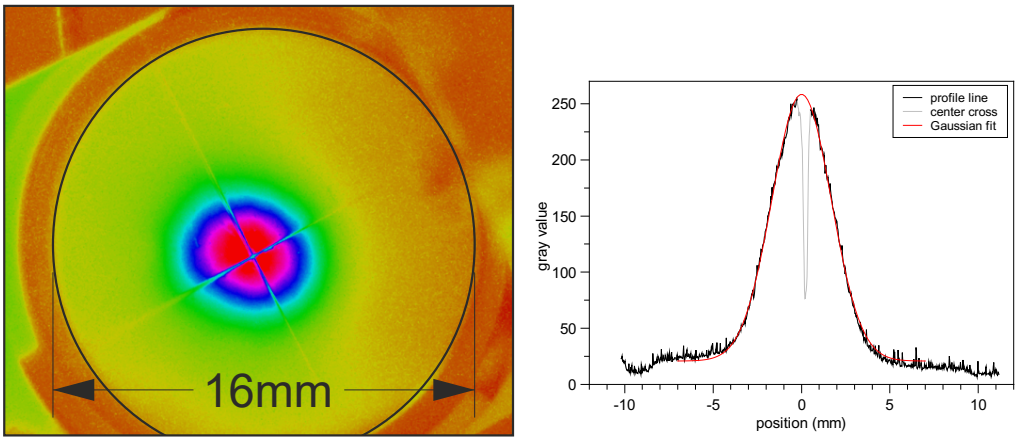

(a) (b)

Figure 4.4: a) Pseudocolor image of the spot of the 20 eV re-moderated positron beam on the MCP beam monitor at the sample position. The CCD camera images a mirror with a center cross, marking the sample position. The phosphor screen has a diameter of 16 mm. b) The Gaussian fit of the beam profile has a FWHM of less than 6 mm.

The energy analyzer is designed bipolar, so the energy distribution of electrons as well as positrons or ions can be analyzed. To avoid the influence of external magnetic fields, the chamber as well as the analyzer are μ-metal shielded. All components of the sample holder insight the chamber are made of non-magnetic materials.

The samples are precisely positioned in front of the analyzer with a rotateable xyz-manipulator, which can be cooled down using liquid nitrogen to 90 K and heated up 1300 K by electron bombardment from an Y-coated W filament installed below the sample, see Figure 4.5a. This allows in-situ temperature dependent analysis. For PAES measurements the temperature is limited to approximately 550 °C because of a dominant electron background at higher temperatures. The sample holders are fixed with three clamps in the sample stage for a best possible thermal connection. There are two different types of holding clamps. The more spring-like design marked by ③ in Figure 4.5a allows an easier handling of the samples than the ones of type ①, but become loose early. For single crystals and foils, specially designed sample holders out of Ti are available, fitting to all other sample stages in the spectrometer. Polycrystalline foils are wrapped around the sample holder and fixed with screws. Single crystals with a diameter of 10 mm can be placed into a matching

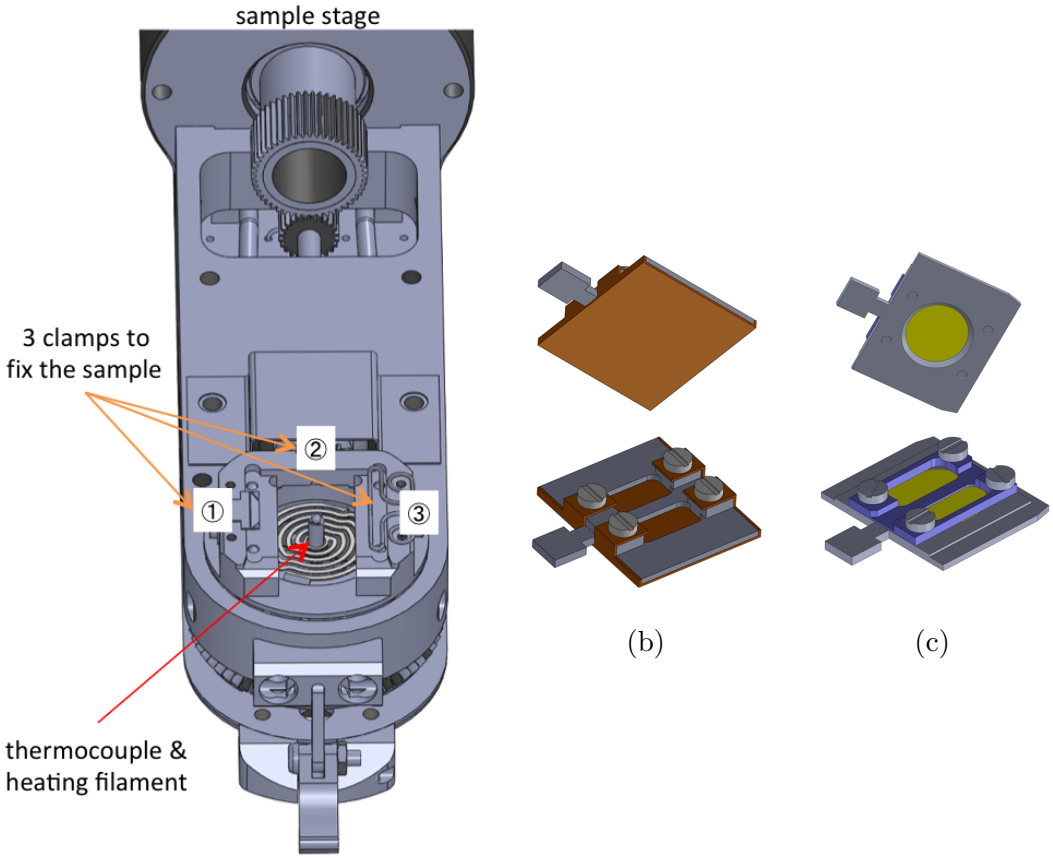

Figure 4.5: a) Sample stage in the Auger chamber for in-situ temperature dependent measurements between 90 K and 1300 K. On the right, the sample holders for (b) foils and (c) single crystals are shown (top side on top, backside below). Typical sample sizes are in the range 10 mm in diameter for single crystals.

recess fixed with a cover and screws. Both types of sample holders are shown in Figure 4.5 b and c. Recesses in the sample holders allow direct heating of the sample material. For temperature control, a thermocouple is mounted in the center of the heating filament, which can be moved with a lever towards the sample for optimal thermal contact. To avoid damaging of thin or brittle samples, the thermocouple is pressed against a Ti bridge on the rear side of sample holder with a thickness of only 0.2 mm. The thermocouple is isolated with a sapphire plate to allow biasing of the sample up to 3 kV.

For residual gas analysis, the chamber is equipped with a quadrupole mass spectrometer. Recently a new Ar-ion gun was installed in the Auger chamber to record sputter profiles with PAES is-situ.

The ultra high vacuum in all chambers is realized by a prevacuum system followed by turbo molecular pumps. In addition an ion getter pump (IGP) is installed in the STM chamber, to sorb effectively hydrogen as well as other light elements. The Auger chamber is equipped with a second turbo molecular pump dedicated for the large volume of the energy analyzer. To avoid the presence of magnetic fields in this chamber, a non evaporable getter (NEG) pump is installed, which has a pumping speed of 400 l/s for H_2. The base pressure of the Auger chamber is about $5 \cdot 10^{-10}$ mbar measured with the mass spectrometer. The residual gas mainly consists of hydrogen and H_2O. Its partial pressure is lower by a factor of three than the one of hydrogen. The water in the chamber which is mainly adsorbed at the walls of the chamber and other installed components, can be partially removed by backing the chamber. At room temperature pumping of adsorbed water is inefficient due to the high vapour pressure. At temperatures above 100 °C the water slowly desorbs from the surface and is thus pumped away. Due to some temperature sensitive components the bakeout temperature is limited to 130 °C. Typical bakeout times are 48 to 72 hours.

4.2.4 Positron elevator

For PAES it is advantageous to set the positron energy to the lowest possible value to suppress secondary electrons and enhance the surface sensitivity. But the bipolar design of the analyzer allows studies of the positron work functions as well by analyzing the energy of re-emitted positrons. To investigate the positron work function of a sample, the positrons need to thermalize completely in the bulk of the sample. Within their diffusion length of about 100 nm, some positrons can reach the surface and interact with the surface potential. Depending on the element and the crystallographic orientation, the positron work function can be negative, and positrons are emitted from the sample with a specific energy. This process is used for moderation. To investigate new materials as positron moderators, the energy distribution of the positrons needs to be measured. The implantation depth of positrons can be calculated from the Makhovian profiles [13]. Usually, an implantation energy of few keV is necessary, to fully thermalize a significant fraction of the positrons in the

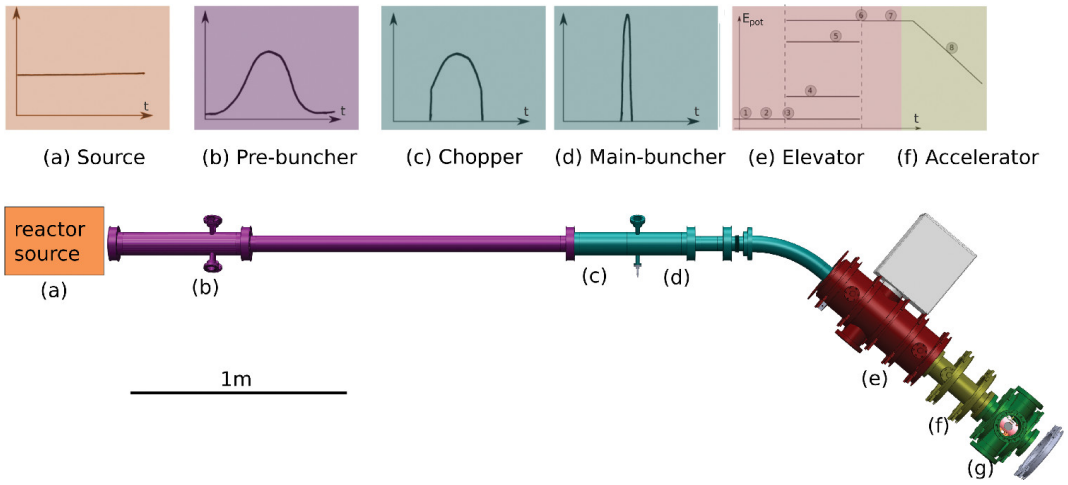

Figure 4.6: Setup of the positron elevator installed in the positron beam line at the Surface Spectrometer. From [67].

bulk of which some are able to reach the surface potential within their diffusion length.

In the present setup, the positron source as well as the sample and the detector are close to ground potential. However, an implantation energy of some keV is necessary. This increase of the positron energy is realized with the so called 'positron elevator', which is a device for particle acceleration based on elevation of the potential energy of beam pulses. The setup, shown in Figure 4.6 consists of a bunching and chopper unit (Figure 4.6 b-d) to create a pulsed beam. The pulses pass a system of three electrodes in a way, that the potential of the second electrode is increased while the positrons are passing through. The setup is able to convert the contentious 20 eV to a pulsed positron beam with a kinetic energy of up to 3.5 keV at ground potential, enabling depth dependent positron re-emission measurements. A detailed description of the apparatus can be found in reference [67].

First measurements on the work function of Ni showed excellent agreement of the experimentally determined result with literature values. Furthermore, experimental evidence of the positive work function of polycrystalline Pd was provided as predicted by theoretical calculations [68]. The energy of the positron beam was increased stepwise from 22 eV to 2.5 keV and the re-emitted positrons from Pd were measured, see Figure 4.7. The energy analyzer can't detect particles with an energy of less than approximately 7 eV. The positron work function is in a range of only a few eV, depending on the element and

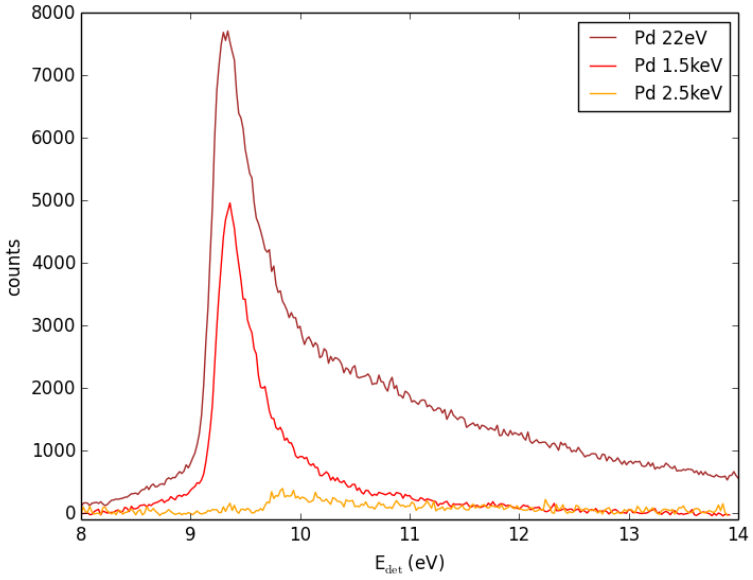

Figure 4.7: Positron reemission spectra of polycrystalline Pd. The energy of the incident positron beam was increased from 22 eV to 2.5 keV. The disappearance of the reemitted positrons at a beam energy of 2.5 keV indicates a positive positron work function of Pd. The sample was biased to +14 V. From [67].

orientation, therefore the sample has to be biased to +14 V. The Pd curve recorded with an implantation energy of 22 eV shows a distinctive peak, which suggests the emission of moderated positrons with a negative positron work function for Pd. However, the depth dependent measurement enabled by the positron energy elevator does not allow this presumption. The disappearance of the re-emitted positrons at a beam energy of 2.5 keV indicates a positive positron work function. At this energy the majority of positrons has thermalized and can't escape from the material any more, except when the positron work function is negative. The spectra at implantation energies of 22 eV and 1.5 keV are dominated by the emission of epithermal positrons since it vanishes at higher implantation depths.

4.3 Scanning tunneling microscopy

In 1981, Gerd Binnig and Heinrich Rohrer developed the first scanning tunneling microscope (STM) [69] to image the topography and atoms positions of surface.

Two years later they were able to map directly the 7×7-reconstruction[1] of the Si(111) surface with atomic resolution, which is one of the most complex surface reconstructions [70]. For their discoveries they received the Nobel Prize for Physics in 1986.

STM measurements are based on the concept of quantum tunneling: an atomically sharp conductive tip is approached to a few Angstroms to a conductive sample so that electrons are able to tunnel between the sample surface and the tip when applying a potential difference. A tunneling current of a few pico to nanoampere can be measured. The tip is moved over the sample line by line to image the electron density distribution of the sample surface, which is related to the atom's positions.

Positrons are very sensitive to local changes in the electron density distribution, as they can effect the surface positron potential described in Section 2.2. Local changes in the electron density distribution may result from step edges, adsorbates or surface atoms of different elements. Therefore, STM images provide important information on the attractiveness of surface sites for positrons and is thus a highly valuable complementary measurement technique.

The electron wave function inside the tunneling barrier can be described by the following equation:

$$\Psi(z) = \mathrm{e}^{\pm\kappa z} \quad \text{with } \kappa^2 = \frac{2m\,(V_\mathrm{B} - E)}{\hbar^2} \tag{4.5}$$

Ψ(z) denotes the wave function, m the electron mass, V_B is the potential over the barrier and E is the energy of the state. The wave function between tip and sample is shown in Figure 4.8.

The intensity of the tunnel current is exponentially related to the width d of the barrier:

$$I \propto \mathrm{e}^{-2\kappa d} \tag{4.6}$$

Due to the exponential relationship between the tunnel current and the distance of the tip to the surface, even the smallest differences in height such as step edges and individual atoms can be made visible by their effects on

[1] A reconstruction denotes an arrangement of atoms on the surface which is different from that in the volume of the crystal as a consequence of the reduction of the free energy.

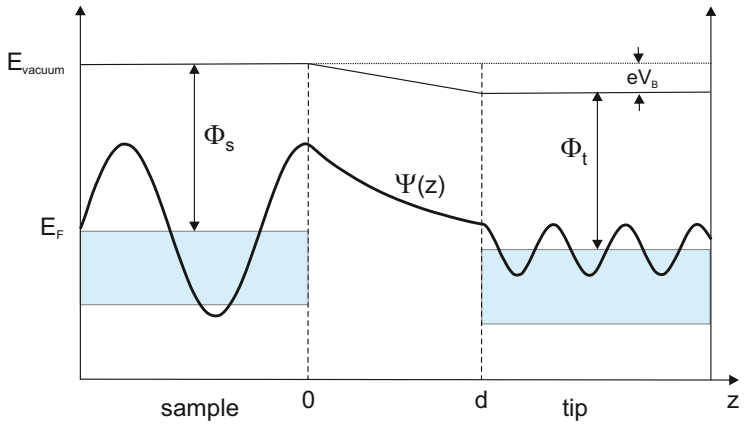

Figure 4.8: Tunneling of electrons between sample and tip illustrated by the wave function. Φ_t and Φ_s indicate the work function of the tip and sample, respectively. V_B denotes the bias voltage between tip and sample.

the tunnel current. As a rule, the strength of the tunnel current drops by an order of magnitude as the distance between the sample and the tip is increased by 1 Å [71]. Correspondingly, there should be no deviations in the distance between the tip and the sample which are attributable to the instrument in order not to falsify the measurement.

A closer look at the tunneling process reveals that not only the distance between sample and tip influences the tunnel current, but also their shape and the electronic structure. An exact description of the tunneling process considering all these influences is extremely difficult therefore, the model of John Bardeen [72] will be introduced. In this description, the following assumptions are made: It is assumed that sample and tip can be described independently by solving the stationary Schrödinger equation. The transition matrix element, which describes the electron transfer, is given by the overlap of the wave functions of tip and sample.

The condition for the electron transfer is given by Fermi's golden rule and states that only elastic tunneling, i.e. tunneling without loss of energy, is possible between the electrodes with the transition rate $\lambda_{\mathrm{i}\to\mathrm{f}}$:

$$\lambda_{\mathrm{i}\to\mathrm{f}} = \frac{2\pi}{\hbar}\rho(E_{\mathrm{f}})\,|M_{\mathrm{fi}}|^2 \tag{4.7}$$

where $\rho(E_\mathrm{f})$ is the state density of the final state, and M_fi is the matrix transition element. With these assumptions, the tunnel current in first-order perturbation theory can be described as follows [71]:

$$I = \frac{2\pi e}{\hbar} \sum_{\mu,\nu} \{ \underbrace{f(E_\mu)[1 - f(E_\nu)]}_{\text{tunneling } \mu \to \nu} - \underbrace{f(E_\nu)[1 - f(E_\mu)]}_{\text{tuneling } \nu \to \mu} \} \left| M_{\mu,\nu} \right|^2 \delta(E_\nu + V_\mathrm{B} - E_\mu) \tag{4.8}$$

In this case, all the electron states of the electrodes are summed, whereby only a contribution by elastic tunneling takes place due to the delta function. The term in the brace describes the tunnel current between the sample and the tip in both directions, since the occupation of the states with electrons in the sample and tip follows the Fermi distribution. According to the model of Bardeen [72], the matrix transition element can be written as follows:

$$M_{\mu,\nu} = \frac{\hbar^2}{2m} \int \mathrm{d}\mathbf{S} \cdot (\Psi_\mu^* \nabla \Psi_\nu - \Psi_\nu \nabla \Psi_\mu^*) \tag{4.9}$$

This is done by integrating an area orthogonal to z that lies completely within the barrier. Neglecting the variation of the potential in the integration region, the wave function can be written as:

$$\Psi(\mathbf{x}, z) = \int d\mathbf{q} a_\mathbf{q} \mathrm{e}^{-\kappa_\mathrm{q} z} \mathrm{e}^{i\mathbf{q}\cdot\mathbf{x}} \tag{4.10}$$

where $\mathbf{q}$ is the reciprocal lattice vector and $\mathbf{x}$ and z is the lateral and vertical position, respectively. κ_q^2 is given by:

$$\kappa_q^2 = \kappa^2 + |\mathbf{q}|^2 \tag{4.11}$$

with κ defined in Equation 4.5.

In STM measurements, therefore, several influences on the tunnel current are always displayed. One part is caused by the electron density distribution and hence the topography of the sample and another by the electronic structure of the sample and tip. The following section shows how one can make use of this fact with the aid of different operation modes of the STM.

4.3.1 Scanning modes of the STM

Constant hight mode In this measurement mode, the height of the tip above the sample is set to a initially defined, constant value. The tip thus moves constantly in a plane above the sample. The variation of the tunnel current is measured and presented as a height profile. This mode allows a very fast sampling of the sample with high image rates, so that dynamic processes can also be imaged. However, the surface of the sample should not be too rough, since elevations of 5-10 Å would lead to a collision of the sample and the tip.

Constant current mode In this mode, unlike the constant height mode, the tunnel current is always monitored and kept constant by a feedback loop. The tip thus follows the sample topography. This allows an atomic resolution of the sample surface, but at a lower scanning speed due to the feedback system.

Spectroscopy scans Spectroscopy scans offer the possibility to determine further physical properties such as the local density of states or the local work function of the sample surface. The measurement of the local barrier hight is done by measuring the variation of the tunnel current with simultaneous variation of the height above the sample. The tunnel current decreases exponentially with the distance to the sample. From equation 4.6 one obtains the relationship

$$\left(\frac{\mathrm{d}\ln I}{\mathrm{d}z}\right)^2 \propto V_\mathrm{B} - E \approx \Phi \tag{4.12}$$

In a simplified view, the vacuum level is constant and remains constant over the distance between the sample and the tip. Furthermore, only one tunneling direction is allowed, which would correspond to the Fermi distribution at T=0. In the tunneling process, states near the Fermi energy are involved [71], so that for these states the work function of the sample corresponds to the sample. The local barrier height spectroscopy provides an information about the spatial distribution of the microscopic electron work function of the surface, determining the positron surface potential.

Assuming a constant distance between tip and sample and constant density of states of the tip, the tunnel current can be qualitatively written as [73]

$$I(V) \propto \int_{E_\mathrm{F}}^{E_\mathrm{F}+V} \rho(E)T(E,V)dE \Rightarrow \frac{dI}{dV} \propto \mathrm{LDOS} \tag{4.13}$$

ρ is the local density of state (LDOS) of the sample surface and T(E,V) is the transmission coefficient through the barrier. The determination of the LDOS can also help to distinguish chemical bounding of the surface atoms, as it is also possible with XPS, but its results are averaged over large surface areas.

In principle, however, it must be noted that the intensity of the tunnel current in the different measuring modes is not determined exclusively by the topography of the sample, but also by the state density, the work function, as well as the voltage applied to the sample and its sign, factors, which are also crucial for positrons.

4.3.2 STM measurements

To demonstrate the atomic resolution of STM, reference measurements were performed on Si(111). Figure 4.9 shows the empty and occupied states of Si(111), including the famous 7×7 surface reconstruction with atomic resolution.

As described in the previous section, the tunneling current is in the order of some hundred pico to few nanoampere and highly sensitive to external disturbance. When the spectrometer was in full operation for the first time, several external influencing factors on the STM were found, which considerably interfere with the tunnel current. Figure 4.10 summarizes the effects to the STM of some components of the spectrometer. During tip approach to the sample, the monitor signal of the tunneling current appeared to be noisy. A Fourier analysis of the tunneling current can help to identify the disturbances, since it shows the intensity of the tunneling current frequency-resolved over time. This analysis is done when the tip is not in tunneling contact with the sample. Since no sample interaction takes place at this position, the tunneling current can only be influenced by external fields. Thus, an almost horizontal line with white noise at a low amplitude is expected. The spectra show peaks with variable width over the hole frequency range. Some causes of the disturbances could be found. Especially the ion getter pump (IGP) mounted in the STM

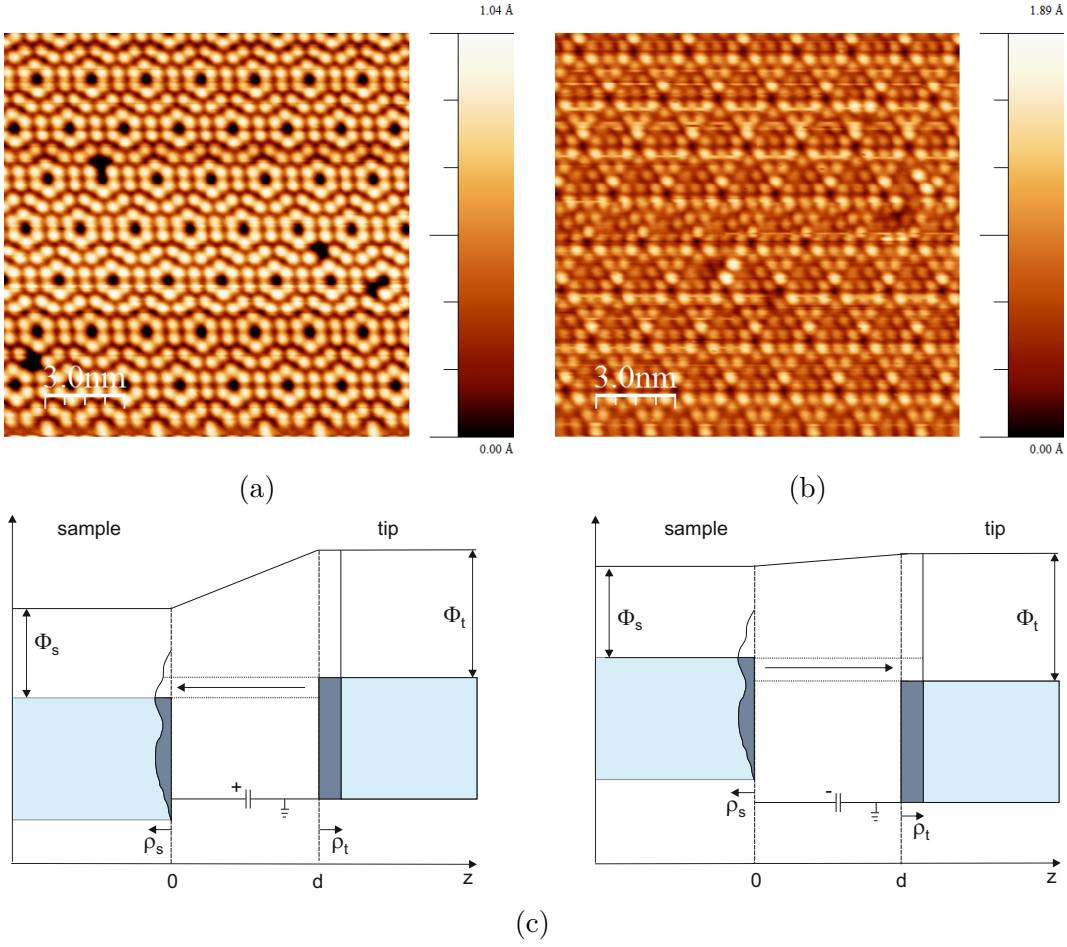

Figure 4.9: STM image with atomic resolution of the (a) empty and (b) occupied states of Si(111) showing the famous 7×7 reconstruction.
(c) Scheme of the tunneling process of electrons tunneling from the tip to the empty states of the sample (left) and from the occupied states of the sample to the tip (right).

chamber has to be mentioned. The ion getter pump of the Auger analysis chamber was replaced by a non evaporable getter pump meanwhile. The power supply of the energy analyzer was found to disturb the tunneling current, too. However, a large number of other disturbing influences remain, which could not be assigned to components of the spectrometer.

When the tip is in tunneling contact with the sample, the stability of the piezo element controlling the vertical position of the tip is crucial for STM imaging. Its movement can be analyzed, when the lateral position of the tip is fixed. In this position, the regulation of the piezo element to maintain the setpoint value of the tunneling current can be monitored. For the present STM, usually a value of 1 pm is not exceeded in a frequency range of more than 80 Hz. Below 80 Hz, the shape can be described by an exponential decay without any sparks. A periodicity of peaks can indicate a loose sample or sample holder, which vibrates under the influence of the tip. To exclude this possibility, the measurement was repeated with different sample types, such as single crystals and foils, which, however, led to the same result.

In order to rule out mass loops, the mass connections between the STM and the UHV chamber as well as the connection between the STM controllers and the common ground were reinforced and the power supplies were installed separately from other controllers of the spectrometer. A separate PC was used with galvanic isolation to the STM to avoid mass loops. A reduction of the intensity was achieved by using a 50 Ω terminating resistor at the tunneling current monitor signal. At irregular intervals, a discontinuation of the disturbances of 1-2 seconds was observed, without noticeable influence.

To evaluate the result, STM measurements were performed on polycrystalline Cu. The image shows an alignment in rows of the atoms as well as some adsorbates, appearing in bright color, cf Figure 4.11 a. However, the image is disturbed by an overlay of high frequent artifacts. In a Fourier analysis of the image at least five side peaks were identified, leading to periodic noise in the image. However, a suppression of the artifacts leads to a bluring of the image.

In later measurements, a permanent saturation of the tunnel current was observed after approaching the tip to tunnel contact, although the voltage of the piezo element was reduced again stepwise, which should move the tip downwards. This can be an indication of a defect in the piezo, since it no longer

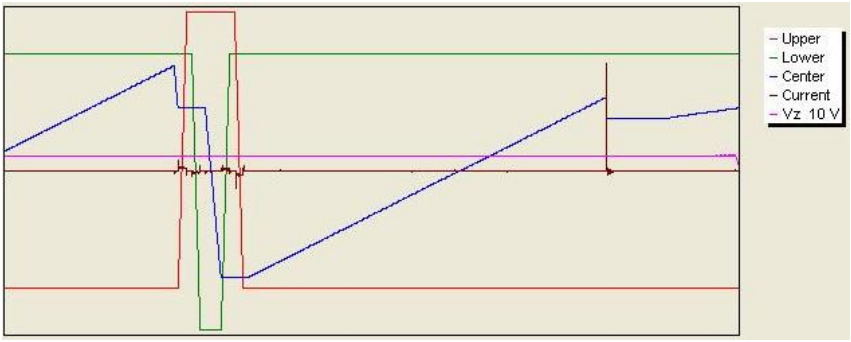

(a)

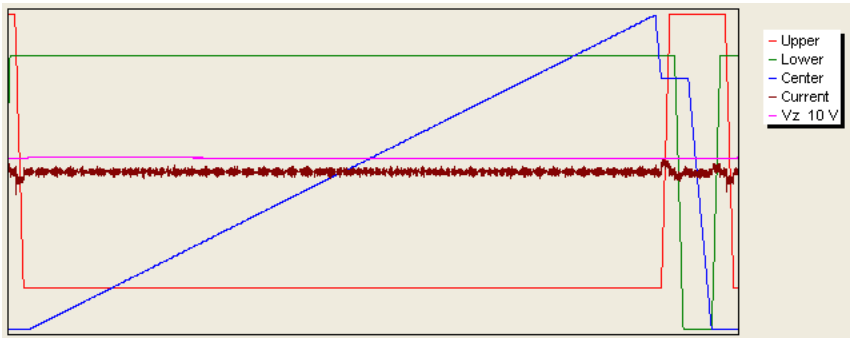

(b)

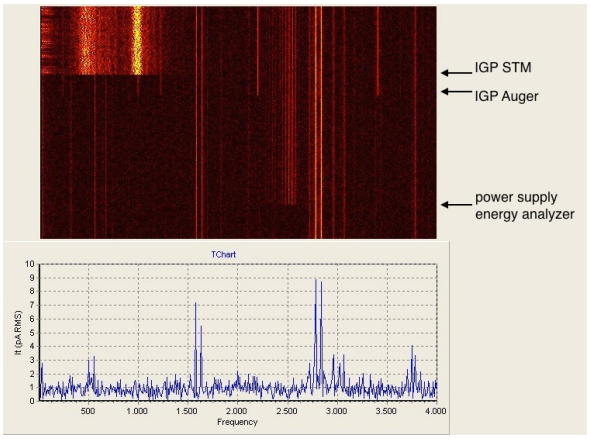

(c)

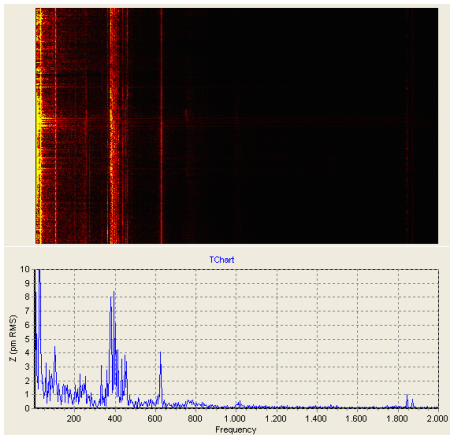

(d)

Figure 4.10: a) The brown center line shows the monitor signal of the tunneling current during the tip approach. The discrete peak indicates the approach to tunneling contact between the tip and the sample. The other lines indicate piezo voltages while moving the tip. (b) Various high-frequency interference disturb the usually smooth signal of the tunneling current. c) The Fourier analysis of the tunneling current during approach provides information about the influence of some components belonging to the spectrometer: switching off the ion getter pumps (IPG) of the STM and the Auger chamber as well as the power supply of the energy analyzer leads to the vanishing of some frequencies. However, some peaks sketched in the diagram below remain in the spectrum. c) Fourier analysis of the vertical movement of the piezo element controlling the tip's hight, when the tip is in tunneling contact with the sample. The lateral position is fixed for this measurement (see text for details).

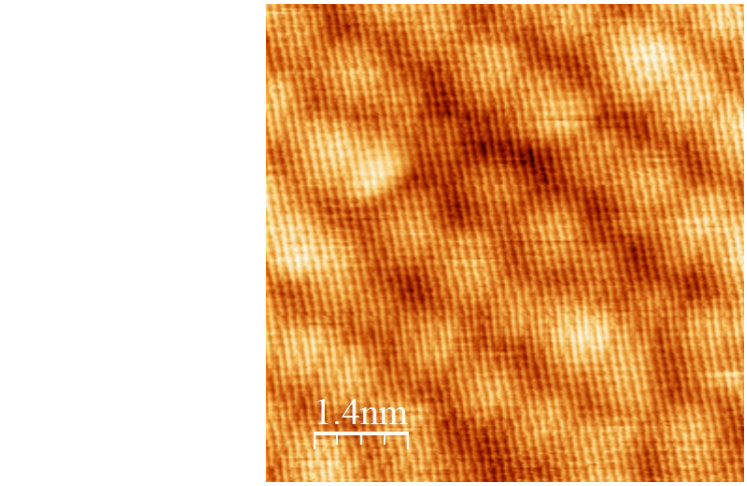

(a)

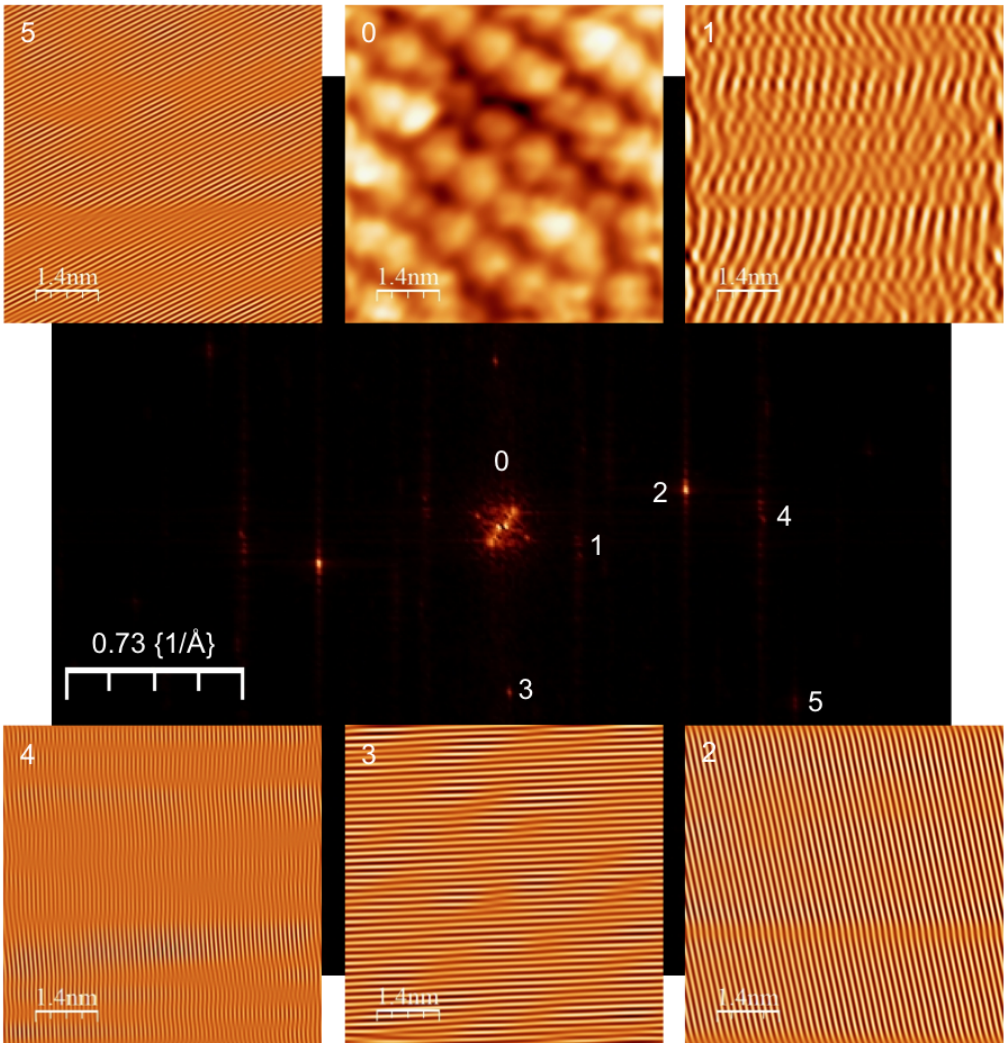

(b)

Figure 4.11: a) STM image of a polycrystalline Cu surface. The atoms aligned in rows are resolvable, but disturbed by an overlay of artifacts. b) The FFT analysis of the STM image shows several side peaks (1-5), which lead to the different artifacts shown in the surrounding images. Elimination of the side peaks leads to a blurred image (0).

moves uniformly. Therefore, a systematic comparison of the PAES studies shown in the Chapters 6 and 7 with complementary STM analysis at the surface spectrometer was not possible.

4.4 The electron energy analyzer

The energy analyzer is one of the key components for electron spectroscopy. An hemisphererical analyzer mainly consists of three components: a lens system at the entrance, two concentric hemispherical electrodes and an electron detector, as shown in Figure 4.12. The grid-free lens system collects electrons emitted from a certain area and acceptance solid angle of the sample, guides them into the analyzer and accelerates or decelerates them from the nominal particle kinetic energy E_{kin} to the selected pass energy. For a better energy resolution, slits of various sizes centered on the mean radius of the analyzer can limit the entrance angle. Subsequently, the electrons pass the hemispheres, which act as an energy filter due to the applied potential for energy analysis. The mean radius of the analyzer is R_0=150 mm, while the hemispheres have radii of R_i=0.75·R_0 and R_o=1.25·R_0. Only electrons with kinetic energies in a certain energy interval are able to pass through the full deflection angle of the analyzer without hitting one of the hemispheres. Since the analyzer is bipolar, which means that the energy distribution of electrons, as well as positrons or ions can be investigated.

The pass energy E_p is given by

$$E_p = -q \cdot k \cdot \Delta V \tag{4.14}$$

with the charge q of the particles, the potential difference ΔV between the hemispheres and a detector specific constant k. Particles with this energy describe the central trajectory through the hemispheres. Electrons with an energy lower than the pass energy go through the hemispheres on a smaller radius, those with a higher energy run on a larger one (shown in Figure 4.12 in red and blue, respectively.). At the exit of the hemispheres the electrons pass a second slit system and hit a Chevron micro channel plate with a phosphor screen behind. The lateral intensity distribution on the phosphor screen reflects

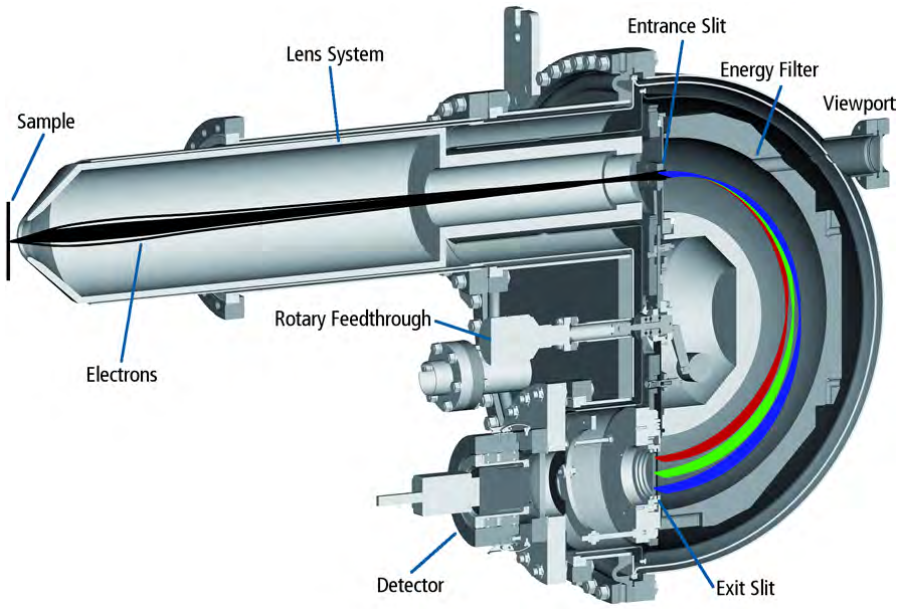

Figure 4.12: Sketch of the Phoibos 150 hemispheric energy analyzer [74]. Electrons emitted from the sample surface are collected by the lens system accelerated or decelerated to the pass energy and guided into the analyzer. The hemispheres act as an energy filter. The trajectory of electrons with the pass energy is shown in green. Electrons with a lower energy are shown in red, those with a higher energy in blue. Entrance and exit slit are used to optimize the energy resolution of the analyzer. After passing the exit slit, the electrons hit a Chevron micro channel plate with phosphor screen. A cooled CCD camera images the screen to map the energy and angular distribution.

the energy and angular distribution of the electrons when leaving the sample. The phosphor screen is read out using a CCD camera, which is cooled to -11 °C to reduce the thermal noise. In contrast to a readout systems with channeltrons the CCD readout allows angle resolved measurements. The image from the CCD camera is analyzed by a software provided by the manufacturer of the analyzer, which contains all analyzer specific settings and calibration curves. To record an energy spectrum, the software controls the analyzer that the potentials are set in such a way that only electrons pass through the analyzer in a certain energy range and are imaged onto the micro channel plate. Step by step, the potentials are then changed until the entire previously set energy interval has been mapped.

4.4.1 Energy resolution

For a fixed electrical field gradient between the hemispheres, only particles with kinetic energies close to the pass energy are able to travel through the analyzer. Electrons with the pass energy E_p reach the exit slit at the nominal radial position R_0. The energy resolution ΔE of the analyzer is given by [74]

$$\Delta E = E_p \left(\frac{W}{2R_0} + \frac{\alpha^2}{4} \right) \tag{4.15}$$

where $W = \frac{1}{2} \cdot (W_1 + W_2)$ is the average of the width of the electron beam at the entrance and exit slit in the dispersion direction and α is the average angular width of the electron distribution.

In addition, the acceptance solid angle Ω of electrons emitted from the sample surface and the accepted sample area A are also included in the intensity of the measurement signal. These parameters are defined by the selection of the input aperture and the lens mode. The measured intensity is given by [74]

$$I \sim \Delta E \cdot \Omega \cdot A \sim \frac{E_p^2}{E_{kin}} \tag{4.16}$$

4.4.2 Modes of operation

For the recording of spectra, two different measurement modes can be selected, which differ in transmission probability and energy resolution and are shown in the following.

Fixed Analyzer Transmission In the **F**ixed **A**nalyzer **T**ransmission mode (FAT) all electrons are accelerated or decelerated to a pass energy, which is constant for the entire kinetic energy range of the spectrum. Since the pass energy is constant, the absolute energy resolution given in Equation 4.15 is constant in the spectrum. Consequently, if the kinetic energy is the same, a low pass energy improves the energy resolution of the analyzer. Higher pass energies, on the other hand, offer a much higher transmission due to the relationship $I \sim E_p^2$ of Equation 4.16.

For a fixed pass energy the intensity is given by $I \sim \frac{1}{E_{kin}}$. Therefore, in this mode, the secondary electron background appears to be overrepresented by elastically scattered electrons at low kinetic energies.

The relationship of pass energy, transmission and energy resolution is illustrated in Figure 4.13. The Pt 4f double photopeak with an energy separation of only 3.3 eV between the $4f_{5/2}$ and $4f_{7/2}$ energy level is used for demonstration. The spectra were recorded in the FAT mode with pass energies starting from 10 eV up to 200 eV. At a pass energy of more than 125 eV the two peaks merge into a plateau and are no longer resolvable at even higher pass energies, whereas the transmission is significantly higher. The loss of energy resolution is visible in the spectra recorded with 25 eV and 200 eV, which were normalized to one to get rid of the different transmissions. At even lower pass energies of about 10 eV, the signal to background ratio becomes worse and peaks are hardly separable from the background. To obtain good statistics it becomes necessary to sum up several spectra, leading to longer measurement times.

Fixed Retarding Ratio The second analyzer mode, called **F**ixed **R**etarding **R**atio mode (FRR) keeps the ratio R constant between the pass energy and the kinetic energy. Φ defines the analyzer electron work function.

$$R = \frac{E_{\mathrm{kin}} - \Phi}{E_{\mathrm{p}}} \tag{4.17}$$

This means that the pass energy is continually adjusted to the kinetic energy during the measurement according to the selected ratio. Since the pass energy raises with the kinetic energy the potential difference between the hemispheres therefore has to increase. According to Equation 4.15, the absolute energy resolution decreases with increasing kinetic energy, while the relative energy resolution $\frac{\Delta E}{E}$ is constant over the entire energy range.

For the intensity, the following is obtained in this mode: $I \sim E_{\mathrm{kin}}$. The secondary electron background is thus shown less intensively. Auger electron spectroscopy measurements are therefore usually taken in this mode.

Figure 4.14 shows the XAES spectra of the low energy Pt Auger transitions at 43 eV and 64 eV recorded in the FAT and FRR mode. In the FAT mode, the peaks are hardly visible independent of the pass energy due to the dominant secondary electron background. The FRR mode on the other hand effectively suppresses the transmission at lower energies so that the Auger peaks are clearly visible.

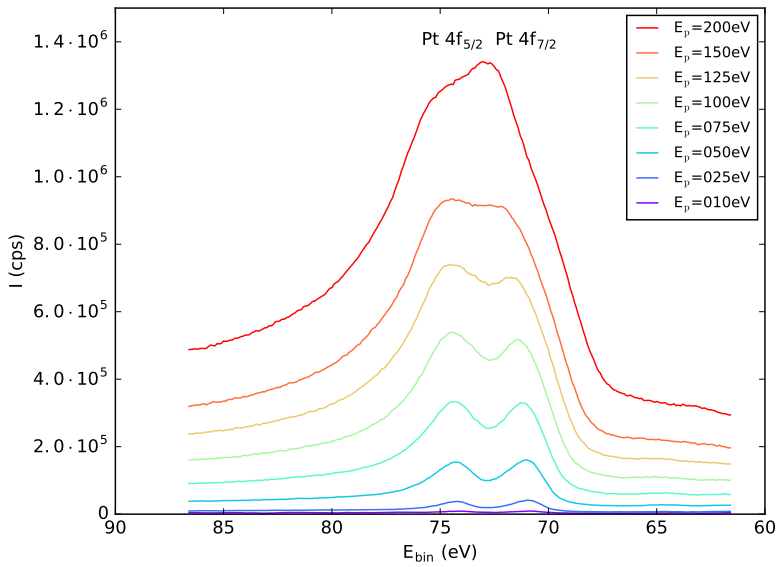

(a)

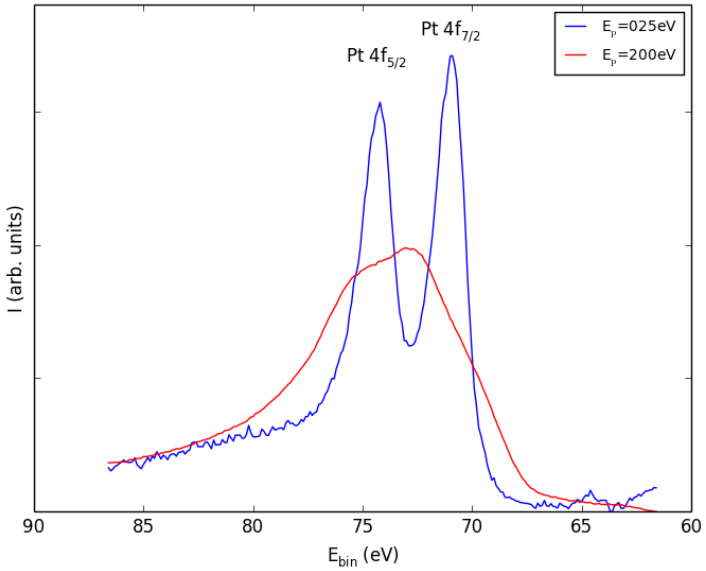

(b)

Figure 4.13: Illustration of transmission and energy resolution of the analyzer in the FAT mode. a) The spectra show the Pt 4f double photopeak recorded with pass energies between 10 eV and 200 eV showing the increasing transmission. b) The normalized spectra recorded with a pass energies of 25 eV and 200 eV visualize the loss of energy resolution.

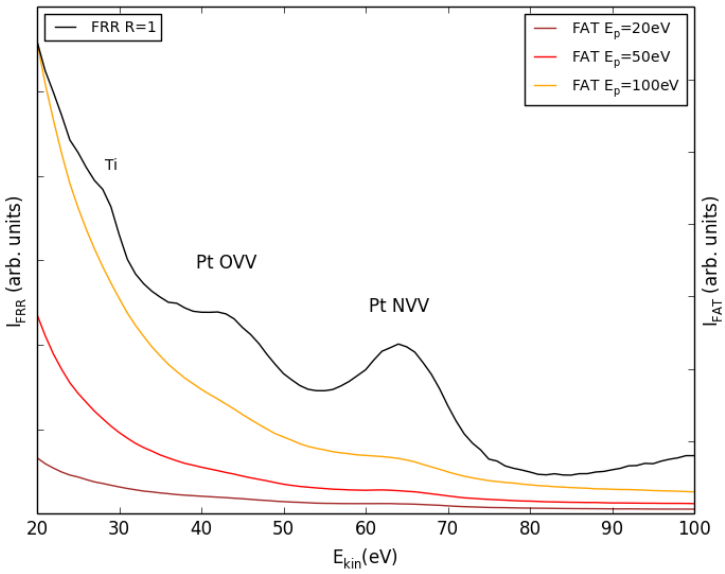

Figure 4.14: XAES spectra of the low energy Pt Auger transitions recorded in the FAT and FRR mode. The high secondary electron background dominates the FAT spectra, whereas in the FRR mode the Pt Auger transitions are clearly visible, due to the suppressed transmission at low energies. The titanium signal originates from the sample holder.

4.4.3 Measurement parameters

In order to achieve a good comparability between the results, the measurements in the following chapters were carried out with standardized parameters. For PAES the Wide Angle Mode (WAM) with an acceptance angle of ± 13° of the analyzer was used. With its large acceptance angle this mode collects as many electrons emitted from the sample as possible in the FRR mode. The retarding ratio was set to R=1. For EAES and XAES measurements the Low Angular Dispersion (LAD) mode was chosen with a reduced acceptance angle of ± 7°, and R values of 5 and 3, respectively due to the higher source intensities. The theoretical relative energy resolution $\frac{\Delta E}{E}$ in the chosen modes with the respective retarding ratios is $\frac{\Delta E}{E} \leq 2\,\%$ for PAES, $\frac{\Delta E}{E} \leq 0.7\,\%$ for XAES, and $\frac{\Delta E}{E} \leq 0.4\,\%$ for EAES. The XPS spectra were recorded using Fixed Analyzer Transmission (FAT) with the Large Area (LA) mode for non-monochromatic X-ray sources. For overview spectra, the pass energy was set to 100 eV, which is a good compromise between energy resolution and intensity. Both is important for detecting the weak signal of contamination from the residual gas on the

surface. Typical measurement times for a PAES spectrum were 30-40 minutes for high statistics, to clearly separate e.g. the Auger transitions of Pd and Ni at 43 eV and 60 eV from each other. For EAES and XAES the acquisition time was less than two minutes per spectrum.

Due to the lower intensity of the positron source compared to standard X-ray or electron sources, the MCP detector voltage needs to increased from 1400 V to 1700 V leading to a higher amplification. In addition, the exposure time of the CCD camera has to be changed from 0.1 s to 2 s to achieve a good signal to noise ratio. Therefore, it is important to cool the CCD camera to -11 °C to reduce the thermal noise.

Chapter 5

Data evaluation and quantification

5.1 Quantification of XPS spectra

A XPS survey spectrum of a material contains several photopeaks, which can be associated with various elements present in the outermost approximately 10 nm of a sample, as discussed in Chapter 3. The area under these peaks is related to the amount of each element. For quantification, correction terms representing the instrumental factors such as flux of the X-ray source and irradiated sample area, the solid angle of the photoelectrons accepted by the analyzer as well as the analyzer transmission function in a certain acquisition mode need to be considered.

Assuming an amorphous sample, the area $\mathrm{I}_{i,j}$ of a peak j from an element i is then given by [75]

$$I_{i,j} = C \cdot T(E_{\mathrm{kin}}) \cdot L_{i,j}(\gamma) \cdot \sigma_{i,j} \int_0^\infty n_i(z) \cdot \exp\left(\frac{-z}{\lambda(E_{\mathrm{kin}}) \cdot \cos(\Theta)}\right) \mathrm{d}z. \qquad (5.1)$$

with the instrumental constant C, the analyzer transmission function $T(E_{\mathrm{kin}})$, the angular asymmetry factor of the orbital $L_{i,j}$, the photoionization cross-section $\sigma_{i,j}$, the concentration $n_i(z)$ of an element i in the distance z below the sample surface, the inelastic mean free path $\lambda(E_{\mathrm{kin}})$ and the take-off angle Θ of the photoelectrons measured with respect to the surface normal. The angular

asymmetry factor affects the angular dependence of the photoemission from a given orbital emitted under the angle γ between the incident X-rays and the ejected photoelectrons. It is an atomic effect, which means that its magnitude is independent of the chemical environment of the atom. Tables of the angular distribution of photoelectrons can be found in [76]. The photoionization cross-section $\sigma_{i,j}$ is the probability for the creation of a photoelectron by the incident X-ray. Values can be taken from the calculations of Scofield [27] for the K_α lines of Al and Mg. The ionization cross-section of an element is given with respect to the cross-section of carbon. Therefore, this value is often called relative sensitivity factor.

The concentration X_A of an element A can be expressed by

$$X_A = \frac{I_A}{\sum_i I_i} \tag{5.2}$$

where $\sum_i I_i$ represents the photopeak intensities of all elements present in the sample's surface.

As a result of the excitation with X-rays, photoelectrons are generated and move through the solid undergoing both elastic and inelastic scattering. The latter results in a background of inelastically scattered electrons. For quantification of the spectra, these electrons need to be removed when evaluating the peak area. The easiest way to remove the background is the straight line approximation, which works well for polymers and insulators, as the intensity for kinetic energies just below the peak is close to that for energies just above due to the significant band gap [77].

If the background at the lower kinetic energy side of the peak is higher than on the other side, the area of the straight line background strongly depends on the choice of the end points. The Shirley background [79] is a simple S-shaped background whose intensity is proportional to the total intensity of the peak area above the background for all channels at higher kinetic energies up to a chosen limit. The essential feature of the Shirley algorithm is the iterative determination of a background using the areas marked A1 and A2 in Figure 5.1 to compute the background intensity $S(E)$ at energy E [78]:

$$S(E) = I_2 + \kappa \cdot \frac{A_2(E)}{A_1(E) + A_2(E)} \tag{5.3}$$

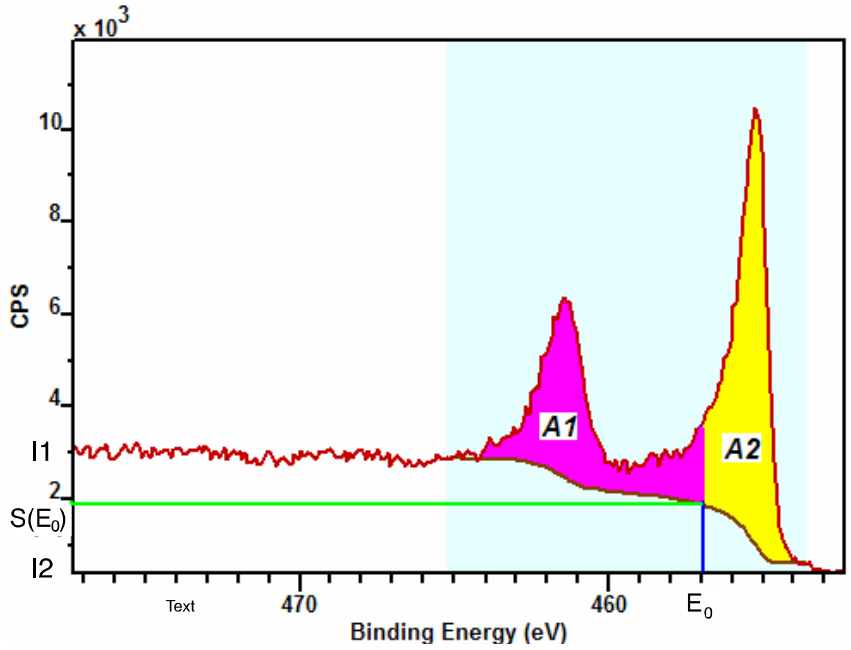

Figure 5.1: Background subtraction in XPS spectra using a Shirley background computed for a Ti 2p photopeak. From [78].

κ defines the step in the background and is typically the mean intensity before and after the peak. The integrated areas $A_1(E)$ and $A_2(E)$ for each point on the background E must initially be computed using an approximation for S(E), then refined using the background computed from the first approximation as input to improve the values computed for $A_1(E)$ and $A_2(E)$. Both, linear and Shirley background subtraction methods are found as a standard tool in commercial XPS data processing systems prior to quantification and peak fitting. An extensive review on the quantification of XPS spectra can be found in [80].

5.2 Quantification of PAES spectra

The exceptional surface sensitivity of PAES discussed in the previous chapters provides unique information of the element distribution in the surface layer. So far, there is no standard evaluation method for PAES spectra as implemented in e.g. CasaXPS for the spectra of X-ray photo electron spectroscopy. Hence, the evaluation of PAES spectra is of great importance for quantification and for interpretation of the results.

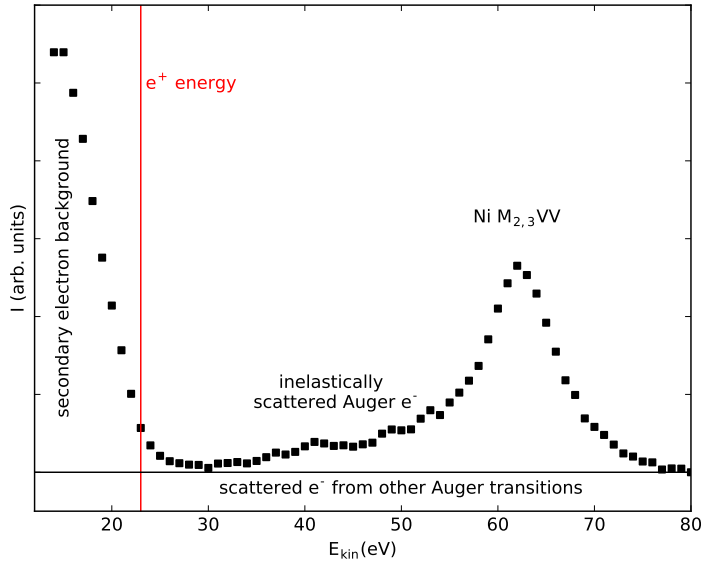

Figure 5.2: PAES survey spectrum of polycrystalline Ni showing the main contributions to a PAES spectrum: Due to the low energy of the incoming positrons of only approximately 20 eV, the Ni $M_{2,3}$VV-Auger transition is free from secondary electron background. The Auger transition itself shows a tail of inelastically scattered Auger electrons with lower energy. A very low electron background results from scattered Auger electrons from transitions at higher energies and appears as a constant contribution to the spectrum.

Before going into detail on the evaluation, the main features of a PAES spectrum will be explained. A typical PAES spectrum is shown in Figure 5.2. In addition to the outstanding surface sensitivity of PAES using low energy positrons of some eV, a second advantage is that the relevant Auger transitions are free from secondary electron background. Low-energy Auger transitions have an energy width (FWHM) of several eV, which results from the broad energy distribution of the valence band. Another aspect is the lifetime of the states involved in the Auger transition, which can also lead to a width in the range of eV. Besides, the Auger peak of the according transition shows a low-energy tail of inelastically scattered Auger electrons. A very low electron background originates from scattered Auger electrons from transitions at higher energies and appears as a constant contribution to the spectrum. Furthermore, a constant background level arises from the thermal noise of the MCP and the CCD camera as well as from γ radiation from surrounding experiments.

Conventional AES uses electrons or X-rays with some keV to induce the Auger process. These high energies lead to a large secondary electron background, especially in the range of the low energy Auger transitions, which are most surface sensitive in conventional AES. For this reason, usually the derivative of an AES spectrum is shown, in order to make the peaks visible, but then a quantitative analysis of the spectra is almost impossible [81]. The initialization of the Auger process using positrons overcomes all these disadvantages, since the spectra don't need to be differentiated and a quantification becomes possible.

5.2.1 Event counting

In a first approach to quantify the contribution of each element to the PAES spectra, the events in a fixed energy Region of Interest (ROI) around the Auger peak positions were summed up. Firstly, a constant background is subtracted from the spectra. It is derived from the mean count rate in an energy range, where the tail of scattered Auger electrons with higher energies is assumed to be constant. This assumption is based on the diminishing core annihilation probability of annihilation with more strongly bound electrons, leading to energetically higher Auger transitions. Each ROI was set to a width of 8 eV corresponding to the FWHM of a Gaussian fit of low-energy Auger peaks of different elements. For this purpose, PAES spectra of the pure elements were recorded and used as reference spectra for calibration. For several reasons, the Auger transitions do not appear as sharp lines in the recorded spectra. Especially, the low energy tail, which originates from inelastically scattered Auger electrons, can extend to another Auger peak with a lower energy spuriously pretending a higher intensity of this transition. For the measurements on Ni and Pd discussed in the next chapters, scattered electrons from the Pd N_1VV transition at 78 eV disturb the Ni $M_{2,3}VV$ and the Pd $N_{2,3}VV$ transitions at 61 eV and 43 eV, respectively. However, this is a rather small effect due to the low core annihilation probability for the Pd 4s electrons, so the contribution to the background is negligibly small. Noteworthy are scattered Auger electrons from the Ni $M_{2,3}VV$ transition, which lead to a significant contribution to the measured Auger electron intensity of the Pd $N_{2,3}VV$ peak. For data analysis, the amount of the scattered electrons in the respective ROIs of the lower energy peaks was determined from the reference materials and

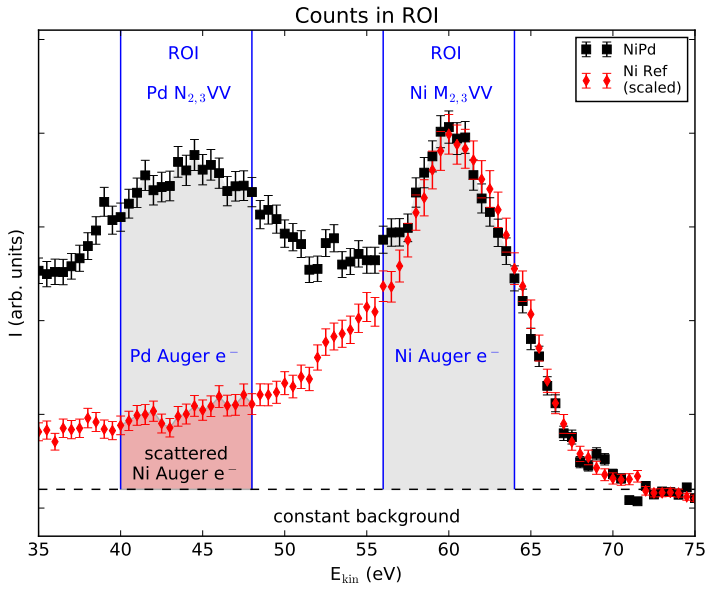

Figure 5.3: First approach for the quantification of PAES spectra: Energy intervals (ROIs) around the Auger peak positions are defined wherein the events are counted. For this, the spectra of the pure elements are necessary for calibration. The scattered Ni Auger electrons in the Pd ROI have to be taken into account. Therefore, this weighted fraction of scattered Ni Auger electrons is subtracted from events in the Pd ROI to not overestimate the Pd contribution in the spectra.

subtracted as shown for Pd in Figure 5.3. To quantify the contribution of an element to the Auger spectrum in a compound, the counted events have to be compared with those of the reference spectra of the pure elements, allowing a statement on the Auger fraction of an element in the compound spectrum.

Both, the contribution of scattered Auger electrons from other transitions and the scaling factors for the quantification to meet the reference spectra are element and compound specific parameters. For each combination of elements, the determination of these parameters has to be done anew.

5.2.2 Approximation by reference spectra

To overcome the special handling of scattered Auger electrons, a new approach to quantify the spectra was used. The recorded data M(E) of a compound is fitted by a model function F(E), which is assumed as a linear combination of

the reference spectra $S_{X,Y}(E)$ of the pure elements X and Y using independently scaled fractions α and β:

$$F(E) = \alpha \cdot S_X(E) + \beta \cdot S_Y(E) \tag{5.4}$$

The reference spectra $S_{X,Y}$ were recorded in advance with the same measurement parameters. As a figure of merit, the fit is characterized by the R value, which quantifies the difference between the recorded data and the fit function. The R value as defined in Equation 5.5 is minimized in the fitting procedure.

$$R = \sum_i (M_i - F_i)^2 \tag{5.5}$$

In the applied fitting procedure it is not a requirement that the sum of the scaling factors α and β has to be unity. This condition would presuppose that the line shape of an Auger transition is not influenced by the presence of additional elements, or by chemical bonding. For this reason, the scaling factors are varied independently.

For the fitting procedure, a constant background represented by the minimum value is subtracted from each spectrum and all spectra are normalized to one. Figure 5.4 illustrates the first steps of the iteration of a spectrum of a 0.5 ML cover layer of Ni on a Pd substrate. Initially, the measured data and the reference spectra of pure Ni and Pd are shown. Then, the algorithm starts to vary the scaling factor α for the Ni reference to minimize the difference R between data and fit. In the next step, the scaling factor β for Pd is varied to minimize R, while the scaling factor α for Ni is kept constant. After this, again the Ni fraction is varied and Pd is kept constant. Up to now, the iteration is executed 20 times, though no reduction of the R value is found any more after about ten iterations for most spectra.

The result of the minimization is shown in Figure 5.5 a. The measured data can be excellently described by a linear combination of the two reference materials over the whole energy range. By plotting the full parameter range of the scaling factors α and β, it can be shown that the result of the fitting procedure corresponds to the global minimum of the R parameter, see Figure 5.5 b. The fit algorithm was also applied to Ni on Pt, Fe on Pt and Fe on Pd. Fitted and measured spectra showed a very good agreement and the resulting

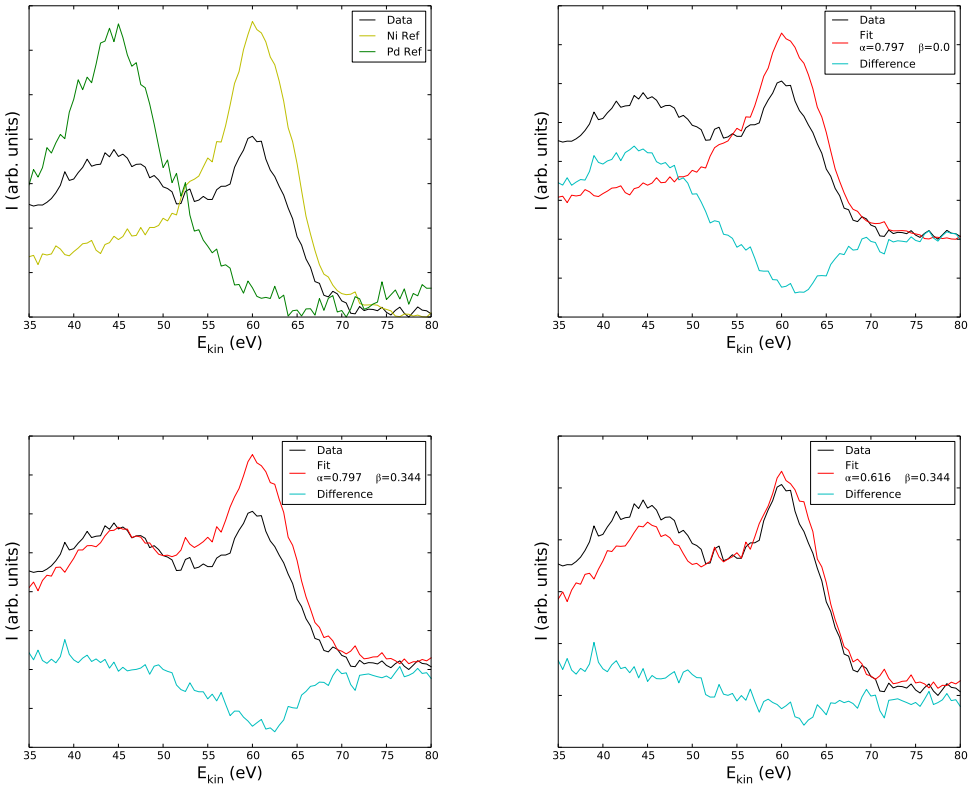

Figure 5.4: Illustration of the first steps of the minimization algorithm using the example of 0.5ML Ni on Pd. Starting from top left, the plots show the reference spectra of pure Ni (yellow) and pure Pd (green) and the measured spectrum of the compound (black). In the first iteration step, the scaling factor α of Ni is varied to minimize the difference R (cyan) between the measured spectrum and the fit (red). In the second step, the Pd scaling factor β is varied, while α is kept constant. Subsequently, Ni is varied again, while Pd is fixed. Published in [82].

fractions match with the amount of cover layers deposited on the substrate. Therefore it is well assumed that the reproduction of the measured spectrum by a linear combination of references is a reasonable description for these systems.

None of the element combinations mentioned above exhibits island growth. PAES is sensitive only to the topmost layer, and due to the three dimensional structure in case of island growth, the surface appears to have a lower coverage than the nominal value. In this case the fit might show a good agreement with the spectra, but the scaling factors differ from the amount of cover layer deposited.

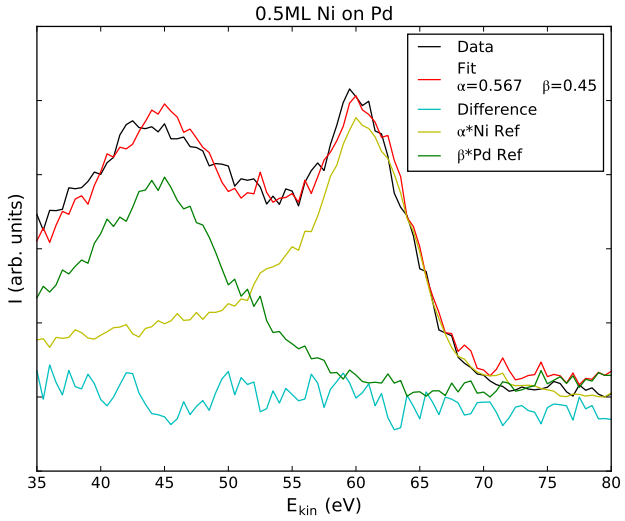

(a)

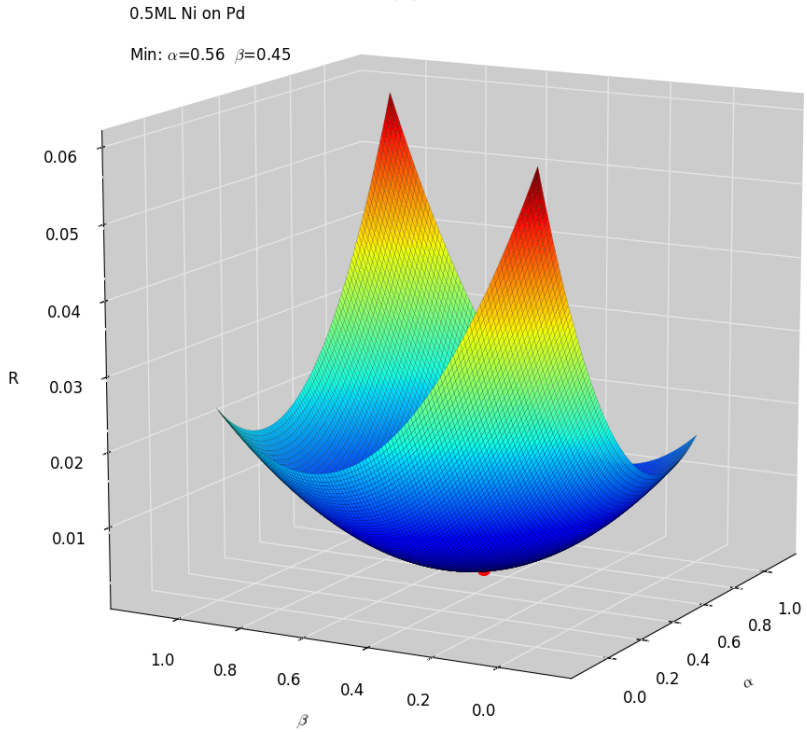

(b)

Figure 5.5: a) Result of the approximation of the measured data by reference spectra. The measured spectrum (black) is fitted (red) by independent scaling of the spectra of pure Ni (yellow) and pure Pd (green) in order to minimize the difference R (cyan) between the measured spectrum and the fit. b) By plotting the R value for all combinations of the scaling factors α and β for Ni and Pd respectively with a step size of 0.01, it can be demonstrated that the result of the new fitting procedure corresponds to the global minimum for the full parameter range. The minimum of R is indicated by the red dot. Published in [82].

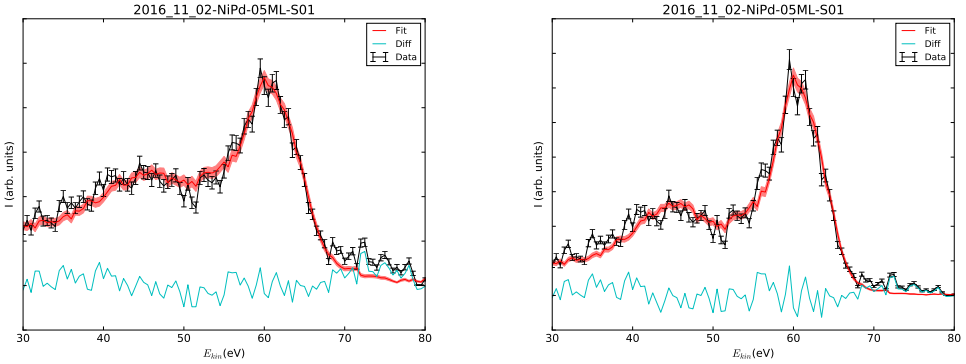

(a) Unweighted spectrum. (b) Weighted spectrum.

Figure 5.6: Effect of weighting a spectrum in the fitting procedure on the example of a Ni/Pd compound. In the weighted spectrum (b) the fit better reproduces the shape of the spectrum by the statistical error in the range of the peaks, since the contribution to the R value is higher, compared to deviations in the background region. The red line represents the best fit result and its shaded area the error bars of the reference spectra.

In a further development of this evaluation method, the error bars of both reference spectra and the measured spectrum are now taken into account. This allows a weighting of the spectra and forces a good fit accordance in the region of the Auger peaks, since they become more pronounced and a deviation in the peak region has a greater influence on the R value than a deviation in the spectrum background, see Figure 5.6.

5.3 Comparison of PAES evaluation methods

The point-by-point summary at the end of this section compares the advantages and disadvantages of both evaluation methods, evaluation by event counting and fit by references, and presents the fields of application. Both evaluation methods were applied to the same spectra of a sample and the comparison is shown in Figure 5.7. Heating cycles of a cover layer of Ni on a Pd substrate are shown and the composition of the surface should be evaluated over time. At first glance, the results appear to show different results. The event counting method shows a constant Ni signal and varying intensities of Pd, whereas the fitting procedure shows a variation of the Auger fraction of both elements, indicating Ni becoming more present at the surface, cf Figure 5.7a. At a closer

look it turns out, that the particular methods consider different aspects of the sample. When comparing the spectra in more detail, see Figure 5.7b and c) it turns out that the Ni Auger peak becomes more pronounced over time, but the total number of Ni events counted has been stable. This means that the surface-related processes are mainly driven by the interaction of Pd. Hence, for the interpretation of data a fundamental understanding of the evaluation procedure is necessary and the evaluation method must be adapted to the respective question.

Event counting

- Direct counting of the events present in each Auger transition of the spectrum without prior processing except for background subtraction.
- Effect of surface contamination or cleaning is visible for each element directly, as it is represented in the count rate.
- Quantification is a lengthy procedure and susceptible to errors.
- Count rate is sensitive to external parameters influencing the measurement (e.g. run of the indoor crane, leading to a deflection of the positron beam) as well as to the age of the sample (residual gas coverage).
- Total sum of counts in the spectra and background level can act as control parameters.
- **Field of application:** Evaluation of time dependent processes to compare the evolution of absolute count rates

Fit by reference

- Evaluation of the relative contributions of elements to a spectrum.
- Absolute intensities are not comparable due to initial normalization of the total sum of counts.
- An increase of an element's contribution doesn't have to be equivalent with migration to the surface.
- A moderate or temporary decrease in primary positron intensity due to external influences does not disturb the result. It may lead to a less distinct fit result, which is represented in the size of error bar.

- Scattered Auger electrons due to surface contamination of the rest gas leading to a broadening of the Auger peaks are not well reproduced, since the reference spectra are mainly recorded from *as-prepared* samples.
- **Field of application:** Evaluation of equilibrium states e.g. at different temperatures to evaluate the elemental Auger contributions

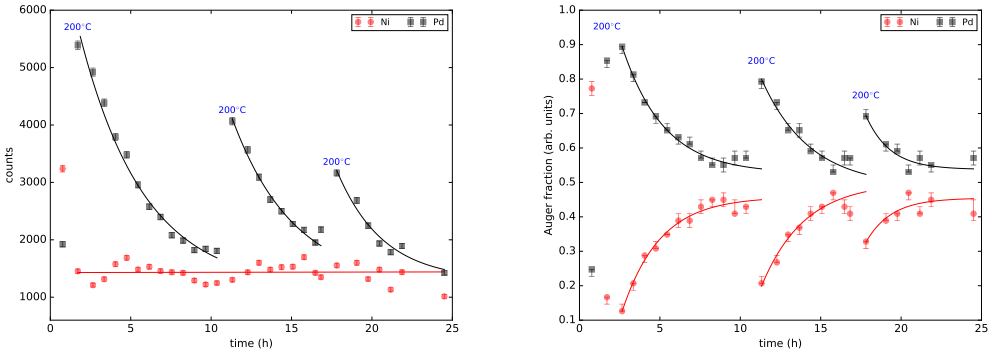

(a) Results of the data evaluation of (left) event counting and (right) the fit by reference spectra.

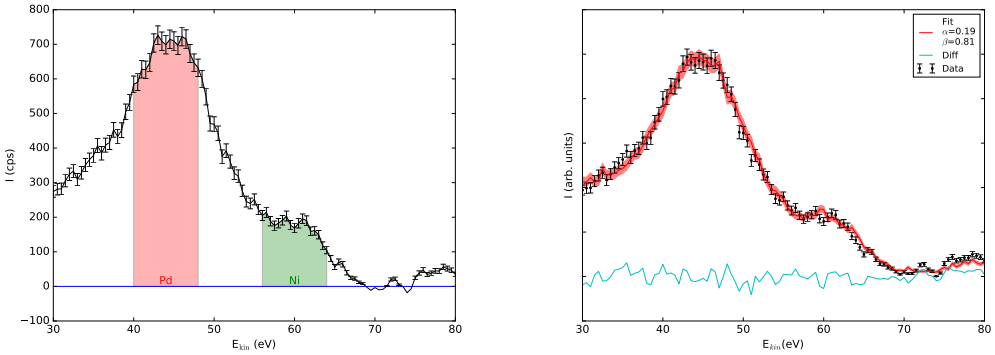

(b) PAES spectrum at 200 °C in the first heating cycle.

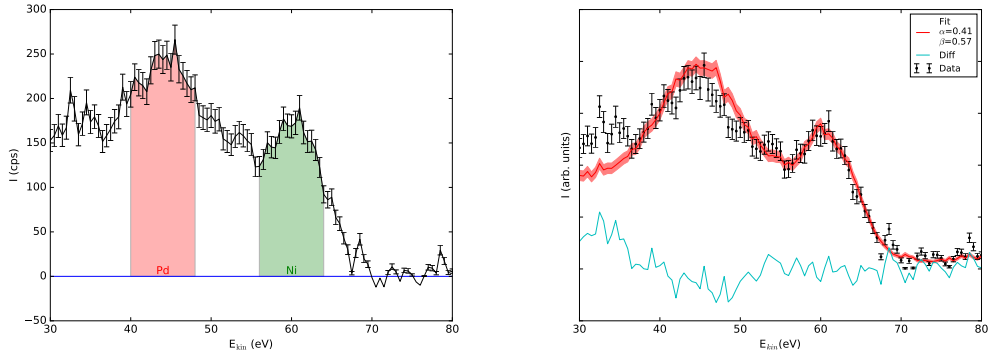

(c) PAES spectrum at room temperature at the end of the first heating cycle. A larger number of scattered Auger electrons can be detected in the energy range between 30 and 35 eV due to surface contamination.

Figure 5.7: a) Illustration of the results of the data evaluation of three heating cycles of 0.7 ML of Ni on Pd. b) PAES spectra of the first heating cycle at 200 °C and after eight hours at room temperature before starting the next heating cycle (c). The absolute number of Ni Auger electrons has almost been constant over time, but the Ni contribution to the spectrum has increased from 0.12 to 0.45.

Chapter 6

PAES measurements

A variety of PAES spectra was recorded to optimize the Auger peak to background intensity and to determine setup-specific parameters such as energy and time resolution experimentally. This is a necessary prerequisite to investigate surface processes in compounds.

6.1 PAES on high purity elements

Initially, PAES reference spectra of the metals spread over a wide range of the periodic table of elements were recorded. As examples, the most prominent Auger transitions of high purity Ag, Cu, Fe, Ni, Pd and Pt are shown in Figure 6.1. All spectra were recorded in the fixed retarding ratio mode of the analyzer with a retarding ratio R=1. Comparing the intensities of the peaks quantitatively as in Figure 6.2, there are markable differences. The intensities are shown with respect to the intensity of the Cu MVV transition and effects of the detector transmission was taken into account. The core annihilation probabilities calculated for a bulk material vary between 5.53 % for Ag and 7.41 % for Ni [11] and hence cannot explain the differences in the detected intensity. The peak intensity of Cu shows a very high counting rate, while the Fe signature is very small. The Auger yield of Cu, Fe and Ni is expected to be close to each other and higher than for Ag, Pd and Pt. Therefore, surface effects due to adsorbates seem to influence the positron wave function leading to different PAES intensities of the elements.

Regarding the spectra of Pd and Pt, in addition to the dominant peak at low energies of about 44 eV, a further Auger transition with lower intensity can be seen. The lower intensity results from the lower core annihilation probability of positrons with electrons of the involved core levels. Using the example of Pt, the core annihilation probability for electrons of the n=5 level, leading to the Pt OVV transition is 8.19 % compared to 1.1 % [7] for electrons leading to the Pt NVV transition. Taking into account the number of electrons in the respective levels, the calculated intensities are in good agreement with the detected signals.

6.1.1 High resolution PAES of Cu $M_{2,3}VV$

Energy resolution is an important issue when analyzing compound sample and the respective Auger peaks need to be resolved. An excellent material to determine the energy resolution for Auger transitions is Cu as the Cu $M_{2,3}VV$ transitions has an energy separation of only 2.2 eV, corresponding to the difference in the binding energy of the Cu $2p_{1/2}$ and the Cu $2p_{3/2}$ core levels [56]. In a survey spectrum, usually this transition is not resolved as two peaks. However, scanning the peak more detailed, the separation is resolvable, see Figure 6.3. The plot shows both acquisition techniques, PAES and EAES, recorded with the same step size of 0.25 eV. The PAES measurement time amounted to 45 minutes. In PAES, the Cu M_3VV peak appears more intense than the M_2VV transition, as the core annihilation probability is higher for this orbital. In case of EAES the ionization cross section and the number of electrons in the respective orbital are relevant for the peak intensities. As the $3p_{3/2}$ level hosts twice as many electrons as the $3p_{1/2}$ shell, the Cu M_3VV peak appears again with a higher counting rate. The separation is clearly visible in both techniques, implying, that the mechanism of ionization in PAES and EAES does not considerably influence the energy differences of the electron shells.

6.1.2 Short term PAES on Pt

The exceptional surface sensitivity of PAES makes it ideally suited for the investigation of surface processes. The connection to the high intensity positron

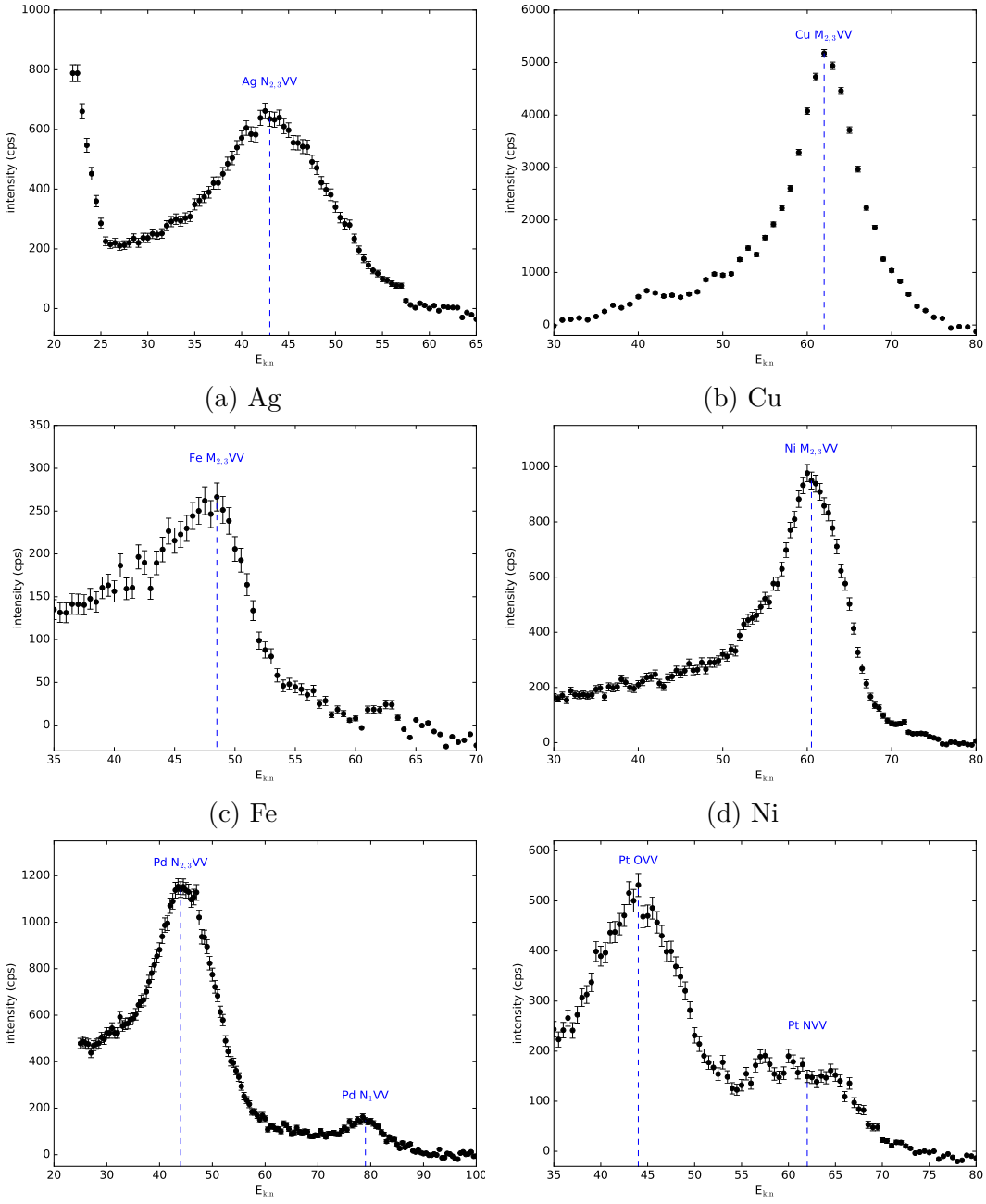

(a) Ag (b) Cu

(c) Fe (d) Ni

(e) Pd (f) Pt

Figure 6.1: PAES reference spectra of high purity elements.

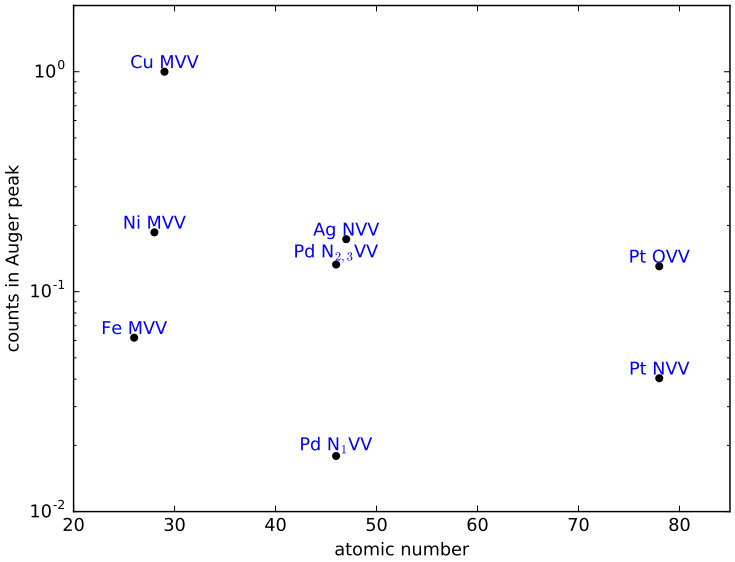

Figure 6.2: Detected PAES Auger intensities versus the element atomic number. The Cu MVV peak intensity is used as standard.

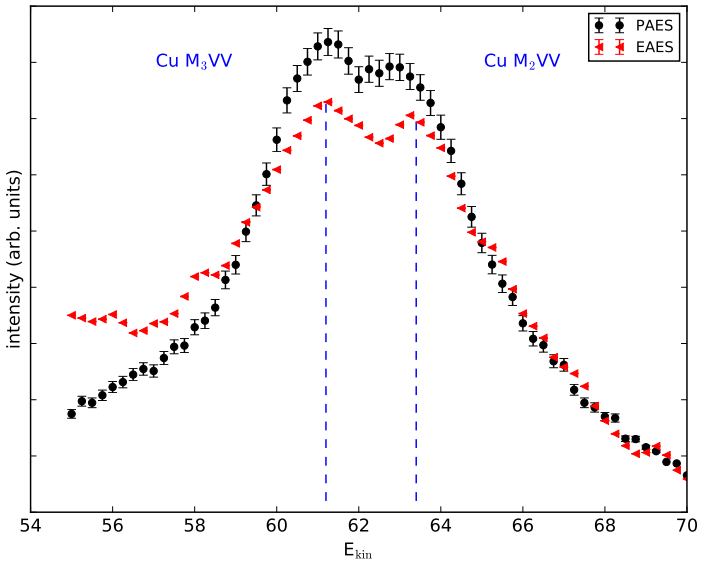

Figure 6.3: High resolution spectrum of the Cu $M_{2,3}VV$ double peak with PAES and EAES. The separation of only 2.2 eV is clearly resolvable.

source NEPOMUC allows the recording of a PAES spectrum within a few minutes. This gave the unique opportunity for a time-resolved observation of the coverage of a well prepared Pt surface with carbon from the residual gas. The low energy Auger transitions of Pt were recorded with a retarding ratio of R=0.3 for a higher transmission. The stack of ten successive spectra is shown in Figure 6.4a. The measurement time amounted to only 230 s for each PAES spectrum. The rapid decrease in intensity is visible directly. The time constants for covering the Pt surface with C could be determined to 26 minutes by taking into account further spectra, where a saturation of the intensity was observed. The saturation level is about 25 % of the initial intensity. This corresponds to the maximum annihilation probability of positrons with atoms in the second atomic layer. In this clarity, these data are not accessible by conventional techniques such as EAES and XPS due to the limited surface sensitivity, though even faster measurement times are possible.

6.2 PAES on Fe/Pt

After the measurements on pure materials to obtain reference spectra and to determine detector specific parameters such as energy and time resolution, a system of two elements has been investigated. The Fe-Pt[1] system has been the subject of numerous investigations in recent years, since FePt in the $L1_0$ phase is a promising candidate for ultra high magnetic storage densities due to its high uniaxial magnetocrystalline anisotropy, see e.g. [83]. FePt typically crystallizes in the A1 phase, an fcc lattice, which is chemically disordered. When annealed at temperatures of more than 600 °C, it transforms to the energetically favored $L1_0$ phase, which forms a chemically ordered fct-lattice [84], see Figure 6.5. It has been shown that the $L1_0$ phase can be stabilized by doping with foreign atoms, e.g. Ag [85, 86]. However, oxidation or segregation processes on the surface may adversely affect the magnetic properties of the system as shown e.g. for Co particles [87].

For segregation at the surface in the Fe-Pt system, more theoretical [88–95] than experimental [84,96] studies can be found in the literature. Therefore, there

[1]The following convention is used in this document: Fe-Pt for the system of Fe and Pt (ordered, disordered, layer systems etc.), FePt for the alloy of Fe and Pt, Fe/Pt for Fe atoms or Fe layers on a Pt surface.

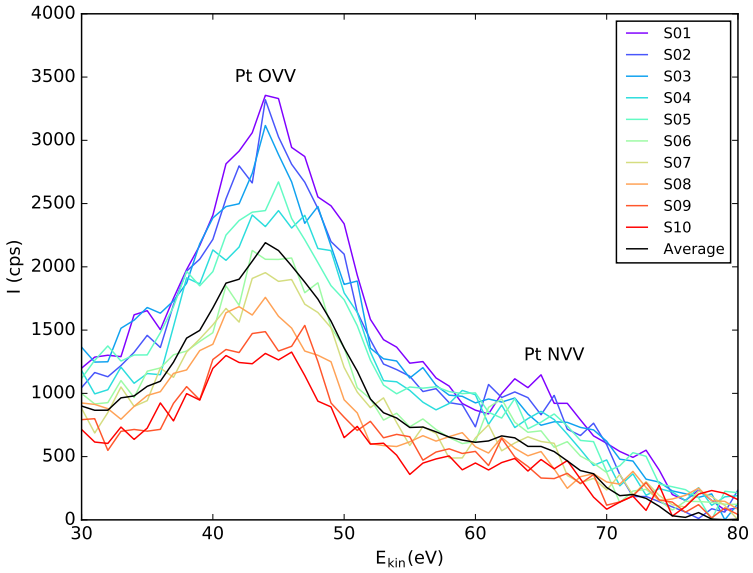

(a)

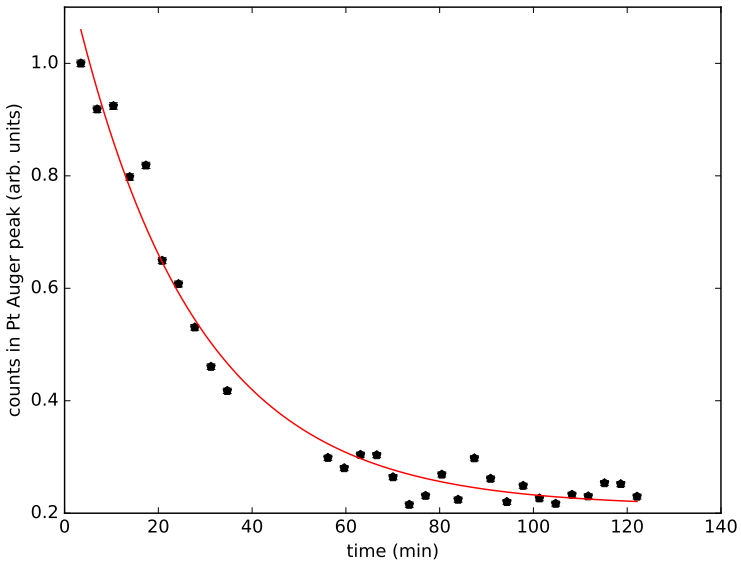

(b)

Figure 6.4: a) Stack of ten successive PAES showing the surface contamination of Pt time resolved. A measurement time of only 230 seconds per spectrum allows this unique insight. b) The quantification of the spectra allows the determination of the time constant for C coverage to 26 minutes^{-1} by an exponential fit.

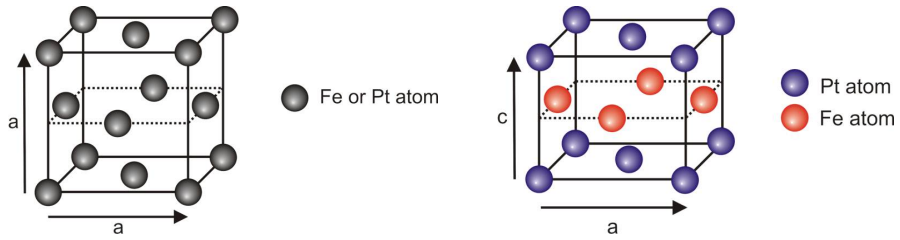

(a) (b)

Figure 6.5: a) Disordered A1 phase and (b) chemically ordered $L1_0$ phase of FePt.

is great interest in studying in situ the development of the surface composition of FePt due to reordering processes such as surface segregation.

In the Fe-Pt system, the coordination of the Fe atoms on the surface plays an important role for the magnetic properties, e.g. whether the surface obtained is hard or soft magnetic [97]. Therefore, the stability of the surface and especially the elemental composition of the topmost atomic layer is of highest interest. The element composition on the surface can change not only by oxidation, but also by possible segregation processes. Monte Carlo simulations of the surface of Fe/Pt show a segregation behavior [93] dependent on the substrate orientation. In FePt nanoclusters, an influence on the oxidizability of the cluster depending on their size was found, which was explained by the formation of a Pt-rich layer on the surface [84]. Therefore, there is great interest in investigating the development of the surface composition of Fe/Pt.

Since Fe/Pt is a model system for surface segregation, the exceptional surface sensitivity of PAES should be used to investigate the process more detailed. Therefore, different cover layers of Fe on polycrystalline Pt substrates were grown and studied with time and temperature-dependent PAES and XPS.

6.2.1 Fe cover layers on Pt

As a reference the spectra of pure Fe and Pt were recorded in the beginning. The PAES signal of Fe was found to be lower by a factor of two, compared to Pt. Auger electrons from the Pt OVV transition have an energy of 44 eV, those of Fe MVV 48 eV. The lower core annihilation probability of positrons with electrons from the Pt orbital with the quantum number n=4 of 1.08 %

sample	Pt fraction	
	PAES	XPS
Pt ref	1	1
0.5 ML Fe on Pt	0.552	0.776
1 ML Fe on Pt	0.441	0.654
2 ML Fe on Pt	0.08	0.574
3 ML Fe on Pt	0	0.266
Fe ref	0	0

Table 6.1: Quantification of the Pt fraction in the Fe/Pt samples obtained in the PAES and XPS spectra.

compared to 8.19 % for the n=5 level [11] makes the Pt NVV transition at 64 eV appear less pronounced.

Subsequently, polycrystalline Pt substrates were covered with Fe by electron beam evaporation starting from half a monolayer up to 3 ML. The PAES spectra are shown in Figure 6.6 a. The PAES spectra of Fe cover layers with thicknesses of 0.5 ML and 1 ML show a significant fraction of Pt of 0.55 and 0.44, respectively. Cover layers with 2 ML and 3 ML are dominated by Fe and show the same low intensity as the Fe reference. The data are summarized in Table 6.1. The normalization to the same intensity leads to an improved visibility of the transition from Pt to Fe with increasing layer thickness, see Figure 6.6 b.

The corresponding XPS spectra, shown in Figure 6.7, reveal a significant amount of C and especially O on the surface of the Fe reference, whereas the Pt surface appears clean. Both samples were similarly cleaned by Ar-ion sputtering at 1keV and have a purity of 99.99 %. The Fe cover layers prepared by electron beam evaporation of a Fe rod with the same purity as the Fe reference show a significantly lower amount of C. The O content increases with increasing Fe layer thickness. It was shown by Giordano et al. [98] that FeO_2 forms a trilayer structure on Pt(111) with O atoms in the outermost layer. Calculations on O adsorption on metals using the example of Cu(100) show, that the core annihilation probability of the Cu 3p is reduced from 6.99 % in case of clean Cu(100) to 1.60 % when one monolayer of O is adsorbed [42]. This in turn explains the reduced Auger intensity for Fe compared to Pt.

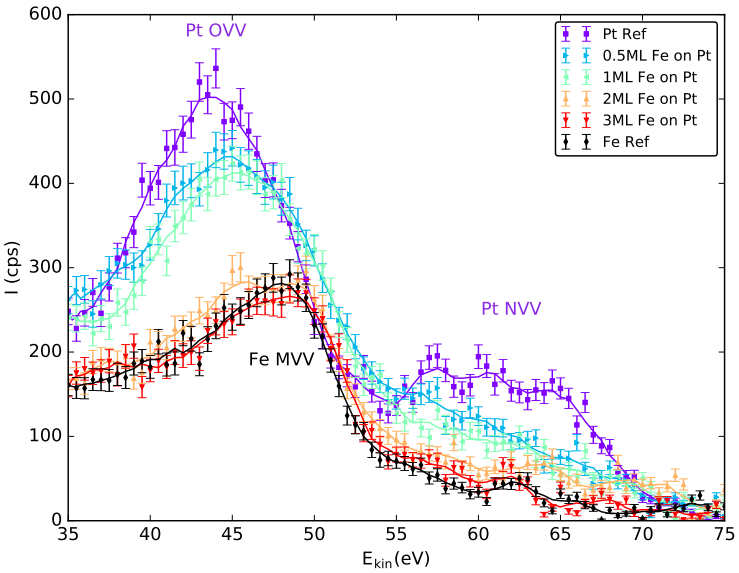

(a) PAES spectra of Fe cover layers on polycrystalline Pt. The Fe Auger signal of Fe is about 50% lower than Pt. Fe cover layers with thicknesses of 2 ML and 3 ML are dominated by Fe, whereas lower covering thicknesses show a strong Pt influence.

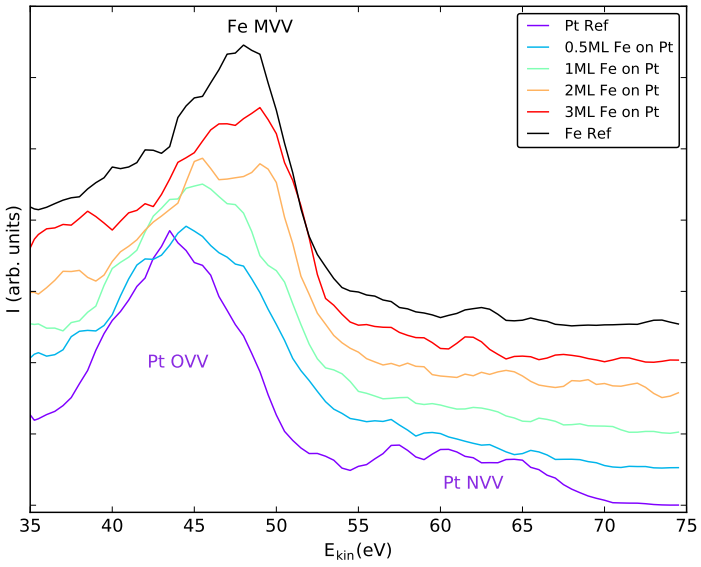

(b) Normalized PAES spectra to show the transition from the Pt dominated to the Fe dominated surface. For a better visibility, the spectra are plotted with offsets.

Figure 6.6: Fe cover layers on polycrystalline Pt.

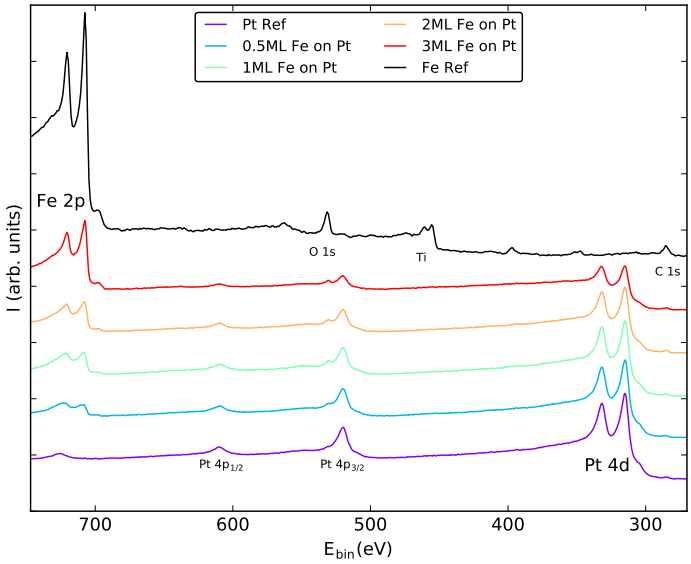

Figure 6.7: XPS spectra of the reference materials Fe in a Ti sample holder and Pt as well as cover layers of Fe on Pt.

6.2.2 Time and temperature dependent PAES on Fe/Pt

To investigate the occurrence of a surface segregation process, a sample with 3 ML Fe on Pt was prepared and spectra were recorded over 12 hours. The intensity of the PAES signal decreases by only 12 % within the measurement time, indicating a low residual gas adsorption, see Figure 6.8 a. The corresponding XPS data show an increase of C, see Table 6.2. No significant change in the elemental composition was hereby observed indicating surface segregation.

For this reason, a new sample was prepared to repeat the measurement at a temperature of 100 °C, to enhance the surface kinetics. By comparing the spectra of the sample 'as-prepared' and the subsequent spectrum at 100 °C an unexpected drop of the PAES signal to only 36 % of the initial value is observed, see see Figure 6.8 b. The XPS data, summarized in Table 6.2, show only small deviations in the elemental distribution, which are negligible compared to the amount of C and O at the surface after 12 hours in vacuum. No peak shifts, indicating a change in the chemical state of Fe or Pt were detected, which could explain the intensity loss.

A competing process to the emission of Auger electrons is the formation of Ps, a bound state of positron and electron. The fraction of positrons forming Ps

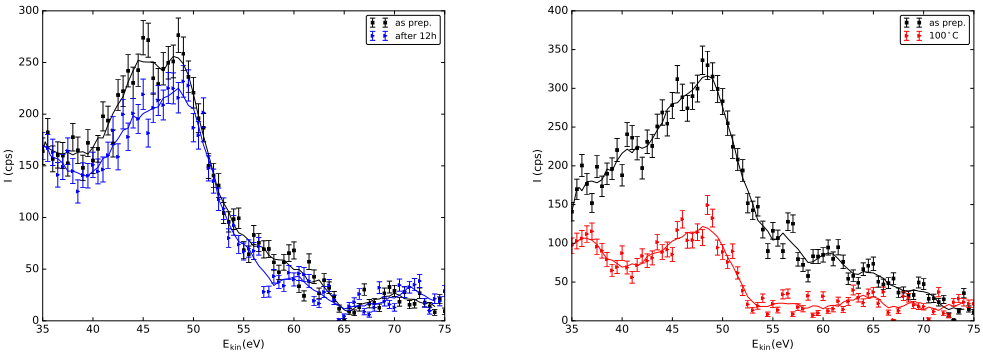

(a) (b)

Figure 6.8: 3 ML Fe on Pt: (a) time and (b) temperature dependent PAES.

	$\%_{at}$			
	C	O	Fe	Pt
sample 1				
as prep.	3.6	4.2	65.5	26.8
after 12h at RT	15.2	7.9	53.7	23.2
sample 2				
as prep.	4.6	3.8	61.4	30.1
at 100 °C	6.8	3.8	59.3	30.1

Table 6.2: Summary of the XPS data of the time and temperature dependent measurement on 3 ML Fe on Pt.

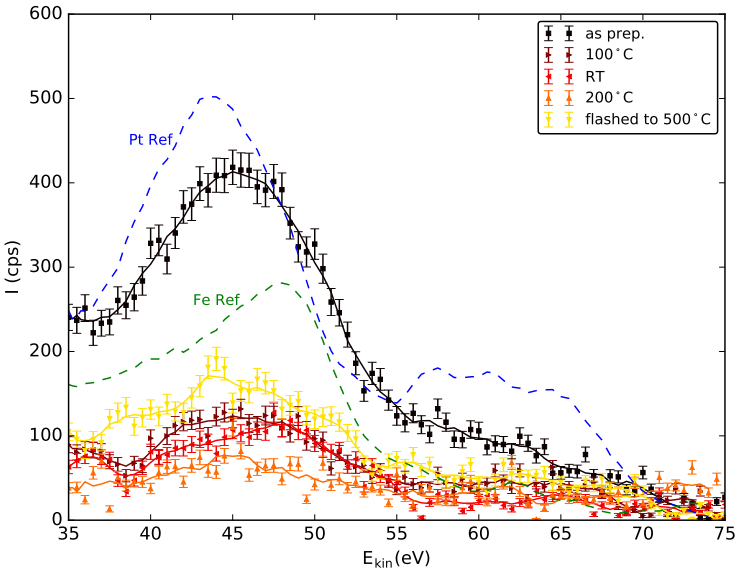

Figure 6.9: PAES spectra of 1 ML Fe on Pt depending on the sample temperature starting at room temperature. The lines are to guide the eye. The spectra of pure Fe and pure Pt serve only as a reference.

depends on the temperature [99]. At the surface the formation and emission rate grows with increasing temperature. To investigate the effect of Ps formation, a sample with only 1 ML Fe on Pt was prepared and PAES spectra were recorded at variable temperatures, shown in Figure 6.9.

Table 6.3 summarizes the fraction of Fe and Pt in the PAES spectra as well as the measured intensity. For the quantification the spectra were fitted by the reference spectra. Beginning at room temperature, the spectrum shows an almost equal fraction of Fe and Pt. The intensity reduction as observed in the previous sample with 3 ML Fe on Pt can also be reproduced with this lower Fe layer thickness. At 100 °C the signal decreases to 34 % of the initial value and remains at a low intensity, even when the sample is cooled down to room temperature again. At 100 °C the Fe fraction appears to decrease to about 0.4 and increases after cooldown to about 0.8. However, due to the low count rate, the fit error is large. The spectrum recorded at 200 °C shows a further reduced signal with only 22 % of the intensity of the 'as-prepared'-sample. For this spectrum, a fit is almost impossible and results show a very large variation. After the sample was cooled down from again to room temperature it was heated up to 500 °C within few seconds (flashing). After this, an increase of

sample	Auger fraction				intensity
	Fe		Pt		
as-prepared	0.51	+0.04 -0.06	0.49	+0.06 -0.04	1
100 °C	0.41	+0.10 -0.10	0.51	+0.10 -0.16	0.34
RT	0.83	+0.12 -0.10	0.09	+0.12 -0.12	0.27
200 °C	0.19	+0.22 -0.19	0.57	+0.24 -0.35	0.22
flashed	0.37	+0.08 -0.08	0.57	+0.10 -0.10	0.44

Table 6.3: Quantification of the PAES spectra of 1 ML Fe on Pt. The fit range indicates the minimum and maximum of the fit error. The intensity compares the total number of counts in the spectra with respect to the as-prepared spectrum.

the Auger signal was observed to at least 44% of the initial intensity. An Pt fraction of 0.57 can be detected, which could explain the increasing intensity.

In the corresponding XPS data no variation of the Fe fraction of approximately 30 % can be detected within the error at elevated temperatures. The Pt fraction shows some variation, which is in the order of the observed increase of C. After flashing, a very low O fraction of 1.6 % is detected, compared to 4.8 % at 200 °C.

From the results one can conclude, that the increased formation of Ps at higher temperatures seems not to be the decisive factor, because the intensity does not increase after cooling down to room temperature. Due to the high reactivity of pure Fe, an oxidation of the surface layer might be already completed at the beginning of measurement, which is in agreement with the XPS data. The XPS data show no evidence for C enrichment of the surface layer when the sample is heated up. C could have been implanted in the sample, e.g. during Fe evaporation and diffuse to the surface layer during heating. Furthermore, the PAES spectra show an overall decrease of the Auger intensity. When C atoms form a cover layer to the Fe but do not affect the Pt atoms, a decrease of only the Fe fraction is expected. In case of a full coverage of the surface, as known from samples exposed to the residual gas for some hours, the decrease of the PAES signal is less significant. In summary, the

effect of adsorbates leading to a change in the surface charge distribution seem to influence the positron wave function allowing no reliable PAES study on the surface segregation.

Comparison with Ni on Pt

In a comparative study, Fe was replaced by Ni, which is less reactive. Furthermore the XPS spectrum of a pure Ni foil showed a significantly lower amount of C and O on the surface. The Ni $M_{2,3}VV$ Auger transition overlaps with the Pt NVV peak but due to the according core annihilation probability, the intensity of the Pt NVV transition is only 13 % of the Pt OVV intensity. Therefore, both elements are well distinguishable in the spectra.

A polycrystalline Pt substrate was covered with 0.5 ML of Ni and the sample was heated stepwise up to 250 °C with intermediate cooling to room temperature. The results are shown in Figure 6.10. The spectrum at 100 °C shows only a moderate loss in intensity compared to the 'as-prepared' sample at room temperature, which is in accordance with contamination from the residual gas. When cooling down from 100 °C the Pt signal seems to disappear. In the next heating cycles to 150 °C and 200 °C, a reduction of the Ni signal is observed, too. The spectra appear as almost horizontal lines with a slight elevation at the energy of the Ni MVV transition and a markable drop to lower count rates at energies of more than 67 eV. At a temperature of 250 °C no signal of Ni or Pt can be detected any more even after cooling down. Again, the XPS spectra do not indicate a change in the surface composition or the chemical states.

Since the decrease in Pt intensity was observed first, temperature dependent PAES spectra were recorded on pure Pt. The previously studied systems showed a decrease in intensity at 100 °C in case of Fe/Pt and at 150 °C in case of Ni/Pt. Therefore, the temperature was increased in small steps of about 10 °C in the range between 30 °C and 150 °C. A selection of the spectra at representative temperatures is shown in Figure 6.11. A minor decrease of the signal can be observed, but this is also compatible with residual gas coverage, especially since the intensity increases slightly at 150 °C.

Another aspect is the interaction of hydrogen from the residual gas in the chamber with the sample surface. H adsorption on platinum has been

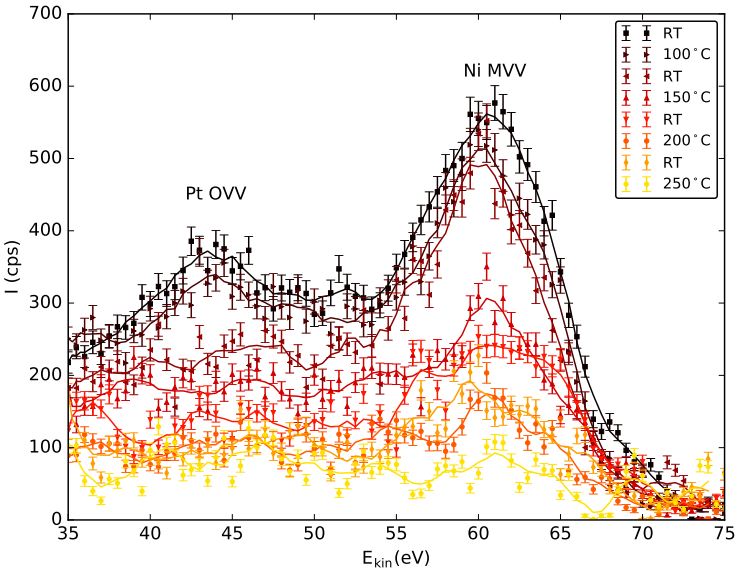

Figure 6.10: PAES spectra of 0.5 ML Ni on Pt depending on the sample temperature beginning from room temperature up to 250 °C. The lines are to guide the eye.

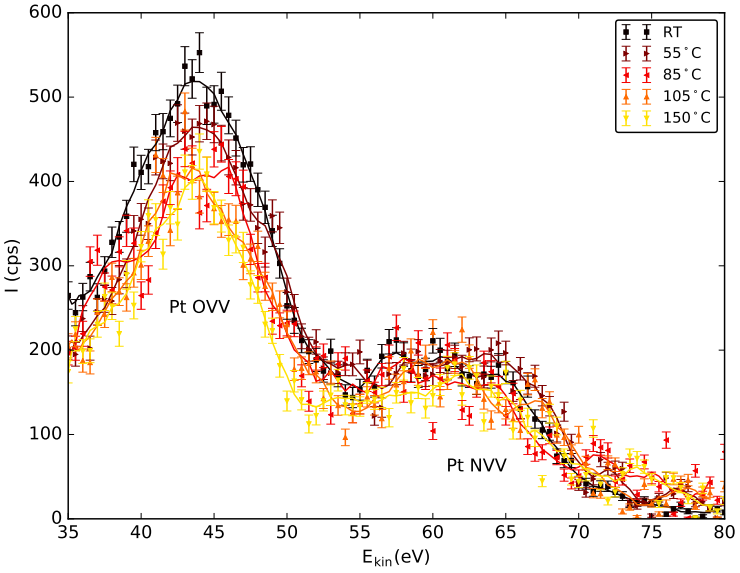

Figure 6.11: PAES spectra of 0.5 ML Ni on Pt depending on the sample temperature. The lines are to guide the eye.

studied extensively for catalytic application [100]. However, with Auger electron spectroscopy no direct observation of H is possible. To find evidence in XPS is rather difficult, since H causes mainly low energy shifts due to changes in the binding energy or small changes of the band structure near the Fermi level.

A decrease of the PAES signal can indicate Ps formation, apart from several additional aspects discussed previously. However, Ps cannot be studied by this spectroscopy technique directly. However, for PAES studies on surfaces with a enhanced Ps formation, additional information from Ps might be provided for a better understanding of surface processes.

In summary, it can be shown that surface processes such as surface segregation or diffusion of atoms cannot be studied independent from effects of oxidation, adsorbates, Ps-formation or H interaction. Calculations by Jensen and Weiss [11] on the core annihilation probability of positrons on metal surfaces showed significant reduction of the PAES signal of the metal substrate when the adsorption of impurities on the surface is taken into account. For example in case of Cu(100) the core annihilation probability of positrons with electrons of the 3p shell turned out to be reduced from 3.02 % for a clean surface to 1.62 % with an adsorbed overlayer of C. Large differences were also found depending on the adsobed element. The adsorption of O shows a core annihilation probability of the Cu 3p shell of 1.72 %, whereas an overlayer of S reduces the probability to only 0.74 %, due to the different adsorption sites. Table A.1 and Table A.2 summarize the core annihilation probabilities calculated for different adsorbates and cover layer thicknesses on Cu(100).

The repeated heating may also enhance getter effects of the sample surface or increase the diffusion of impurities from the bulk to the sample surface. Therefore, future studies will be focused on the evolution of the distribution of surface elements at a specific temperature.

Chapter 7

PAES on Ni/Pd

The elements Ni and Pd play a key role in a wide range of catalytic applications. Functional materials and surfaces based on Pd are applied e.g. for heterogeneous catalysis and for hydrogen purification. For industrial applications, several aspects play an important role such as the chemical composition of the Pd surface, which influences the catalytic properties substantially, and the mechanical stability e.g. of thin membranes, which is affected by foreign atoms or segregation processes. For hydrogenation, Ni is the central catalyst for more than 80 years [101]. Since the invention of Raney [102] Ni as a catalyst is present in many synthetic transformations ranging from cross coupling reactions in which carbon-carbon bonds are formed for the reduction of electron rich carbon bonds.

Nowadays, combinations of different catalytically active materials are used in order to increase efficiency and reduce costs. For example, del Rosario et al. [103] showed that the efficiency of direct-ethanol fuel cells can be increased by using a catalyst with a Ni-Pd bilayer structure instead of pure Pd. Theoretical calculations made for Ni on a Pd surface predict Ni atoms to migrate to the second atomic layer [18, 104] for all crystallographic Pd orientations [105]. Experimental results on a Ni-1$_{\mathrm{at}}$ % Pd alloy studied with Auger Electron Spectroscopy (AES) in a temperature range of 550 to 800 °C show a moderate enrichment of Pd of the surface [106]. In Low Energy Electron Diffraction (LEED) studies on a $Ni_{50}Pd_{50}(100)$ surface an oscillatory segregation profile with a Pd enriched surface layer and Ni enrichment in the second layer is observed [107]. Khanra et al. demonstrated the effect of surface segregation

on the catalytic activity of alloys using CO hydrogenation on a Pd-Ni(111) surface [108]. The influence of the annealing temperature on the surface segregation was shown by Li et al. on Au/Pd(111) using LEED and Low Energy Ion Scattering (LEIS) [109]. To achieve long-term stability of more sophisticated catalysts, the driving forces at surfaces leading to e.g. segregation, diffusion and temperature dependent interaction of surface atoms need to be understood, since they may significantly influence the catalytic activity.

7.1 Sub-monolayer coverage of Ni on Pd

Sub-monolayers of Ni on a polycrystalline Pd substrate were investigated with PAES. Beginning with references of pure Pd and pure Ni, the thickness of the Ni cover layer on the polycrystalline Pd substrate was increased in steps of 0.1 ML beginning with 0.1 ML to 0.5 ML, followed by samples with 0.7 ML, 1 ML and 4 ML of Ni on Pd, see Figure 7.1. Starting from the Pd reference, a decrease of the Pd signal with a simultaneous increase of the Ni signature can be detected as expected. The spectra of 1 and 4 ML Ni on Pd show a higher intensities in the lower energy range between 38 eV and 50 eV than the Ni reference. This might result from inhomogeneous growth of the evaporated Ni on the Pd substrate, leading to a higher fraction of scattered Ni Auger electrons than for a homogeneous and flat surface, or due to the possible growth of islands, hence Pd can still be detected.

For further analysis, the spectra can be well approximated by a linear combination of the spectra of the reference materials. To estimate the contribution of each element to the PAES spectra, the events in fixed energy Regions Of Interest (ROI) around the Auger peak positions were summed up, as described in detail in Section 5.2.1. The Auger transitions Pd $N_{2,3}$VV at 43 eV and Ni $M_{2,3}$VV at 61 eV were evaluated. Each ROI was set to a width of 8 eV, corresponding to the FWHM of a Gauss fit of the Auger peaks.

The contribution of the respective elements to the PAES spectra is shown in Figure 7.1. For ideally grown layers, one would expect a linear correlation of the Auger intensities with equal contributions for both elements, due to the same Z_{eff}, only deviating by the difference in the core annihilation probability, which is lower for Pd 4p with 6.07 % than for Ni 3p with 7.41 % [11]. This is in

good agreement with the results shown here. For the samples with a coating of 1 ML and 4 ML the intensity is larger than 90%, but it does not reach 100 % of the Ni reference. This deviation might result from surface inhomogeneities mentioned above.

The complementary XPS spectra are shown in Figure 7.2. Even at a Ni layer thickness of 4 ML, a Pd content of 29.1 % can be derived from the Pd 3d peak. All spectra show low amounts of C and O below 10 % and 5 %, respectively. The Pd $3p_{3/2}$ photopeak overlaps with the 1s peak of O. Therefore, the O fraction is determined by evaluating the intensity ratio of Pd $3p_{3/2}$ to Pd $3p_{1/2}$, which should be 2:1, corresponding to the number of electrons in the respective orbital. The deviations are contributed to O.

7.2 Time-dependent PAES on 0.5 ML Ni on Pd

The evolution of the Ni and Pd signals of a sample with 0.5 ML Ni on Pd was investigated by alternating measurement with PAES and XPS at room temperature. For this purpose, the time-dependent fraction of Ni and Pd was evaluated using PAES and XPS spectra. For example, several PAES raw spectra are shown in Figure 7.3. A change in the intensities of Ni and Pd can be clearly observed with the naked eye. The overall decrease in the intensity results from the contamination of the surface by the residual gas, which is confirmed by an increase of carbon detected by XPS. However, even 10 hours after sample preparation the signature of Ni and Pd is clearly detectable.

In order to determine the fraction of the Auger signals of the respective elements, the events in a fixed energy ROI of the Auger peak were evaluated as described in Section 5.2.1. For the quantification of the XPS spectra, the Pd 4d and the Ni 2p photopeak were fitted using CasaXPS as a standard software for XPS analysis. The details of this evaluation technique are described in Section 5.1.

The results of the PAES and XPS spectra are shown in Figure 7.4. The data reveal a remarkable difference in the fraction of Ni and Pd for the respective methods. The initial Ni intensity in the PAES spectra is more than three times higher than that in the XPS spectra. Assuming that at the beginning

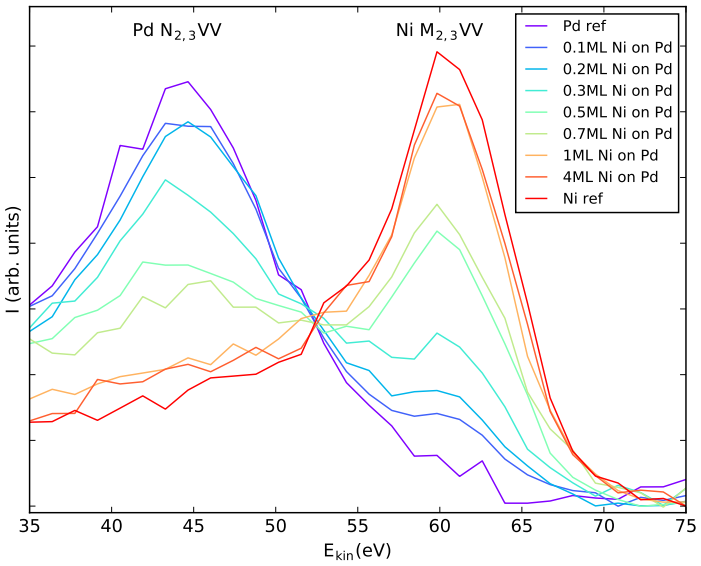

(a)

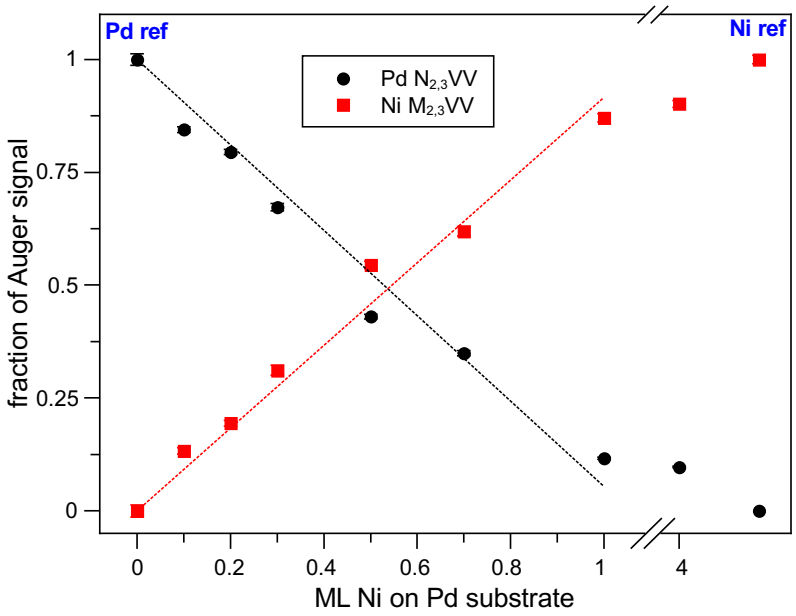

(b)

Figure 7.1: a) PAES spectra of pure Ni, pure Pd, and Pd coated with 0.1 ML to 4 ML Ni. The spectra are normalized and a constant background was subtracted (FRR mode, R=1).
b) Fraction of the Auger intensities of Pd and Ni in the measured PAES spectra (errorbars within the symbols). Published in [52].

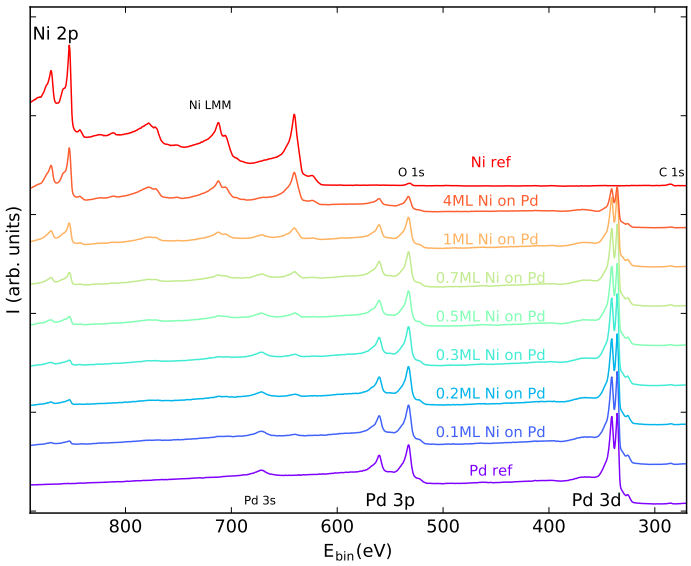

Figure 7.2: XPS spectra of pure Ni, pure Pd, and Pd coated with 0.1 ML to 4 ML Ni. The intensities of C and O are found to be below 10 % and 5 %, respectively, in all spectra.

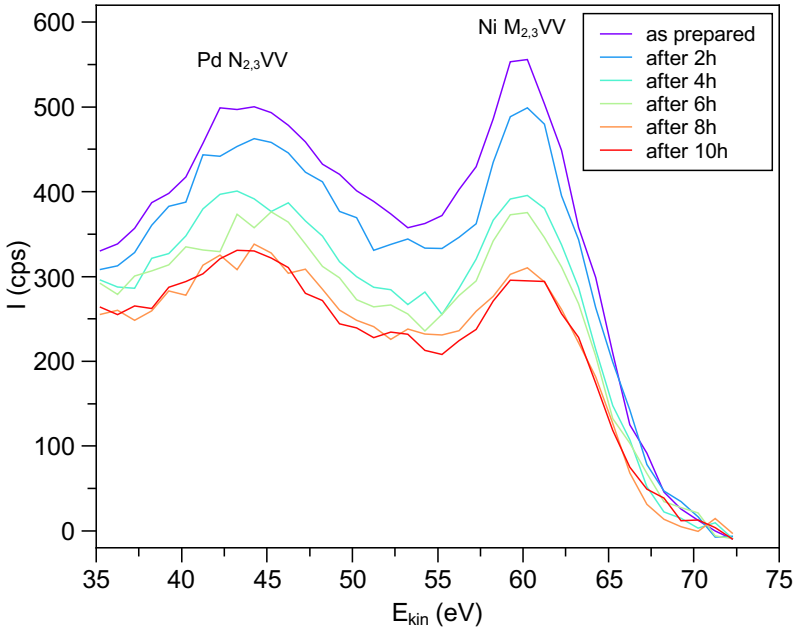

Figure 7.3: Time-dependent PAES spectra of the 0.5 ML Ni on Pd. The overall decrease in the intensity results from coverage from the residual gas. Additionally, changes in the intensities of Ni and Pd are visible. Published in [52].

no surface rearrangement took place, for PAES one would expect the same intensity for both elements slightly influenced by the difference in the core annihilation probability for the respective elements, as previously discussed in Section 7.1.

For XPS the surface sensitivity is determined by the IMFP of the photo electrons and thus by their energy. The IMFP for the evaluated Ni 2p photoelectrons is in the range of 10.4 Å, while the one for Pd 3p electrons is around 17.4 Å [110]. Thus, the XPS signal represents a weighted average over several atomic layers, leading to a far smaller contribution of Ni.

Both analysis methods, PAES and XPS show the same tendency of Ni to decrease and Pd to increase as a function of time. Due to the intrinsic higher surface sensitivity, the intensity change of the Auger peaks is much more significant with PAES, i.e. the Ni signal decreases by about 12% within 13 hours. XPS shows a decrease of only 4% with respect to the initial intensity within 15 hours.

Although a saturation of the values obtained by PAES after about 11 hours cannot be excluded and the data of the XPS spectra largely scatter, a linear fit was performed in the first approximation, in order to estimate the characteristic time for the variation of the respective fractions, leading to a decrease of the Ni intensity of $(5.1 \pm 0.5) \cdot 10^{-3}\mathrm{h}^{-1}$ for PAES and $(5.3 \pm 2.0) \cdot 10^{-4}\mathrm{h}^{-1}$ for XPS.

The clear decrease of the Ni Auger signal obtained with PAES is attributed to a rearrangement of the Ni atoms within the first layers of the surface. Since XPS is less sensitive to the topmost atomic layer this effect is much less visible. Two dimensional reordering is excluded since typical diffusion coefficients for Ni on a surface at room temperature is on the order of seconds to minutes and hence cannot explain the observed decrease. Within the measurement time, a clear surface segregation, i.e. the most stable configuration of Ni atoms e.g. in the second atomic layer, is not observed. However, as a slight deviation from the linear decrease after about 11 hours (red data in Figure 7.4 a)) reaching of a saturation value cannot be excluded. A discussion on the effect of surface contaminates from the residual gas on Ni and Pd studied by XPS is found in the next section.

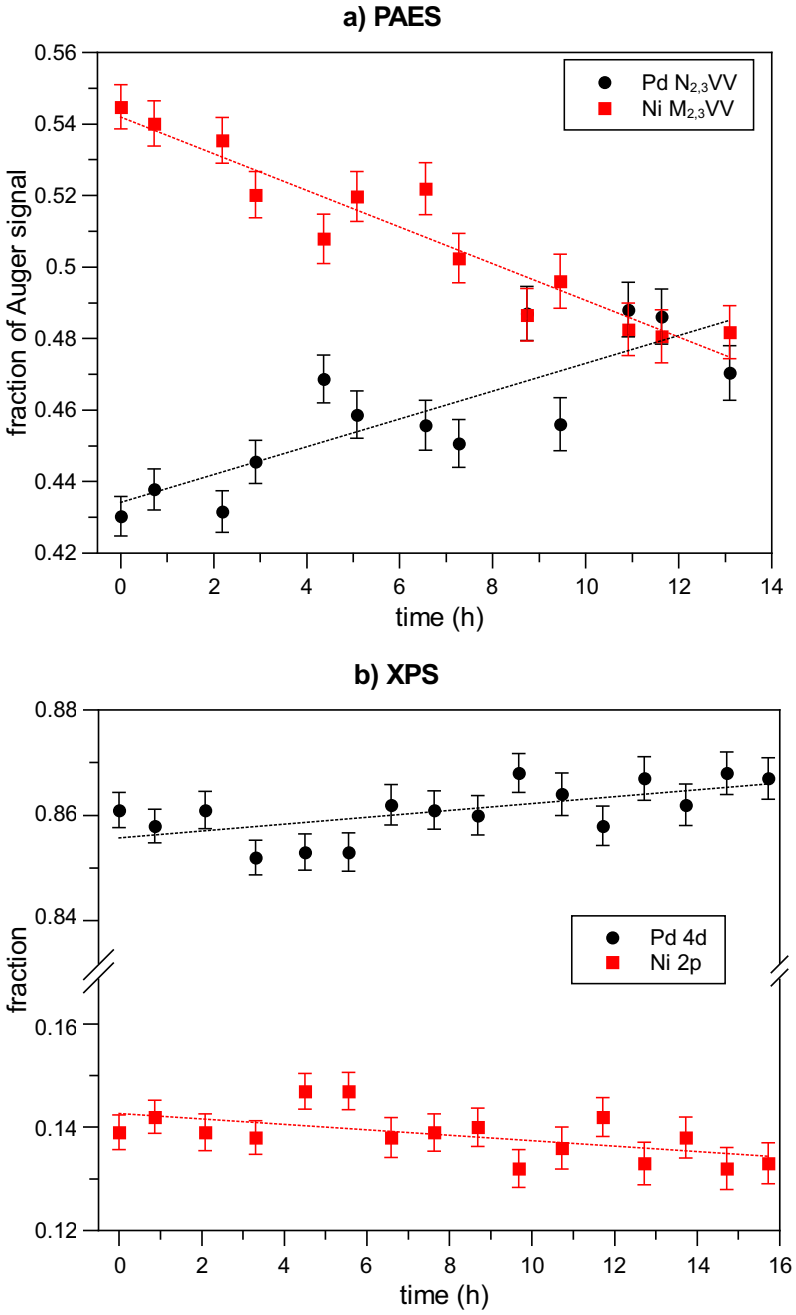

Figure 7.4: a) Comparison of the time-dependent fraction of Ni and Pd in PAES and (b) XPS on 0.5 ML Ni on Pd. Both methods show the same tendency, but due to the higher surface sensitivity of PAES, the effect is more significant. Published in [52].

7.3 Surface contamination of Ni and Pd studied by XPS

To rule out effects of surface contamination leading to the observed phenomena, the main surface adsorbates C and O were monitored by XPS on pure Ni and Pd during a period of 8h for the Ni reference and over 13h for the Pd reference with an interval of 1h. For the evaluation of the spectra, the Ni 2p, the Pd 3d and the 1s photo peaks of C and O were analyzed. The time constants for the XPS data were evaluated by fitting exponential functions to the intensity change of the photo peaks for the decrease of Ni and Pd and the increase of C, respectively. The time constants of PAES and XPS are summarized in Figure 7.5. Oxygen was found on the surfaces of both, Ni and Pd, but no significant change of the O fraction was observed within the measurement time. Therefore, the fit is compatible with a constant function. A significant increase of C was detected on both materials, with a characteristic time constant which is in good agreement with the decrease of the signal of the respective substrate material. Therefore, the time constant for C seems to be independent of the substrate material. Different adsorption sites were reported e.g. for O on a partial layer of Au on Si [9], leading to similar PAES results. The slide deviation of the time constant of the Ni 2p signal might be an effect of the IMFP of electrons due to the higher binding energy of this orbital (∼860 eV) compared with the one of C 1s (∼284 eV) and Pd 3d (∼337 eV), leading to a lower IMFP, i.e. Pd 3d electrons are more likely to be detected than Ni 2p electrons, even when covered by e.g. 1ML of C.

The evaluation of the normalized PAES spectra showed a significant increase in the Pd signal while the Ni signal decreased. As the energy of the Auger electrons from Pd $N_{2,3}VV$ (43 eV) and Ni $M_{2,3}VV$ (64 eV) does not differ very much the IMFP is almost the same for both elements. The time constants from the PAES data for the decrease of Ni and the increase of Pd significantly differ from the one of C, therefore the measured results cannot be explained by the coverage of C.

In summary it was shown that O contamination is present in both samples, Ni and Pd, but remained constant during the measurement time. As shown by XPS, the characteristic time constants for the increase of C and the decrease of

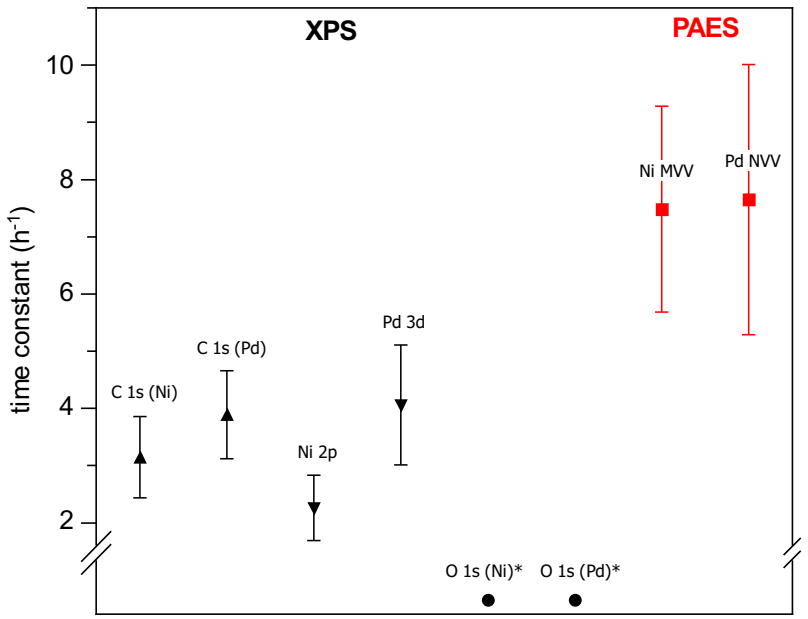

Figure 7.5: Characteristic time constants for the main contaminations C and O on pure Ni and pure Pd measured by XPS, as well as the time-constants for Ni and Pd of the Pd sample with a 0.5 ML Ni cover layer investigated by time-dependent PAES. Triangles pointing upwards indicate an increase and triangles pointing downwards a decrease of the intensity. (*) The O contamination remained constant during the measurement time. The time constants found for Ni and Pd determined by PAES significantly differ from those of the XPS results for C, therefore the PAES data are interpreted as a superposition of C contamination and structural changes at the sample surface. Published in [111].

Ni and Pd, respectively, are similar. The time constant for C differs by a factor of two from that of the PAES results for Ni and Pd. The contamination of the surface by C and O cannot explain the intensity change in the PAES data. Therefore it is concluded that a rearrangement of the Ni and Pd atoms in the topmost layers of the surface took place with a characteristic time constant in the order of hours.

7.4 Segregation of Ni adatoms on oriented Pd surfaces

The complex interplay of surface processes is subject of the first time in-situ temperature-dependent study on the stability of Ni adatoms on single crystalline Pd substrates with three different low index surface orientations. In order to characterize a low Ni coverage, i.e. Ni with a nominal thickness of less than 1 ML or to observe surface segregation PAES is applied.In addition, XPS is applied to verify the comparability of the prepared samples, to analyze the elemental composition of the surface near layers, and to evaluate the influence of residual gas.

As a reference, the PAES spectra of pure Pd and pure Ni were recorded in advance in an energy range of 35 eV to 75 eV showing the Pd NVV and Ni MVV Auger transitions. The fixed retarding ratio-mode with a step width of 0.5 eV and a retarding ratio of one was used. These detector parameters were also selected for the actual measurement on the Ni/Pd samples. The measurement time for a PAES spectrum amounted to 40 minutes. Each PAES measurement was accompanied by XPS. The analysis of the photopeaks allows an estimation on the elemental composition in the near-surface layers. Moreover, surface contamination caused by the residual gas in the UHV chamber and chemical shifts can be detected. During the whole measurement time, the temperature of the sample is kept constant, before increasing to the next temperature step.

To quantify the PAES spectra, the recorded data of the compound is fitted by a model function, which is assumed as a linear combination of the reference spectra of the pure elements Ni and Pd using independently scaled fractions α and β. In the applied fitting procedure it is not a requirement that the sum of the scaling factors α and β has to be unity. This condition would presuppose

that the line shape of an Auger transition is not influenced by the presence of additional elements, or by chemical bonding. For this reason, the scaling factors are varied independently. The fitting procedure is described in detail in Section 5.2.2. For the evaluation of the XPS spectra the Ni 2p and Pd 3d photopeaks were quantified, using the standard quantization of CasaXPS [78].

Figure 7.6 shows the PAES spectra of the three different Pd substrate orientations coated with a single atomic layer of Ni in the temperature range between 30 °C and 350 °C. The Auger transitions Pd NVV at 43 eV and Ni MVV at 64 eV are clearly detectable. These low energy Auger transitions have a width of several eV, which mainly results from the broad valence band. Because of the isoelectronicity of Ni and Pd the effective atomic number and hence the Auger yield for the MVV and NVV transition, respectively, is equivalent.

Both, temperature and substrate orientation appear to strongly influence the relative intensities of the two elements. A fast decrease of the Ni intensity is clearly observed in the raw spectra at moderate temperatures of 150 °C for the Pd(111) substrate, whereas for Pd(110) no significant decrease can be detected up to 250 °C. Independent of the Pd substrate orientation, at 350 °C the spectrum is dominated by the Pd signal for all samples.

The measured data are well reproduced by the model function of the reference spectra. The fit results are shown as solid lines in the spectra of Figure 7.6 and the Ni intensity is quantified in Figure 7.7a, where a value of one represents pure Ni. An average Ni intensity of 0.72 is detected at room temperature, but only 0.08 at 350 °C. Although a nominal thickness of one atomic layer of Ni was put on the Pd, the measurement signal also shows a small contribution of Pd. Despite a low evaporation rate of only 6 Å/minute, a certain inhomogeneity of the layer thickness can not be excluded. Moreover, a fraction of 5 to 20 % of the PAES signal may originate from the second atomic layer depending on the positron probability density at the surface [11]. All Pd orientations show a strong tendency for segregation as predicted from theoretical calculations, leading to a Ni depletion of the surface. This corresponds to the fact that at a temperature of 350 °C, only a very low Ni amount can be detected for all Pd surfaces. The course of the Ni decrease can be described by a simple model, implying that an activation energy is needed to initiate the segregation process. The temperature dependency can hence be expressed by the equation

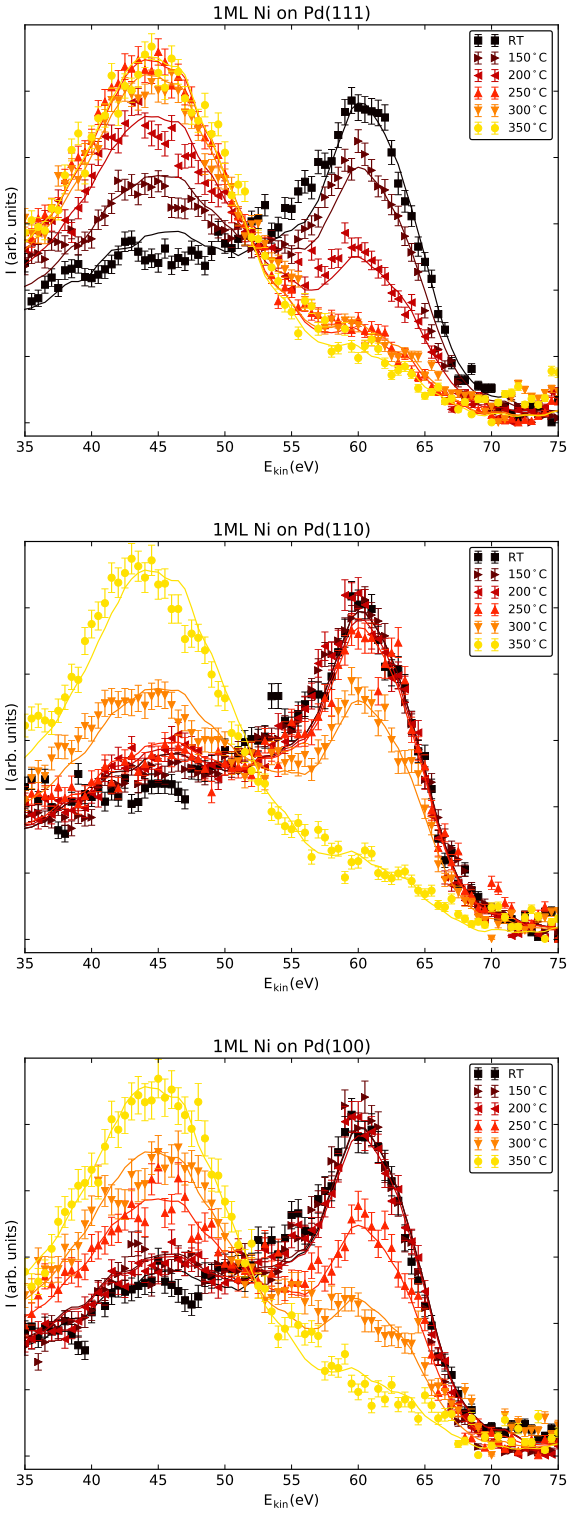

Figure 7.6: Temperature dependent PAES spectra of one ML of Ni on Pd(111), Pd(110) and Pd(100). The solid lines represent the fit result for the quantification of the Auger intensities of Ni and Pd, respectively.

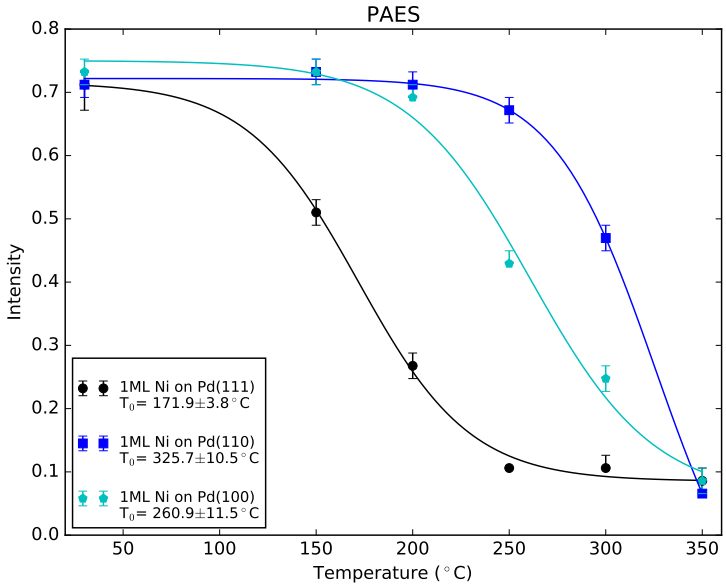

(a)

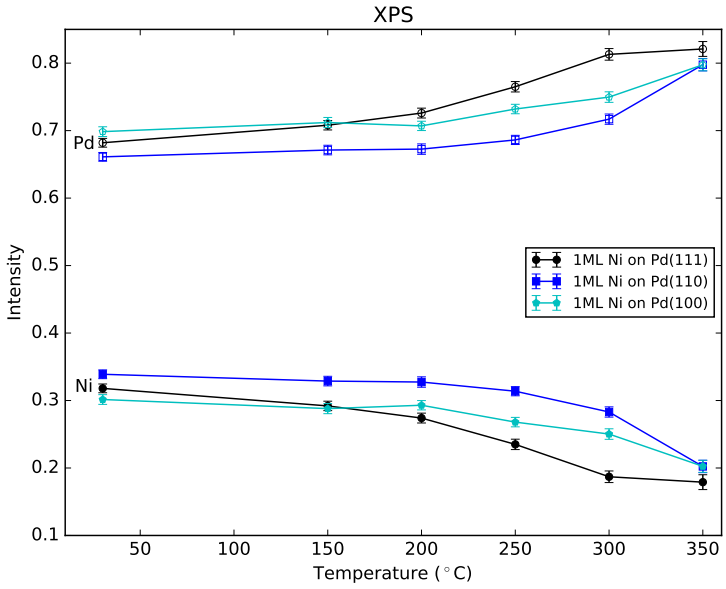

(b)

Figure 7.7: a) Ni intensity of the PAES spectra as a function of temperature for different Pd substrate orientations. The activation temperatures T_0 result from the fit function given in Equation 7.1. b) Intensities for Ni and Pd derived from the XPS data. Note the same axis scale of the intensity.

$$I(T) = \frac{-C_1}{1 + \exp(-C_2 \cdot (T - T_0))} + I_0 \tag{7.1}$$

where T_0 denotes the corresponding activation temperature, while C_1 and C_2 are shaping parameters. The results of the quantification in Figure 7.7a were fitted using this model, leading to the lowest activation temperature of 172(4) °C for Pd(111), followed by 261(12) °C for Pd(100) and 326(11) °C for Pd(110). The exact value and its error for each crystallographic orientation are given in Figure 7.7a. The corresponding activation energies amount to 38.4(3) meV for Pd(111), 46.0(10) meV for Pd(100) and 51.6(9) meV for Pd(110).

The complementary XPS data was evaluated by quantifying the photopeak intensity as described in the previous section, see Figure 7.7b. The mean detected Ni intensity in the three as-prepared samples at room temperature is 0.32. The individual samples show only slight deviations from the mean value and thus indicate a uniform sample preparation. No peak shifts of the Pd 3d and Ni 2p photo peaks were found in the data evaluation, which would indicate a contamination due to the rest gas during the measurement. A decrease of the Ni intensity with increasing temperature is found for all samples, showing a minimal value of 0.19 at 350 °C. This is a reduction of only 40% in contrast to nearly 90% for the PAES results. The XPS data substantiate the PAES results, though they are less significant because of the lower surface sensitivity of XPS in this energy range. However, the observed increase of the Pd intensity and the stabilization of the measured Ni signal at high temperatures support our interpretation of observing the surface segregation.

The course of the Ni depletion depending on the Pd orientation is in good agreement with theoretical models for adatom surface diffusion on low index fcc surfaces, based on Monte Carlo simulations on Pd [112] as well as to those based on the embedded atom method calculated for Pt surfaces [113]. The exchange diffusion mechanism for the (100) orientation is taken into account. This mechanism is reported by Antczak and Ehrlich [114] and Oura et al. [115] to play an important role in surface diffusion for Pt, Ir and Ni and is predicted for Pd, too [113]. Regarding the low index surfaces, the lowest activation energy is reported for the (111)-surface, followed by the (100)-orientation and resulting in the highest value for (110) surface orientation. A variety of theoretical models and calculation schemes were compared, showing a uniform trend, but the

exact results for the activation energies differ in a wide range between 0.14 eV up to 1.35 eV [112] and between 7 meV and 4 eV [113]. The experimentally derived energies are found in the range of some ten meV.

The difference in the activation energy between the Pd(111) and Pd(110) orientation is less than a factor of two, compared with a factor of at least six for the theoretical calculations. The deviations may result from the fact that no segregation effects were included in the considered theoretical models, which may enforce the migration of Ni and lower the activation energies. The measured energies also indicate, that the energy difference for different orientations in the theoretical model may be overrated.

In summary, the direct observation of surface segregation of Ni adatoms on single crystalline Pd surfaces was shown. The in situ temperature dependent measurements of the composition of the first atomic layer have shown evidence for surface segregation effects related to crystal orientation. For all samples a strong tendency for Pd segregation was found, beginning at different activation temperatures T_0. The lowest activation temperature of T_0=172 °C was evaluated for Pd(111), followed by Pd(100) with T_0=261 °C. The highest activation temperature was found for Pd(110) with T_0=326 °C. This sequence is in good agreement with theoretical predictions for adatom diffusion on low index fcc surfaces and substantiates the model of Pd surface enrichment for Ni/Pd due to surface segregation for all Pd orientations. However, the corresponding activation energies are on average by a factor of ten lower than predicted by theoretical models considering single atom diffusion and the exchange diffusion mechanism. More sophisticated models including full coverage by 1 ML Ni of a Pd surface for the calculations of the temperature dependent surface kinetics are expected to improve the agreement between theory and experiment considerably.

7.5 Cyclic heating of 0.7 ML Ni/Pd

To examine the surface segregation process of Ni and the stability of the formed surface layer, a polycrystalline Pd substrate was covered with 0.7 ML of Ni. Subsequently, the sample was heated up to 200 °C for 1 hour and the time

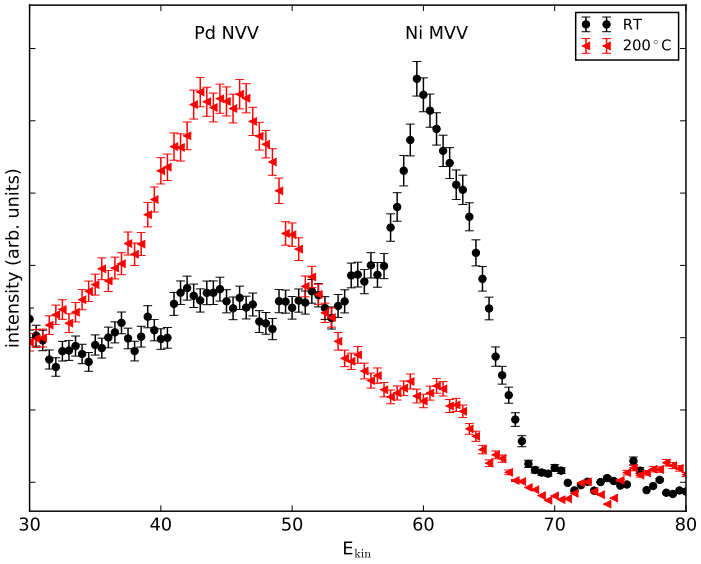

Figure 7.8: PAES spectra of 0.7 ML Ni/Pd recorded at room temperature and at 200 °C.

dependent evolution of the Ni and Pd intensity was recorded. The heating process was executed three times in total.

Beginning with the as-prepared sample, a distinct Ni signature with an Auger fraction of 0.73 and a less pronounced Pd peak is visible, see Figure 7.8. When heating the sample to 200 °C, the intensities reverse and the spectrum recorded at 200 °C is dominated by the Pd signature, showing an Auger intensity of 0.87. However, a small Ni signature can still be found. Heating is stopped after recording the PAES spectrum. As the sample is not cooled actively, the time for the cool down of the sample was evaluated by an exponential fit. Two time constants were found. A fast component with a time constant τ_1=10 min and a slow component with τ_2=60 min. The intensity of the fast component is four times higher compared with the slow one. From this, it can be calculated that the sample temperature has dropped to approximately 50 °C after one hour.

The time dependent evolution of the Auger intensity of Ni and Pd is shown in Figure 7.9. The Ni signal remains constant, whereas the Pd intensity decreases exponentially after the heating process. From theoretical calculations on the positron probability density at the sample surface, between 5 % and 20 % of the PAES signal can originate from the second atomic layer, depending on the

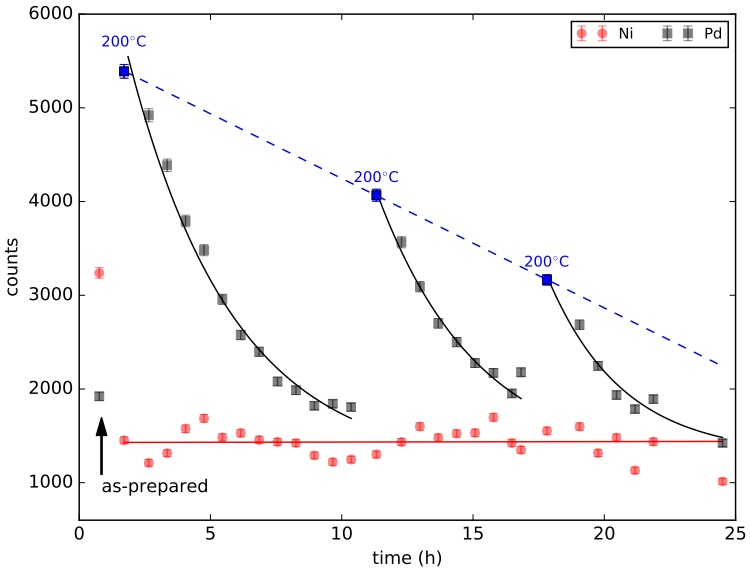

Figure 7.9: Time dependent PAES signal of Ni and Pd in three heating cycles to 200 °C (blue squares in Pd). Other data points are recorded at room temperature. The Ni signal appears to remain constant after the first heating, indicating a fast segregation process. The Pd signal shows an exponential decrease after each heating, which can be interpreted as the adsorption of rest gas, especially H, as it can be easily desorbed by heating. The decrease of the Pd signal at 200 °C may result from a progressive covering from the residual gas, which cannot be desobed thermally. It is represented by the dashed blue line.

surface structure and the elements [11]. The exponential decrease of the Pd signal can be seen as a consequence of rest gas interaction and the advancing coverage of the Pd surface. As the Ni count rate remains constant over time, it can be concluded, that the Ni atoms are stabilized in the subsurface layer and not affected by the rest gas. From this, it is concluded, that the Ni atoms initially present at the surface, migrate in a surface segregation process to the second atomic layer.

After several hours of observation, the sample was heated to 200 °C again. An increase of the Pd signal by 225 % compared to the previous spectrum was observed, whereas the Ni count rate was not effected by this process. This suggests the conclusion, that adsorbates were thermally desorbed from the Pd layer. Another heating cycle increased the Pd signal by 145 % compared to the previous spectrum without any detectably influence on Ni. However, the initial

value of the Pd intensity cannot be reached any more. This effect is attributed to C contamination. The accompanying XPS analysis shows an increase of the C content present at the surface. The C content measured at a sample temperature of 200 °C increased between the heating cycles from 5.1 % to 7.7 % and 9.2 %.

7.5.1 Comparison with Ni/Pt

Due to their isoelectronicity Pd and Pt are often compared regarding their behavior in surface processes. For this reason, the surface composition of the isoelectronic system Ni/Pt was studied with PAES. A polycrystalline Pt substrate was covered with 0.7 ML of Ni and heating cycles equivalent to those described for Ni/Pd in the previous section were executed. Beginning at room temperature with the as-prepared sample, the PAES spectrum shows a clear Ni signature with an Auger fraction of 0.77. Heating to 200 °C enhanced the Pt signature, leading to an Auger fraction of 0.37. Comparing the count rates of Ni and Pt, see Figure 7.10, Pt showes a significant increase to 146 % of the value at room temperature, whereas the Ni signal decreased. Over the course of time, the count rates of both elements show an exponential decrease, however, the decrease of Pt is faster. A further heating up of the sample increases the Pt signal to 138 % compared to the value previously obtained at room temperature and decreases exponentially afterwards. However, the initial count rate is not reached any more. Again, the Ni count rate is not affected in this heating process. This is in agreement with XPS results on pure Ni, evaluating the effect of thermal cleaning shown in Figure 3.10. No significant effect can be observed up to 200 °C.

Comparing the signal increase of Pd and Pt during heating to 200 °C, it turns out that Pd shows a more pronounced effect of thermal cleaning. As the base pressure of the chamber did not change during experiments as well as the rest gas composition, the almost identical time constants of the signal decrease and the behavior of Pd and Pt during heating indicate different rest gas interaction at the respective surface. The XPS data of both sample do not show significant differences in the amount of contaminates on the surface. However, Pd appears to profit more from the heating procedure. This result may be explained by the different desorption of H from Pd and Pt surfaces.

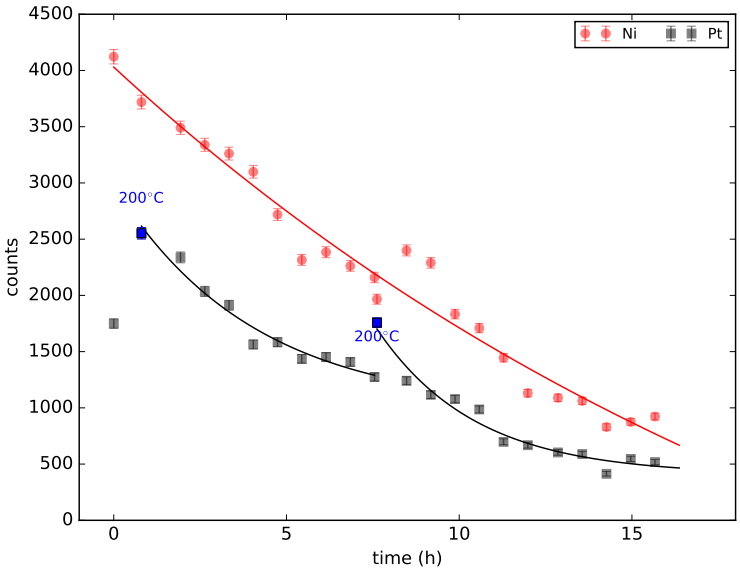

Figure 7.10: Time dependent PAES signal of Ni and Pt in two heating cycles to 200 °C. In contrast to Ni on Pd, the Ni signal follows the decreases of the Pt signal. This indicates that Ni is effected by the residual gas in the same way as Pt and therefore not covered by a Pt layer. Pt shows a moderate cleaning effect at elevated temperatures, which is less pronounced compared to Pd. For Ni no cleaning effect is observed at 200 °C.

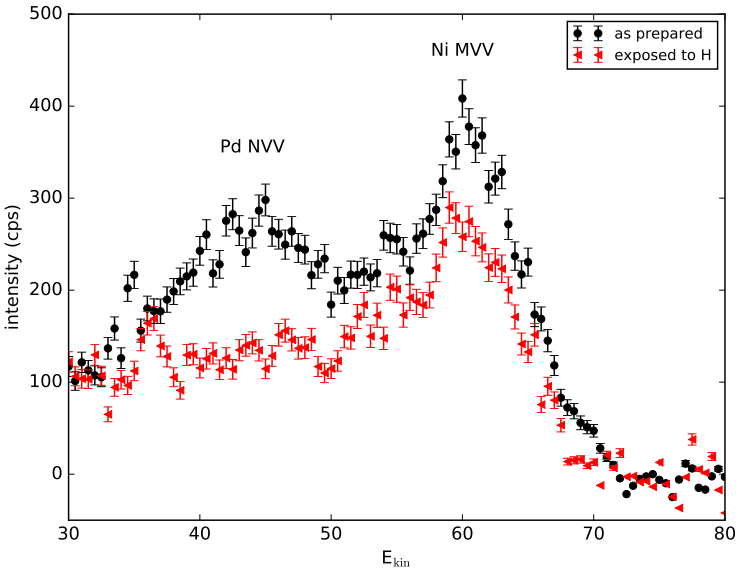

Figure 7.11: PAES spectra of 0.7 ML Ni/Pd before and after the exposure to H.

Theoretical calculations found the desorption energy for H to be lower for Pd compared to Pt [116]. However, this calculation relates to nanoparticles of Pt and Pd. Therefore, the effect is expected to be more pronounced for Pd than for Pt. The influence of H to a Ni/Pd surface was studied experimentally on a sample with a 0.7 ML Ni cover layer on polycrystalline Pd. The sample was exposed to H for 20 min at a H partial pressure of $1.0 \cdot 10^{-7}$ mbar. The spectra are shown in Figure 7.11. Comparing the count rate of Ni and Pd before and after H-exposition, a decrease of the Pd intensity of 50 % was detected, whereas the Ni singal decreased by only 25 %, although Ni covers the greater part of the surface. This suggests a high adsorption rate of Pd for H. In the complementary XPS data, this effect was not observable, as H cannot be detected directly. Even a detailed analysis of the band structure was not able to resolve the arising of a side peak unambiguously, indicating a H bonding. Therefore, PAES is particularly suitable to study the surface interaction with H, even if no Auger transition is possible in the H atom.

From the exponential decrease of the count rate of both elements, it is concluded that both elements are interacting with the rest gas, i.e. Ni and Pt are present at the surface during the whole time. From this data, in contrast

to Ni on Pd, no tendency for surface segregation can be derived. Theoretic predictions and experimental data on surface segregation of Ni atoms on a Pt surface show unambiguous results. Simple models based on the breaking of atomic bonds [90, 117, 118] and differences in the atom size [119] as well as density functional theory calculations [120] predict a strong tendency for surface segregation. However, no evidence was found for surface segregation in the experiment on a NiPt alloy [121]. For NiPt nano particles, a complex surface segregation depending on the crystallographic orientation was found with a Pt-rich frame along the edges and corners of the nano particles, whereas the Ni atoms are preferentially segregated in their 111-facet region [122]. Therefore, size dependent effects may play an important role for surface segregation. This effect can be studied by the investigation of thin layers of Ni and Pd on a MgO substrate, discussed in the next section.

7.6 Ni/Pd on MgO(001)

Surface segregation is a consequence of the minimization of the Gibb's free energy and therefore a complex interplay of various parameters such as surface structure, composition and temperature. Many segregation processes are well known at the larger scale, i.e. the interaction of one monolayer or non-interacting single atoms of an element located at the surface of another element with a bulk thickness of several hundred atomic layers can be predicted. For a surface the large volume of the bulk can act as a semi-infinite source or sink of atoms. For example, structural deformations such as lattice mismatch as a consequence of the migration of atoms can be spread widely over several layers. In contrast, at the nanoscale the bulk volume is limited. This leads to new phenomena, as the energy changes associated with changes in the bulk composition matter and a competition of surface and bulk energy terms arises. For this reason, size-dependent surface segregation and its impact on order-disorder phenomena and on catalytic activity was the object of many theoretical and experimental studies, e.g. [95, 123–125].

In the previous sections, the surface segregation of Ni on bulk Pd was studied. In the following, evaporated layers with a thickness of only 3 ML of Ni and Pd on a MgO substrate are studied, to evaluate the size-dependent effect on the

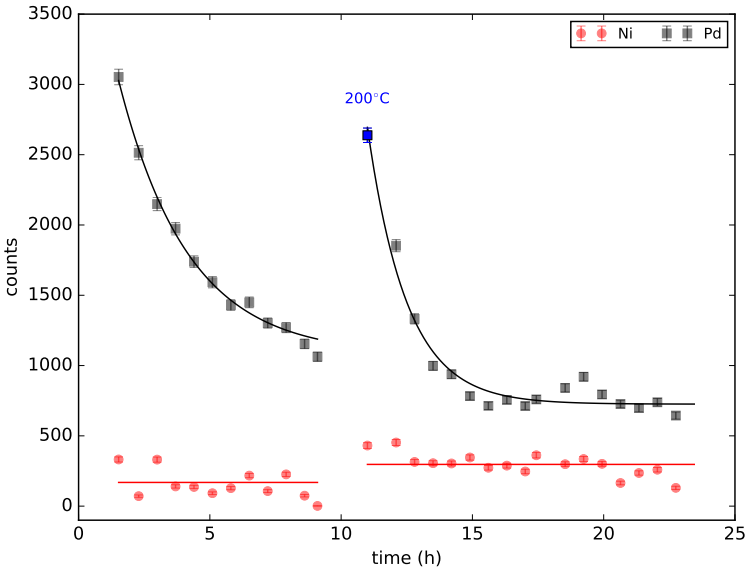

Figure 7.12: $Pd_{3\,ML}/Ni_{3\,ML}/MgO$: Layer system of 3 ML Ni covered with 3 ML Pd grown on MgO. The exponential decrease of Pd and the constant Ni intensity at room temperature and after heating to 200 °C indicate a stable Pd layer at the surface.

surface segregation of Ni/Pd. MgO is known to act as an inert substrate for metallic alloys and nanoparticles.

7.6.1 Ni/Pd layers on MgO

$Pd_{3\,ML}/Ni_{3\,ML}/MgO$ A MgO(001) substrate was evaporated with 3 ML of Ni and subsequently covered with 3 ML of Pd by electron beam evaporation. The recorded PAES spectrum is dominated by Pd with an Auger fraction of 0.96. The time-dependent evolution of the count rate of Ni and Pd is shown in Figure 7.12. Spectra were recorded at room temperature over a time range of 8h. The Ni signal remained stable at a low level, whereas the Pd signal decreased exponentially. As Pd is the outermost layer, this is attributed to residual gas coverage. As the Ni signal is constant, it is concluded, that Ni remains in the subsurface layers and is not affected by the residual gas. Subsequently, the sample was heated to 200 °C. The Pd signal increases to 250 % of the value at room temperature. However, it does not reach the initial value. In the XPS data, a moderate decrease of C can be detected at 200 °C. Thus, the increase of

the Pd signal is much more pronounced than it would be explained by the XPS data. Pd is known for its high sticking probability for H [126] and H cannot be detected in XPS. The decrease of the PAES signal due to an H overlayer after exposure to 1000 Langmuir was reported by Lee *et al.* [127]. Therefore, it is concluded that the increase in the Pd signal at 200 °C is dominated by the desorption of H from the Pd surface. After cooling down to room temperature, an exponential decrease of the Pd signal can be detected again, as H and rest gas is adsorbed again. The count rate of Ni is not influenced significantly by the heating process. A slight increase in intensity can be observed after heating. For Ni on bulk Pd, theoretic calculations predict the segregation of Ni to the second atomic layer. As the Ni atoms were covered by three monolayers of Pd in the preparation process, the increase and subsequent stabilization of the Ni signal may be interpreted as Ni enrichment of the subsurface layer, forced by the increase in temperature. The constant Ni signal with an Auger fraction of less than 0.1 and 0.25 before and after heating, respectively, as well as the exponential decrease of the Pd intensity as a consequence of rest gas interaction indicate a stable Pd layer at the surface. As described in the previous sections, the Pd surface layer is also the energetically favored configuration for Ni atoms on bulk Pd after surface segregation.

$Ni_{3\,ML}/Pd_{3\,ML}/MgO$ Another layered Ni/Pd system was grown on MgO with the same layer thickness of Ni and Pd but in reverse order. The PAES spectrum is dominated by the Ni signal with an Auger intensity of 0.88. At room temperature, an exponential decrease of the Ni intensity is observed, see Figure 7.13. As Ni is the covering layer, this can be attributed to an advancing contamination with the rest gas. To evaluate the Pd count rate correctly, the fraction of scattered Ni Auger electrons overlapping with the energy range where the Pd events are counted needs to be eliminated from the spectrum, as described in Section 5.2.1. This is particularly necessary in this case since the spectrum is dominated by the Ni Auger peak. The Pd intensity is found to be compatible with a constant fit at room temperature, indicating Ni to remain at the surface. This is in agreement with the results obtained from Ni on bulk Pd, showing a low time constant for surface segregation at room temperature.

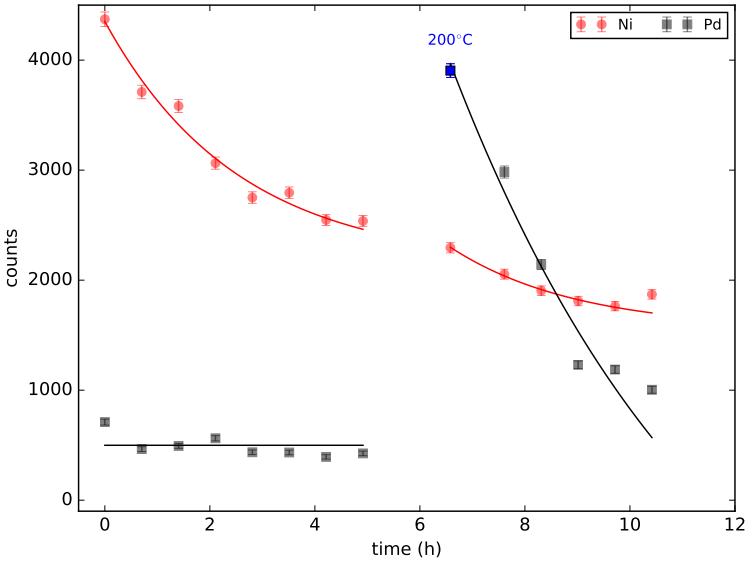

Figure 7.13: $Ni_{3\,ML}/Pd_{3\,ML}/MgO$: Layer system of 3 ML Pd covered with 3 ML Ni grown on MgO. The constant Pd intensity before heating to 200 °C and the exponential decrease afterwards indicate Pd to migrate from the subsurface to the surface.

However, when heating up the sample to 200 °C, the Pd Auger peak dominates the PAES spectrum with an Auger fraction of 0.7. In the subsequent evolution at room temperature, the Pd intensity shows an exponential decrease, as observed in the previously discussed results for the layered sample on MgO with reveres order. From this it is concluded that a rearrangement took place on the surface, so that Pd is now found in the outermost layer. Comparing the slope of the exponential decrease of Ni and Pd, a time constant of 2.5 h for Ni and 5.2 h for Pd can be evaluated. As the base pressure of the chamber as well as the composition of the rest gas has not changed, this could be an indication to different adsorption rates of the two elements, especially for hydrogen. This is in agreement with observation of a lower sticking probability for H on Ni compared to Pd [126]. In summary, experimental evidence for a surface segregation in thin layers of Ni and Pd on MgO was found, showing a stable arrangement of Pd atoms in the outermost layer.

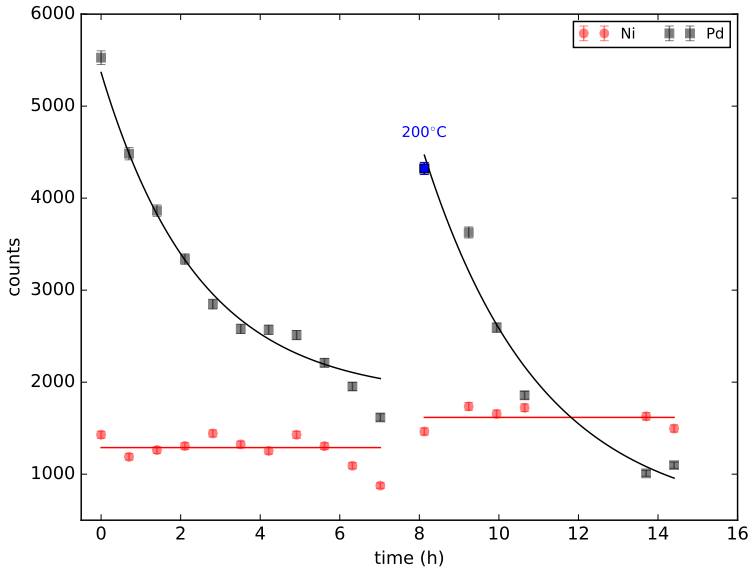

Figure 7.14: $(NiPd)_{6\,ML}/MgO$: Alloy of 6 ML NiPd on MgO substrate grown by simultaneous evaporation of Ni and Pd. The exponential decrease of the Pd signal before and after heating indicate a Pd layer at the surface due to segregation during growth.

7.6.2 NiPd alloy on MgO

As a consequence of the observation of the formation of a stable Pd surface layer in layered Ni/Pd samples grown on MgO, the composition of the surface layer should be studied, when both elements are evaporated onto the MgO surface at the same time. For this co-evaporation, two independent effusion cells were adjusted to the same evaporation rate for Ni and Pd of 6 Å/min. A total thickness of 6 ML was grown on the MgO substrate. Slight deviations from the set rate over time allow a composition of 45 at% Pd and 55 at% Ni to be calculated. The following PAES spectrum shows a clearly pronounced Pd peak with an Auger fraction of 0.84 and only a small Ni signature. Over time, an exponential decrease of Pd can be observed, whereas Ni remains at a constant level at room temperature, see Figure 7.14. This result indicates that the arrangement of the Pd atoms at the surface already took place during the evaporation process. This phenomenon was observed in epitaxial growth for several element combinations such as Si/Ge [128], $La_{0.7}Sr_{0.3}MnO_3$ [129] or Sb/Si [130].

During heating the sample to 200 °C, the Pd signal shows an increase by 270 % compared to the previous spectrum. However, the initial count rate of the as-prepared specimen is not reached. This can be attributed to a desorption of H as the XPS spectra show a moderate reduction of C after the heating process, which is still above the initial value. Subsequently, an exponential decrease of the Pd intensity can be observed, indicating Pd to adsorb rest gas again. The Ni signal shows only a low increase in count rate as a result of the heating. This is in agreement with the XPS results obtained on stepwise thermal cleaning of pure Ni presented in Figure 3.10. The contaminations C and O were mostly dissolved at temperatures above 200 °C.

In summary, for layered systems of Ni and Pd on MgO, evidence for surface segregation of Ni atoms to the subsurface layer at 200 °C and the formation of a stable Pd surface layer were found. This result is in accordance with the results obtained for Ni cover layers on a bulk Pd substrate. However, the co-evaporation of Ni and Pd on MgO appears to show surface segregation already during growth. The exposure of a Ni/Pd surface to H showed a clear effect to the respective PAES intensities, which is not detectable with XPS. Hence, evidence for element specific surface interaction can be derived from the PAES spectra.

Chapter 8

Summary and outlook

In this work, the successful PAES studies on surface segregation of Fe/Pt, Ni/Pt and Ni/Pd are presented. The surface spectrometer at the world's most intense positron source enables the precise preparation of coating layers on metal and insulator substrates as well as their investigations with a variety of surface analysis techniques. The surface topography can be studied with STM and the elemental composition can be investigated with outstanding surface sensitivity using PAES. Furthermore, element information of subsurface layers can be obtained by XAES, EAES and XPS. Due to its high chemical specificity, XPS analysis is an excellent complementary technique to study surface contamination.

An unprecedented measurement time of only 230 s for a PAES spectrum was achieved, allowing time resolved PAES studies. The high Auger peak intensity and energy resolution of the setup enables the separation of Auger peaks with an energy difference of only 2.2 eV, allowing the investigation a variety compounds.

The excellent surface sensitivity of PAES was demonstrated experimentally on submonolayer Ni coverage on a Pd substrate. A Ni cover layer with a thickness of only 0.1 ML was clearly detectable with PAES and a 1 ML cover layer of Ni dominated the spectrum with an Auger intensity of more than 90 %.

The time dependent PAES investigation of Ni adatoms on polycrystalline Pd gave a first evidence for surface segregation at room temperature. In an in-situ temperature dependent study, the surface segregation of Ni adatoms on Pd substrates was observed for the first time. Different activation energies

were found depending on the crystallographic orientation of the Pd substrate. In contrast to Ni/Pd, the system Ni/Pt was determined to show no surface segregation. Apart from the surface segregation of Ni adatoms on a bulk Pd substrate, surface segregation of thin layers of Ni and Pd on a MgO substrate were studied. Again, a clear tendency for surface segregation and the stability of Pd surface layer is observed. In addition, evidence for surface segregation already during growth was found for an alloy of Ni and Pd on MgO.

A clear and element specific effect to the PAES signal was observed as a consequence of H exposure of a Ni/Pd surface, which was not observable with XPS. Hence, PAES can provide unique information for the investigation of catalysts, e.g. to study the poisoning of catalyst due to contact with S or the accretion of CO as well as for the elaboration of in-situ recovery procedures.

When developing novel catalysts, PAES can be used for both, the investigation of the elemental composition of the surface layer as well as for studies on the H-surface interaction. Furthermore, poisoning and recovery procedures for catalysts due to contact with reactive gases may be studied with PAES in situ, providing unique insight, which is not accessible for conventional surface analysis techniques.

Appendix A

Calculated core annihilation probabilities

system	core annihilation probability (%)							
	substrate				adsorbate			
clean Cu(100)	3s	0.83	3p	3.02				
Cu(100)+C	3s	0.44	3p	1.62	1s	0.14		
Cu(100)+N	3s	0.39	3p	1.41	1s	0.21		
Cu(100)+O	3s	0.48	3p	1.75	1s	0.10		
Cu(100)+S	3s	0.20	3p	0.74	2s	0.12	2p	0.31

Table A.1: Annihilation probabilities with substrate and adsorbate core electrons for adsorbate-covered Cu(100) surfaces. [11]

system	core annihilation probability (%)		
	Cu 3s	Cu 3p	O 1s
Cu(100)	1.766	6.990	
Cu(100)+O (1/8 ML)	1.203	4.806	0.030
Cu(100)+O (1/4 ML)	1.043	4.172	0.067
Cu(100)+O (1/2 ML)	0.748	2.991	0.142
Cu(100)+O (1 ML)	0.398	1.595	0.227
CuO(100)	0.566	2.227	0.323
Cu_2O(100)	1.012	3.981	0.167
Cu_2O(100)+O (1/2 ML)	0.799	3.144	0.208

Table A.2: Positron annihilation probabilities with relevant core electrons for a clean Cu(100) surface, Cu(100) covered with adsorbed oxygen and for (100) surface of CuO, Cu_2O and Cu_2O with half monolayer of adsorbed oxygen. [42]

	level 1s	2s	2p	3s	3p	3d	4s	4p	4d	4f	5s	5d
Li	5.42											
Be	4.37											
Na	0.049	2.11	6.86									
Mg	0.032	1.56	4.87									
Al	0.021	1.18	3.53									
K		0.028	0.069	1.27	5.25							
Ti		0.045	0.11	2.31	8.70							
V		0.053	0.12	2.76	10.21							
Cr		0.059	0.14	3.07	11.28							
Fe		0.034	0.076	1.98	7.20							
Ni		0.034	0.075	2.07	7.41							
Cu		0.027	0.058	1.66	5.93							
Zn		0.018	0.038	1.18	4.23							
Rb				0.021	0.072	0.17	1.05	5.31				
Zr				0.039	0.13	0.26	2.05	8.71				
Nb				0.042	0.14	0.26	2.18	9.07				
Mo				0.040	0.13	0.24	2.12	8.74				
Pd				0.026	0.080	0.13	1.51	6.07				
Ag				0.022	0.069	0.11	1.38	5.53				
Cd				0.015	0.047	0.073	1.01	4.06				
Cs							0.020	0.078	0.26		0.93	4.41
Ce							0.052	0.19	0.18		1.48	5.60
Gd							0.039	0.14	0.39		2.03	9.01
Ta							0.034	0.12	0.30	1.82	1.94	8.43
W							0.036	0.13	0.31	1.64	2.05	8.80
Pt							0.026	0.089	0.21	0.75	1.56	6.63
Au							0.021	0.071	0.16	0.56	1.32	5.58
Tl							0.009	0.031	0.071	0.22	0.68	2.89
Pb							0.005	0.018	0.039	0.12	0.40	1.72

Table A.3: Calculated core annihilation probabilities in % for bulk materials. [11]

Appendix B

Experimental parameters

Auger electrostatic lens system

lens number	potential
1	-1 V
2	-1 V
3	-100 V
4	-250 V
5	-30 V
6	-20 V
7.1	+9.6 V
7.2	+9.3 V
7.3	+9.2 V
7.4	+9.1 V

Table B.1: Lens parameters for the 20 eV re-moderated positron beam.

List of Publications

2017 S. Zimnik, M. Dickmann and C. Hugenschmidt. In-situ observation of temperature-dependent segregation of Ni adatoms on oriented Pd surfaces. *submitted to Surface Science*, available in arXiv

2017 S. Zimnik, M. Hackenberg and C. Hugenschmidt. Iterative fitting method for the evaluation and quantification of PAES spectra. *Journal of Physics: Conf. Series*, 791 (2017) 012034

2016 S. Zimnik, C. Piochacz, S. Vohburger and C. Hugenschmidt. Time-dependent investigation of sub-monolayers of Ni and Pd using Positron-annihilation induced Auger Electron Spectroscopy and XPS. *Surface Science*. 643 (2016) 178 - 182

2016 S. Zimnik, C. Piochacz, S. Vohburger and C. Hugenschmidt. Comparative Study of Time-dependent PAES and XPS on a Ni/Pd Surface. *Defect and Diffusion Forum*, 373 (2016) 313 - 316

2016 N. Grill, C. Piochacz, S. Zimnik, and C. Hugenschmidt. Novel pulsed particle accelerator for energy dependent positron re-emission experiments. *Review of Scientific Instruments*, 87 (2016) 053304

2014 C. Hugenschmidt, H. Ceeh, T. Gigl, F. Lippert, C. Piochacz, M. Reiner, K. Schreckenbach, S. Vohburger, J. Weber and S. Zimnik. Positron Beam Characteristics at NEPOMUC Upgrade. *Journal of Physics: Conf. Series*. 505 (2014) 012029

2014 S. Zimnik, F. Lippert and C. Hugenschmidt. Upgrade of the surface spectrometer at NEPOMUC for PAES, XPS and STM investigations. *Journal of Physics: Conf. Series*. 505 (2014) 012003

2013 C. Hugenschmidt, H. Ceeh, T. Gigl, F. Lippert, C. Piochacz, P. Pikart, M. Reiner, J. Weber, S. Zimnik. The upgrade of the neutron induced positron source NEPOMUC. *Journal of Physics: Conf. Series*. 443 (2013) 2079

Parts of the present thesis have been published in the above stated references.

Bibliography

[1] P. A. M. Dirac. A theory of electrons and protons. *Proc. R. Soc. A*, 126(801):360–365, 1930.

[2] Carl D. Anderson. The positive electron. *Phys. Rev.*, 43:491–494, 1933.

[3] P. J. Mohr, B. N. Taylor, and D. B. Newell. Codata recommended values of the fundamental physical constants: 2006. *Rev. Mod. Phys.*, 80(2):633, 2008.

[4] P.J. Schultz and K.G. Lynn. Interaction of positron beams with surfaces, thin films, and interfaces. *Rev. Mod. Phys.*, 60(3):701–779, 1988.

[5] M. Reiner, A. Bauer, M. Leitner, T. Gigl, W. Anwand, M. Butterling, A. Wagner, P. Kudejova, C. Pfleiderer, and C. Hugenschmidt. Positron spectroscopy of point defects in the skyrmion-lattice compound mnsi. *Scientific Reports*, 6:29109, 2016.

[6] M.J. Puska and R.M. Nieminen. Theory of positrons in solids and on solid surfaces. *Rev. Mod. Phys.*, 66(3):841–897, 1994.

[7] P. Coleman. *Positron beams and their applications*. World Scientific, 2000.

[8] A. Dupasquier, A.P. Mills, and Società Italiana di Fisica. *Positron Spectroscopy of Solids*. Proceedings of the International School of Physics "Enrico Fermi". IOS Press, Ohmsha, 1995.

[9] A. Kawasuso and S. Okada. Reflection high energy positron diffraction from a Si(111) surface. *Phys. Rev. Lett.*, 81(13):2695–2698, 1998.

[10] T. Hyodo, Y. Fukaya, M. Maekawa, I. Mochizuki, K. Wada, T. Shidara, A. Ichimiya, and A. Kawasuso. Total reflection high-energy positron diffraction (TRHEPD). *J. Phys.: Conf. Ser.*, 505(1):012001, 2014.

[11] K. O. Jensen and A. Weiss. Theoretical study of the application of positron-induced auger-electron spectroscopy. *Phys. Rev. B*, 41:3928–3936, 1990.

[12] K. A. Ritley, K. G. Lynn, V. J. Ghosh, D. O. Welch, and M. McKeown. Low-energy contributions to positron implantation. *J. Appl. Phys.*, 74(5):3479–3496, 1993.

[13] A. F. Makhov. The penetration of electrons into solids. *Sov. Phys. Solid State 2*, 1934, 1961.

[14] A. H. Weiss. Positron annihilation induced auger electron spectroscopy. *Solid State Phenomena*, 28-29:317–340, 1992.

[15] R. M. Nieminen and M. J. Puska. Positron Surface States on Clean and Oxidized Al and in Surface Vacancies. *Phys. Rev. Lett.*, 50:281–284, 1983.

[16] C. Hugenschmidt. Positrons in surface physics. *Surf. Sci. Rep.*, 71(4):547 – 594, 2016.

[17] A.H. Weiss, G. Yang, J.H. Kim, A. Nangia, and N.G. Fazleev. Application of positron annihilation induced auger electron spectroscopy to the study of surface chemistry. *J. Radioanal. Nucl. Chem.*, 210(2):423–433, 1996.

[18] O.M. Lovvik. Surface segregation in palladium based alloys from density-functional calculations. *Surf. Sci.*, 583:100 – 106, 2005.

[19] J. Mayer, C. Hugenschmidt, and K. Schreckenbach. Direct observation of the surface segregation of Cu in Pd by time-resolved positron-annihilation-induced Auger electron spectroscopy. *Phys. Rev. Lett.*, 105(20):207401, 2010.

[20] L. Meitner. Über die β-Strahl-Spektra und ihren Zusammenhang mit der γ-Strahlung. *Zeitschrift für Physik A Hadrons and Nuclei*, 11:35–54, 1922.

[21] P. Auger. Sur l'effet photoélectrique composé. *Journal de Physique et Le Radium*, 6:205–208, 1925.

[22] D. Coster and R. De L. Kronig. New type of Auger effect and its influence on the X-ray spectrum. *Physica*, 2(1-12):13 – 24, 1935.

[23] M.F. Chung and L.H. Jenkins. Auger electron energies of the outer shell electrons. *Surf. Sci.*, 22(2):479 – 485, 1970.

[24] M. O. Krause. Atomic radiative and radiationless yields for K and L shells. *J. Phys. Chem. Ref. Data*, 8(2):307–327, 1979.

[25] A.C. Thompson, D. Vaughan, Center for X-ray Optics (Lawrence Berkeley National Laboratory), Center for X-ray optics, advanced light source, and Lawrence Berkeley National Laboratory. Advanced Light Source. *X-ray Data Booklet*. Lawrence Berkeley Laboratory, 2009.

[26] L. E. Davis, N. C. MacDonald, P. W. Palmberg, G. E. Riach, and R. E. Weber. *Handbook of Auger Electron Spectroscopy*. Perkin-Elmer Corp., 1978.

[27] J.H. Scofield. Hartree-slater subshell photoionization cross-sections at 1254 and 1487 ev. *J. Electron. Spectrosc. Relat. Phenom.*, 8(2):129 – 137, 1976.

[28] J.C. Vickerman and I. Gilmore. *Surface Analysis: The Principal Techniques*. Wiley, 2011.

[29] D. Briggs and M. P. Seah. *Practical Surface Analysis*. Wiley Chichester UK, 1990.

[30] M. P. Seah and W. A. Dench. Quantitative electron spectroscopy of surfaces: A standard data base for electron inelastic mean free paths in solids. *Surf. Interface Anal.*, 1(1):2–11, 1979.

[31] A. Weiss, R. Mayer, M. Jibaly, C. Lei, D. Mehl, and K. G. Lynn. Auger-electron emission resulting from the annihilation of core electrons with low-energy positrons. *Phys. Rev. Lett.*, 61(19):2245–2248, 1988.

[32] P.W. Palmberg, G.E. Riach, and R.E. Weber. *Handbook of Auger Electron Spectroscopy Data*. Physical Electronics Industries, 1972.

[33] N. G. Fazleev, J. L. Fry, and A. H. Weiss. Surface states and annihilation characteristics of positrons trapped at the (100) and (111) surfaces of silicon. *Phys. Rev. B*, 70(16):165309, 2004.

[34] A.R. Koymen, K.H. Lee, G. Yang, H. Zhou, and Alex H. Weiss. Temperature dependent top layer composition of Pd on Cu(100). *Mat. Sci. For.*, 105-110:1411–1414, 1992.

[35] A. R. Koymen, K. H. Lee, G. Yang, K. O. Jensen, and A. H. Weiss. Temperature-dependent top-layer composition of ultrathin Pd films on Cu(100). *Phys. Rev. B*, 48(3):2020–2023, 1993.

[36] K. H. Lee, Gimo Yang, A. R. Koymen, K. O. Jensen, and A. H. Weiss. Positron annihilation induced Auger electron spectroscopy studies of submonolayer Au on Cu(100): Direct evidence for positron localization at sites containing Au atoms. *Phys. Rev. Lett.*, 72(12):1866–1869, 1994.

[37] D. Mehl, A. R. Köymen, K. O. Jensen, F. Gotwald, and A. Weiss. Sensitivity of positron-annihilation-induced Auger-electron spectroscopy to the top surface layer. *Phys. Rev. B*, 41(1):799–802, 1990.

[38] G. Yang, J.H. Kim, S. Yang, and A.H. Weiss. Adsorption site identification for oxygen molecules on ausi(100) by positron annihilation induced auger electron spectroscopy(paes). *Appl. Surf. Sci.*, 85:77 – 81, 1995.

[39] C. Hugenschmidt, J. Mayer, and K. Schreckenbach. Surface investigation of Si(100), Cu, Cu on Si(100), and Au on Cu with positron annihilation induced Auger-electron spectroscopy. *Surf. Sci.*, 601:2459– 2466, 2007.

[40] J. G. Zhu, M. P. Nadesalingam, A. H. Weiss, and M. Tao. Stability of Se passivation layers on Si(001) surfaces characterized by time-of-flight positron annihilation induced Auger electron spectroscopy. *J. Appl. Phys.*, 97:103510, 2005.

[41] T. Ohdaira, R. Suzukia, Y. Kobayashia, T. Akahaneb, and L. Daic. Surface analysis of a well-aligned carbon nanotube film positron-annihilation induced Auger-electron spectroscopy. *Appl. Surf. Sci.*, 194:291–295, 2002.

[42] N.G. Fazleev, M.P. Nadesalingam, W. Maddox, S. Mukherjee, K. Rajeshwar, and A.H. Weiss. Oxidation and thermal reduction of the Cu(100) surface as studied using positron annihilation induced Auger electron spectroscopy (PAES). *Surf. Sci.*, 604(1):32–37, 2010.

[43] J. H. Kim, G. Yang, and A. H. Weiss. Study of the adsorption of hydrogen and oxygen on Si(100) using positron-annihilation induced Auger electron spectroscopy (PAES). *Surf. Sci.*, 396(1–3):388–393, 1998.

[44] J. Mayer, C. Hugenschmidt, and K. Schreckenbach. High resolution positron annihilation induced Auger electron spectroscopy of the Cu $M_{2,3}$VV-transition and of Cu sub-monolayers on Pd and Fe. *Surf. Sci.*, 604:1772–1777, 2010.

[45] C. Hugenschmidt, J. Mayer, and K. Schreckenbach. High-resolution Auger-electron spectroscopy induced by positron annihilation on Fe, Ni, Cu, Zn, Pd, and Au. *J. Phys.: Conf. Ser.*, 225(1):012015, 2010.

[46] B. Straßer, C. Hugenschmidt, and K. Schreckenbach. Investigation of the annealed copper surface by positron annihilation induced Auger electron spectroscopy. *Radiat. Phys. Chem*, 68(3-4):627 – 629, 2003.

[47] C. Hugenschmidt, M. Stadlbauer, B. Straßer, and K. Schreckenbach. First positron experiments at NEPOMUC. *Appl. Surf. Sci.*, 252:3098–3105, 2006.

[48] C. Hugenschmidt, G. Dollinger, W. Egger, G. Kögel, B. Löwe, J. Mayer, P. Pikart, C. Piochacz, R. Repper, K. Schreckenbach, P. Sperr, and M. Stadlbauer. Surface and bulk investigations at the high intensity positron beam facility NEPOMUC. *Appl. Surf. Sci.*, 255(1):29–32, 2008.

[49] C. Hugenschmidt, H. Ceeh, T. Gigl, F. Lippert, C. Piochacz, M. Reiner, K. Schreckenbach, S. Vohburger, J. Weber, and S. Zimnik. Positron beam characteristics at nepomuc upgrade. *J. Phys.: Conf. Ser.*, 505(1):012029, 2014.

[50] J. Mayer, K. Schreckenbach, and C. Hugenschmidt. Recent development of the PAES set up at NEPOMUC. *Phys. Stat. Sol.*, 11:2468– 2470, 2009.

[51] S. Mukherjee, K. Shastry, C. V. Anto, P. V. Joglekar, M. P. Nadesalingam, S. Xie, N. Jiang, and A. H. Weiss. Time of flight spectrometer for background-free positron annihilation induced Auger electron spectroscopy. *Rev. Sci. Instrum.*, 87(3):035114, 2016.

[52] S. Zimnik, C. Piochacz, S. Vohburger, and C. Hugenschmidt. Time-dependent investigation of sub-monolayers of Ni on Pd using Positron-annihilation induced Auger Electron Spectroscopy and XPS. *Surf. Sci.*, 643:178 – 182, 2016.

[53] A. Einstein. Über einen die Erzeugung und Verwandlung des Lichtes betreffenden heuristischen Gesichtspunkt. *Annalen der Physik*, 322(6):132–148, 1905.

[54] N. Stojilovic. Why Can't We See Hydrogen in X-ray Photoelectron Spectroscopy? *J. Chem. Educ.*, 89(10):1331–1332, 2012.

[55] W. Eberhardt, Steven G. Louie, and E. W. Plummer. Interaction of hydrogen with a pd(111) surface. *Phys. Rev. B*, 28:465–477, 1983.

[56] National Institute of Standards and Technology. NIST X-ray Photoelectron Spectroscopy Database 20, Version 4.1, 2012.

[57] D. Briggs and J. T. Grant. *Surface analysis by Auger and X-ray photoelectron spectroscopy.* IM Publications Chichester, UK, 2003.

[58] J. B. Clegg. Quantitative measurement of impurities in GaAs layers by secondary ion mass spectrometry. *Surf. Interface Anal.*, 2(3):91–95, 1980.

[59] L. E. Lapides. Quantitative analysis of impurities in HgCdTe using secondary ion mass spectrometry. *Surf. Interface Anal.*, 7(5):211–216, 1985.

[60] F. Shoji, K. Kashihara, K. Oura, and T. Hanawa. Surface hydrogen detection by low energy 4He+ ion scattering spectroscopy. *Surf. Sci. Lett.*, 220(2):L719 – L725, 1989.

[61] B. Straßer. *Aufbau einer Anlage zur positroneninduzierten Auger-Elektronenspektroskopie.* PhD thesis, Lehrstuhl für Experimentalphysik E21, Technische Universität München, 2002.

[62] INTERNATIONAL ATOMIC ENERGY AGENCY. *Database of Prompt Gamma Rays from Slow Neutron Capture for Elemental Analysis.* INTERNATIONAL ATOMIC ENERGY AGENCY, Vienna, 2007.

[63] C. Hugenschmidt, G. Kögel, R. Repper, K. Schreckenbach, P. Sperr, and W. Triftshäuser. First platinum moderated positron beam based on neutron capture. *Nucl. Instr. Meth. Phys. Res. B: Beam Interactions with Materials and Atoms*, 198(3-4):220 – 229, 2002.

[64] C. Hugenschmidt, C. Piochacz, M. Reiner, and K. Schreckenbach. The NEPOMUC upgrade and advanced positron beam experiments. *New J. Phys.*, 14(5):055027, 2012.

[65] S. Zimnik, F. Lippert, and C. Hugenschmidt. Upgrade of the surface spectrometer at NEPOMUC for PAES, XPS and STM investigations. *J. Phys.: Conf. Ser.*, 505(1):012003, 2014.

[66] Sycon Instruments Inc. *Sycon Instruments STM-100/MF Thickness/Rate Monitor Users Manual Rev. G.* 6757 Kinne Street, East Syracuse, New York, 13057, USA, September 1997.

[67] N. Grill, C. Piochacz, S. Zimnik, and C. Hugenschmidt. Novel pulsed particle accelerator for energy dependent positron re-emission experiments. *Rev. Sci. Instrum.*, 87(5), 2016.

[68] G. Fletcher, J. L. Fry, and P. C. Pattnaik. Work functions and effective masses of positrons in metals. *Phys. Rev. B*, 27(7):3987–3991, 1983.

[69] G. Binnig and H. Rohrer. Scanning tunneling microscopy. *Helv. Phys. Acta.*, 55:726–735, 1982.

[70] G. Binnig, H. Rohrer, Ch. Gerber, and E. Weibel. 7x7 Reconstruction on Si(111) Resolved in Real Space. *Phys. Rev. Lett.*, 50:120–123, 1983.

[71] J.A. Stroscio and W.J. Kaiser. *Scanning Tunneling Microscopy.* Methods of Experimental Physics. Elsevier Science, 1993.

[72] J. Bardeen. Tunnelling from a many-particle point of view. *Phys. Rev. Lett.*, 6:57–59, 1961.

[73] A. Selloni, P. Carnevali, E. Tosatti, and C. D. Chen. Voltage-dependent scanning-tunneling microscopy of a crystal surface: Graphite. *Phys. Rev. B*, 31:2602–2605, 1985.

[74] SPECS Surface Nano Analysis GmbH. Manual for Phoibos Hemispherical Energy Analyzer, Version 4.0, 2012.

[75] J. Cazes. *Analytical Instrumentation Handbook, Third Edition.* CRC Press, 2004.

[76] R. F. Reilman, A. Msezane, and S. T. Manson. Relative intensities in photoelectron spectroscopy of atoms and molecules. *J. Electron. Spectrosc. Relat. Phenom.*, 8(5):389 – 394, 1976.

[77] G. Beamson and D. Briggs. *High Resolution XPS of Organic Polymers: The Scienta ESCA300 Database.* Wiley, 1992.

[78] N. Fairley and Casa Software Ltd. *CasaXPS Manual 2.3.15: CasaXPX Processing Software for XPS Spectra.* Casa Software Limited, 2009.

[79] D. A. Shirley. High-Resolution X-Ray Photoemission Spectrum of the Valence Bands of Gold. *Phys. Rev. B*, 5:4709–4714, 1972.

[80] M. P. Seah. The quantitative analysis of surfaces by XPS: A review. *Surf. Interface Anal.*, 2(6):222–239, 1980.

[81] H.J. Mathieu and D. Landolt. Quantitative auger electron spectroscopy analysis of Ag-Pd and Ni-Pd alloys. *Surf. Sci.*, 53(1):228 – 240, 1975.

[82] S. Zimnik, M. Hackenberg, and C. Hugenschmidt. Iterative fitting method for the evaluation and quantification of PAES spectra. *J. Phys.: Conf. Ser.*, 791(1):012034, 2017.

[83] D. Weller, A. Moser, L. Folks, M. E. Best, Wen Lee, M. F. Toney, M. Schwickert, J. U. Thiele, and M. F. Doerner. High Ku materials approach to 100 Gbits/in2. *IEEE Trans. Magn.*, 36(1):10–15, 2000.

[84] L. Han, U. Wiedwald, B. Kuerbanjiang, and P. Ziemann. Fe oxidation versus Pt segregation in FePt nanoparticles and thin films. *Nanotechnology*, 20(28):285706, 2009.

[85] R. V. Chepulskii and S. Curtarolo. First principles study of Ag, Au, and Cu surface segregation in FePt-L10. *Appl. Phys. Lett.*, 97(22):221908, 2010.

[86] F. Iskandar, H. M. Lee, T. T., T. Iwaki, and K. Okuyama. Fabrication of L10 FePtAg nanoparticles and a study of the effect of Ag during the annealing process. *J. Magn. Magn. Mater.*, 305(2):514 – 519, 2006.

[87] M. Respaud, J. M. Broto, H. Rakoto, A. R. Fert, L. Thomas, B. Barbara, M. Verelst, E. Snoeck, P. Lecante, A. Mosset, J. Osuna, T. Ould Ely, C. Amiens, and B. Chaudret. Surface effects on the magnetic properties of ultrafine cobalt particles. *Phys. Rev. B*, 57:2925–2935, 1998.

[88] J. C. Hamilton. Prediction of surface segregation in binary alloys using bulk alloy variables. *Phys. Rev. Lett.*, 42:989–992, 1979.

[89] D. Tomanek, S. Mukherjee, V. Kumar, and K.H. Bennemann. Calculation of chemisorption and absorption induced surface segregation. *Surf. Sci.*, 114(1):11 – 22, 1982.

[90] J.J. Burton, E. Hyman, and D.G. Fedak. Surface segregation in alloys. *J. Catal.*, 37(1):106 – 113, 1975.

[91] J. J. Burton and E. S. Machlin. Prediction of segregation to alloy surfaces from bulk phase diagrams. *Phys. Rev. Lett.*, 37:1433–1436, 1976.

[92] M. E. Gruner. Antiferromagnetism and segregation in cuboctahedral fept nanoparticles. *J. Phys. D: Appl. Phys.*, 41(13):134015, 2008.

[93] G. Bozzolo, R. A. Lukaszew, and J. E. Garces. Atomistic modeling of surface alloy ordering and segregation in the Fe-Pt system. *Appl. Phys. Lett.*, 88(1):011915, 2006.

[94] G. E. Ramirez-Caballero, Y. Ma, R. Callejas-Tovar, and P. B. Balbuena. Surface segregation and stability of core-shell alloy catalysts for oxygen reduction in acid medium. *Phys. Chem. Chem. Phys.*, 12:2209–2218, 2010.

[95] M. Müller and K. Albe. Lattice monte carlo simulations of fept nanoparticles: Influence of size, composition, and surface segregation on order-disorder phenomena. *Phys. Rev. B*, 72:094203, 2005.

[96] P. Beccat, Y. Gauthier, R. Baudoing-Savois, and J.C. Bertolni. Monotonous concentration profile and reconstruction at Pt80Fe20(111): LEED study of a catalyst. *Surf. Sci.*, 238(1):105 – 118, 1990.

[97] J. Honolka, T. Y. Lee, K. Kuhnke, A. Enders, R. Skomski, S. Bornemann, S. Mankovsky, J. Minár, J. Staunton, H. Ebert, M. Hessler, K. Fauth, G. Schütz, A. Buchsbaum, M. Schmid, P. Varga, and K. Kern. Magnetism of FePt Surface Alloys. *Phys. Rev. Lett.*, 102:067207, 2009.

[98] L. Giordano, M. Lewandowski, I. M. N. Groot, Y.-N. Sun, J. Goniakowski, C. Noguera, S. Shaikhutdinov, G. Pacchioni, and H.-J. Freund. Oxygen-Induced Transformations of an FeO(111) Film on Pt(111): A Combined DFT and STM Study. *J. Phys. Chem. C*, 114(49):21504–21509, 2010.

[99] A. P. Mills. Positronium formation at surfaces. *Phys. Rev. Lett.*, 41(26):1828–1831, 1978.

[100] J.-P. Candy, P. Fouilloux, and A. J. Renouprez. Hydrogen adsorption on platinum catalysts. quantitative determination of the various species population. *J. Chem. Soc., Faraday Trans. 1*, 76:616–629, 1980.

[101] H. Adkins and H. I. Cramer. The use of nickel as a catalyst for hydrogenation. *JACS*, 52 (11):4349–4358, 1930.

[102] M. Raney. Method of producing finely-divided nickel. US Patent 1628190, may 1927.

[103] J. A. D del Rosario, J. D Ocon, H. Jeon, Y. Yi, J. K. Lee, and J. Lee. Enhancing role of nickel in the nickel–palladium bilayer for electrocatalytic oxidation of ethanol in alkaline media. *J. Phys. Chem. C*, 118(39):22473–22478, 2014.

[104] S. M. Foiles, M. I. Baskes, and M. S. Daw. Embedded-atom-method functions for the fcc metals Cu, Ag, Au, Ni, Pd, Pt, and their alloys. *Phys. Rev. B*, 33(12):7983–7991, 1986.

[105] G. Bozzolo, J. E. Garces, R. D. Noebe, P. Abel, and H. O. Mosca. Atomistic modeling of surface and bulk properties of Cu, Pd and the Cu-Pd system. *Progr. Surf. Sci.*, 73(4-8):79 – 116, 2003.

[106] D.A. Mervyn, R.J. Baird, and P. Wynblatt. Surface segregation in a Ni-1 at% Pd alloy. *Surf. Sci.*, 82(1):79 – 92, 1979.

[107] G.N. Derry, C.B. McVey, and P.J. Rous. The surface structure and segregation profile of Ni50Pd50(100): a dynamical LEED study. *Surf. Sci.*, 326(1-2):59 – 66, 1995.

[108] B.C. Khanra, J.C. Bertolini, and J.L. Rousset. Effect of surface segregation on the catalytic activity of alloys: CO hydrogenation on Pd-Ni(111) surface. *J. Mol. Catal. A: Chem.*, 129(23):233–240, 1998.

[109] Z. Li, O. Furlong, F. Calaza, L. Burkholder, H. Cheuk Poon, D. Saldin, and W. T. Tysoe. Surface segregation of gold for Au/Pd(111) alloys measured by low-energy electron diffraction and low-energy ion scattering. *Surf. Sci.*, 602(5):1084 – 1091, 2008.

[110] C. J. Powell and A. Jablonski. *NIST Electron Inelastic-Mean-Free-Path Database - Version 1.2*. National Institute of Standards and Technology, Gaithersburg, MD, 2010.

[111] S. Zimnik, C. Piochacz, S. Vohburger, and C. Hugenschmidt. Comparative Study of Time-Dependent PAES and XPS on a Ni/Pd Surface. *Defect and Diffusion Forum*, 373:313–316, 2016.

[112] P. M. Agrawal, B. M. Rice, and D. L. Thompson. Predicting trends in rate parameters for self-diffusion on fcc metal surfaces. *Surf. Sci.*, 515(1):21 – 35, 2002.

[113] C.L. Liu, J.M. Cohen, J.B. Adams, and A.F. Voter. EAM study of surface self-diffusion of single adatoms of fcc metals Ni, Cu, Al, Ag, Au, Pd, and Pt. *Surf. Sci.*, 253(1):334 – 344, 1991.

[114] G. Antczak and G. Ehrlich. Jump processes in surface diffusion. *Surf. Sci. Rep.*, 62(2):39 – 61, 2007.

[115] K. Oura, V.G. Lifshits, A Saranin, A.V. Zotov, and M. Katayama. *Surface Science: An Introduction*. Springer-Verlag Berlin Heidelberg, 2003.

[116] L. Chen, C. Zhou, J. Wu, and H. Cheng. Hydrogen adsorption and desorption on the Pt and Pd subnano clusters — a review. *Front. Phys. China*, 4(3):356–366, 2009.

[117] F. L. Williams and D. Nason. Binary alloy surface compositions from bulk alloy thermodynamic data. *Surf. Sci.*, 45(2):377 – 408, 1974.

[118] R.A. Van Santen and W.M.H. Sachtler. A theory of surface enrichment in ordered alloys. *J. Catal.*, 33(2):202 – 209, 1974.

[119] D. McLean. *Grain boundaries in metals*. Monographs on the physics and chemistry of materials. Clarendon Press, 1957.

[120] Y. Ma and P. B. Balbuena. Pt surface segregation in bimetallic pt3m alloys: A density functional theory study. *Surf. Sci.*, 602(1):107 – 113, 2008.

[121] J.J Burton and R.S Polizzotti. Surface segregation in alloys: Dilute solid solutions of Cr, Fe and Ni in Pt. *Surf. Sci.*, 66(1):1 – 13, 1977.

[122] C. Cui, L. Gan, M. Heggen, S. Rudiand, and P. Strasser. Compositional segregation in shaped Pt alloy nanoparticles and their structural behaviour during electrocatalysis. *Nature Materials*, 12:765–771, 2013.

[123] J. Y. Park, Y. Zhang, S. Hoon Joo, Y. Jung, and G. A. Somorjai. Size effect of RhPt bimetallic nanoparticles in catalytic activity of CO oxidation: Role of surface segregation. *Catalysis Today*, 181(1):133 – 137, 2012.

[124] L. Peng, E. Ringe, R. P. Van Duyne, and L. D. Marks. Segregation in bimetallic nanoparticles. *Phys. Chem. Chem. Phys.*, 17:27940–27951, 2015.

[125] G. Guisbiers, G. Abudukelimu, and D. Hourlier. Size-dependent catalytic and melting properties of platinum-palladium nanoparticles. *Nanoscale Research Letters*, 6(1):396, 2011.

[126] M. Johansson, O. Lytken, and I. Chorkendorff. The sticking probability of hydrogen on Ni, Pd and Pt at a hydrogen pressure of 1 bar. *Topics in Catalysis*, 46(1):175–187, 2007.

[127] K.H. Lee, A.R. Koymen, D. Mehl, K.O. Jensen, and A. Weiss. Measurement of positron annihilation induced Auger electron emission from Fe, Cu, Pd, and Au. *Surf. Sci.*, 264(1):127 – 134, 1992.

[128] M.-H. Xie, J. Zhang, A. Lees, J.M. Fernandez, and B.A. Joyce. Surface segregation during molecular beam epitaxy: the site-blocking effects of surfactant atoms. *Surf. Sci.*, 367(2):231 – 237, 1996.

[129] T. T. Fister, D. D. Fong, J. A. Eastman, P. M. Baldo, Ma. J. Highland, P. H. Fuoss, K. R. Balasubramaniam, J. C. Meador, and P. A. Salvador. In situ characterization of strontium surface segregation in epitaxial La0.7Sr0.3MnO3 thin films as a function of oxygen partial pressure. *Appl. Phys. Lett.*, 93(15):151904, 2008.

[130] K. Kimura, Y. Endoh, M. Mannami, H. J. Gossmann, G. H. Gilmer, and L. C. Feldman. Anomalous surface segregation of Sb in Si during epitaxial growth. *Appl. Phys. Lett.*, 69(1):67–69, 1996.

Acknowledgment

An dieser Stelle möchte ich allen danken, die maßgeblich zum Erfolg dieser Arbeit beigetragen haben. An erster Stelle gilt mein Dank Herrn Dr. Christoph Hugenschmidt für die Möglichkeit der Promotion in seiner Gruppe. Seine fachliche Kompetenz und sein persönliches Engagement haben mir bei der Erstellung dieser Arbeit sehr geholfen. Er versteht es, eine nicht alltägliche Vertrauensbasis zu seinen Mitarbeitern aufzubauen, mit der er eine besondere kollegiale und freundschaftliche Arbeitsatmosphäre im Team der Positronenquelle schafft.

Mein besonderer Dank gilt außerdem Prof. Peter Böni. Seine interessierten Fragen und sein bescheidenes und freundliches Auftreten bereicherten zahlreiche Diskussionen. Seine persönlichen Einschätzung habe ich gerne als Rat angenommen. Für seine Unterstützung für mein Stipendium möchte ich mich sehr bedanken.

Prof. Peter Feulner möchte ich für die Diskussion von Messergebnissen und seinen Mitarbeitern vom Lehrstuhl E20 für die zahlreichen Tipps zum STM danken.

Sebastian Vohburger möchte ich für seinen unermüdlichen Einsatz als Techniker in unserer Gruppe danken. Wann immer es etwas zu tun gab stand er mit Fachkunde, Hilfsbereitschaft und sehr viel persönlichem Einsatz sofort bereit. Dr. Christian Piochacz und Marcel Dickmann danke ich für ihre unschätzbare Unterstützung insbesondere während der Messzeiten. Ohne ihren Einsatz und ihre Erfahrung hätte nicht ein einziges Positron die Probe erreicht. Dr. Hubert Ceeh danke ich für seine unschätzbare Erfahrung in gefühlt allem – sei es Messelektronik, Auslegung von experimentellen Aufbauten, Datenauswertung und -interpretation oder unverzichtbarem Star Wars-Wissen. Benjamin Rienäcker möchte ich besonders für seine Unterstützung in allen LabView Angelegenheiten danken und Mathias Hackenberg für seine Unterstützung bei meiner Datenauswertung. Seine hervorragenden Programmierkenntnisse, geduldigen Erklärungen und zahlreichen Beispiele haben mir die Arbeit enorm erleichtert. Niklas Grill und Bernhard Kalis danke ich für die gute Zusammenarbeit während ihrer Master- bzw. Bachelorarbeit. Für die vielen hilfreichen Tipps und das Korrekturlesen dieser Arbeit möchte ich mich bei Matthias Dodenhöft, Johannes Mitteneder, Benjamin Rienäcker und Marcel Dickmann

bedanken. Mein Dank gilt dem gesamten NEPOMUC Team, den Kollegen von E21/E51 und des MLZ. Es hat großen Spaß gemacht in diesem Umfeld arbeiten zu dürfen und gemeinsame Konferenzen, Skiausflüge und Feiern zu erleben.

Der FRM2 Werkstatt von Herrn Christian Herzog danke ich herzlich für die schnelle Bearbeitung verschiedenster Bauteile. Die Herstellung meiner sehr filigranen Probenhalter mit unzähligen M1.6 Gewindebohrungen erforderten die Geduld von Herrn Robert Schlecht.

Frau Susanne Mayr vom Kristalllabor des Physik Departments möchte ich für die Laue Charakterisierung der Einkristalle danken. Ebenso gilt mein Dank Herrn Armin Kriele für seine Unterstützung im Materialwisschenschaftlichen Labor.

Dem Bundesministerium für Bildung und Forschung danke ich für die Finanzierung einer Vielzahl von Komponenten für das Spektrometer.

Das größte Dankeschön gilt meiner Familie, die meine etwas aus der Art schlagende Begeisterung für Physik immer unterstützt und gefördert hat und immer für mich da war. Insbesondere Philip Pikart für die Motivation zur Promotion und die liebevolle Unterstützung währenddessen.